FIELD-ASSISTED SINTERING

Tutorial

Eugene A. Olevsky

Dean and Distinguished Professor

San Diego State University, USA

SDSU | San Diego State University

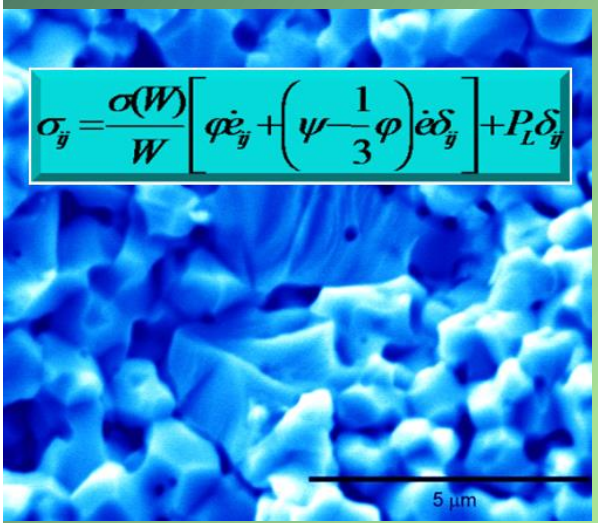

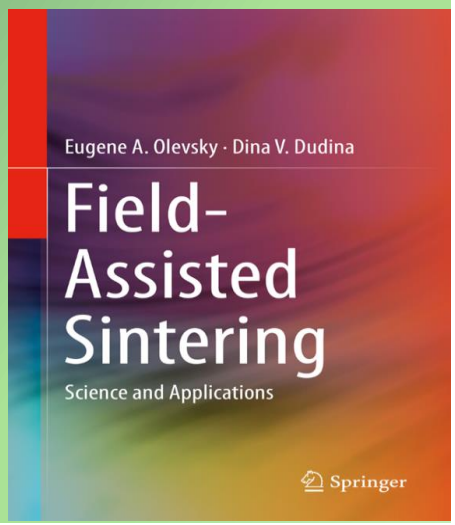

FIELD-ASSISTED SINTERING

Tutorial

Eugene A. Olevsky

Dean and Distinguished Professor

San Diego State University, USA

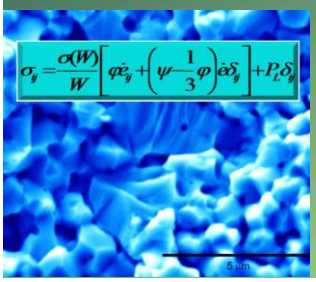

SDSU | San Diego State University

TUTORIAL CONTENTS

- Sintering Fundamentals: Classic Concepts
- Sintering Fundamentals: Continuum Theory
- Introduction to Field-Assisted Sintering
- Spark-Plasma Sintering
- High-Voltage Electric Discharge Compaction
- Flash Sintering
- Microwave Sintering
- Integrated Additive Manufacturing – Field-Assisted Sintering
- Electric Nano-Pulse Technology

TUTORIAL CONTENTS

- **Sintering Fundamentals: Classic Concepts**
- Sintering Fundamentals: Continuum Theory
- Introduction to Field-Assisted Sintering
- Spark-Plasma Sintering
- High-Voltage Electric Discharge Compaction
- Flash Sintering
- Microwave Sintering
- Integrated Additive Manufacturing – Field-Assisted Sintering
- Electric Nano-Pulse Technology

PHYSICAL BASIS OF SINTERING

50 years to find out!

Surface tension phenomena

PHYSICAL BASIS OF SINTERING

Surface tension phenomena

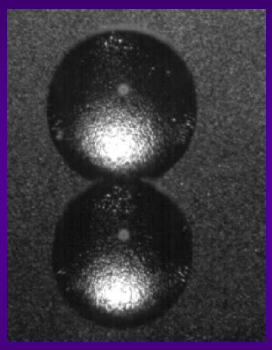

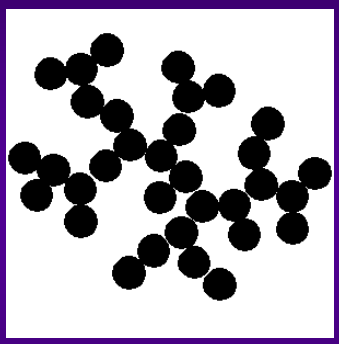

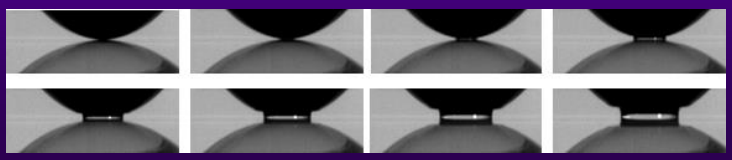

Definitions of sintering

Mechanical
Sintering is a thermally activated transition of a powder (or a porous system) to a more thermodynamically stable state, through a decrease of the free surface energy.

Physical
Sintering is a thermal treatment for bonding particles into a coherent and predominantly solid structure, via mass transport events that often occur on the atomic scale. The bonding leads to improved strength and a lower system energy.

Practical
Sintering is an operation in a metallurgical cycle of production of powder articles, in whose course a pre-compacted powder body changes its structure and obtains the required physical-mechanical properties.

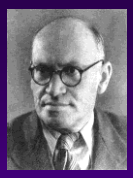

SINTERING THEORY

Frenkel approach (1945)

coalescence of viscous particles driven by surface tension

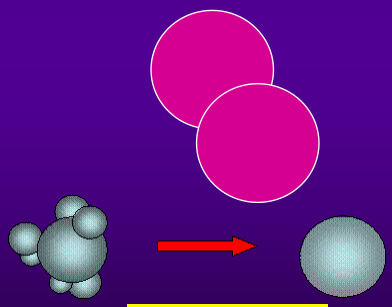

$$-\frac{\partial E_s}{\partial t} = 2\eta\dot{\varepsilon}^2 V$$

Pines approach (1946)

evaporation of emptiness

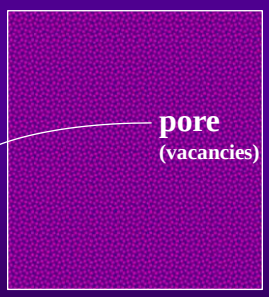

$$C = C_o\left(1 + \frac{2\alpha}{r}\frac{\Omega}{kT}\right)$$

1894-1952

coalescence of viscous particles driven by surface tension

$$-\frac{\partial E_s}{\partial t} = 2\eta\dot{\varepsilon}^2 V$$

Frenkel's Model (1945)

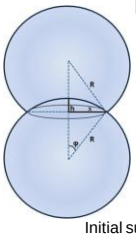

Viscous flow

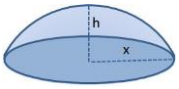

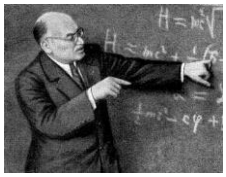

$$S_{segm} = \pi(h^2 + x^2)$$

$$h = R(1-\cos\varphi),\ x = R\sin\varphi$$

$$S_{segm} = \pi[R^2(1-\cos\varphi)^2 + R^2\sin^2\varphi] = 2\pi R^2(1-\cos\varphi)$$

Initial surface of particles: $S_0 = 8\pi R^2$

Current surface: $S = S_0 - 2S_{segm} = 8\pi R^2 - 4\pi R^2(1-\cos\varphi) = 4\pi R^2(1+\cos\varphi) = 8\pi R^2\cos\frac{\varphi}{2}$

Free surface energy: $E_s = S\cdot\alpha$, α -surface tension (N/m); $E_s = 8\pi\alpha R^2\cos^2\frac{\varphi}{2}$

Rate of change of the free surface energy:

$$W_s = -\frac{\partial E_s}{\partial t} = -8\pi\alpha R^2\cdot 2\cos\frac{\varphi}{2}\sin\frac{\varphi}{2}\cdot\frac{1}{2}\frac{\partial\varphi}{\partial t} = -4\pi\alpha R^2\sin\varphi\frac{\partial\varphi}{\partial t}$$

For small $\varphi, \sin\varphi \approx \varphi$ $\quad W_s = -4\pi\alpha R^2\varphi\frac{\partial\varphi}{\partial t}$

Work power of viscous deformation: $W_V = 2\eta\cdot(\dot{\varepsilon})^2\cdot V$

η -viscosity $(Pa\cdot s)$ $\left(\eta = \frac{kT}{Db}\right)$

$\dot{\varepsilon}$ -strain rate (s^{-1})

V -volume of deformation (m^3)

$$V = \frac{8}{3}\pi R^3$$

$$\varepsilon = \frac{h}{R} = 1-\cos\varphi = 2\sin^2\frac{\varphi}{2} \approx 2\left(\frac{\varphi}{2}\right)^2 = \frac{\varphi^2}{2}$$

$$\dot{\varepsilon} = \frac{d\varepsilon}{dt} = \varphi\cdot\dot{\varphi}$$

$$W_v = 2\eta(\varphi\cdot\dot{\varphi})^2\cdot\frac{8}{3}\pi R^3 = \frac{16}{3}\eta R^3\cdot\varphi^2\cdot\dot{\varphi}^2$$

r – pore radius: $r - r_0 = -\frac{3}{4}\frac{\alpha}{\eta}t$

Isolated pore collapse kinetics (second problem solved by Frenkel)

$$W_s = W_v \Rightarrow -4\pi\alpha R^2\varphi\cdot\dot{\varphi} = \frac{16}{3}\eta R^3\varphi^2\cdot\dot{\varphi}^2 \Rightarrow R\cdot\varphi\cdot\dot{\varphi} = -\frac{3}{4}\frac{\alpha}{\eta} \Rightarrow \varphi^2 - \varphi_0^2 = \frac{3}{2}\frac{\alpha}{\eta R}(t-t_0)$$

$$\varphi = \frac{x}{R} \Rightarrow x^2 - x_0^2 \approx \frac{3}{2}\frac{\alpha R}{\eta}(t-t_0);\quad \text{if}\quad x_0 = 0, t_0 = 0 \Rightarrow x = \left(\frac{3}{2}\frac{\alpha R}{\eta}t\right)^{\frac{1}{2}} \rightarrow$$

Neck growth kinetics

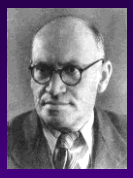

Frenkel approach (1945)

coalescence of viscous particles driven by surface tension

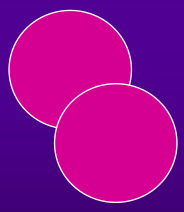

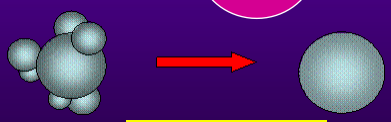

$$-\frac{\partial E_s}{\partial t} = 2\eta\dot{\varepsilon}^2 V$$

Рис. 2.5. Последовательность кинокадров, иллюстрирующих слияние вязких сфер [7].

Рис. 2.6. Результат обработки кинограммы, изображенной на рис. 2.5: *1* – зависимость ξ от *t*; *2* – зависимость κ от *t*.

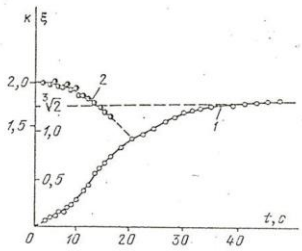

Pines' Model (1946)

1905-1968

"evaporation of emptiness"

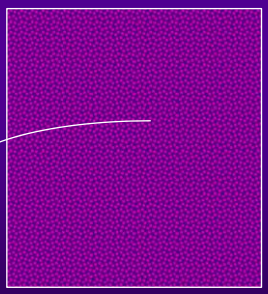

$$C = C_o\left(1 + \frac{2\alpha}{r}\frac{\Omega}{kT}\right)$$

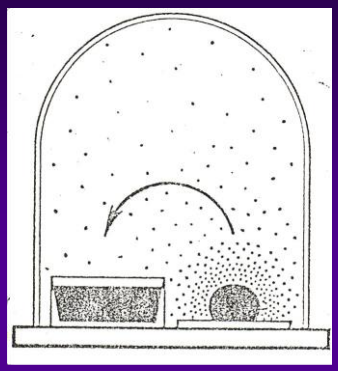

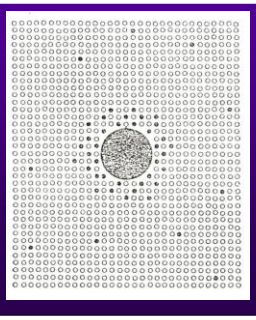

Kuczynski's Model (1949)

Self-diffusion in Sintering of Metallic Particles

1914-1990

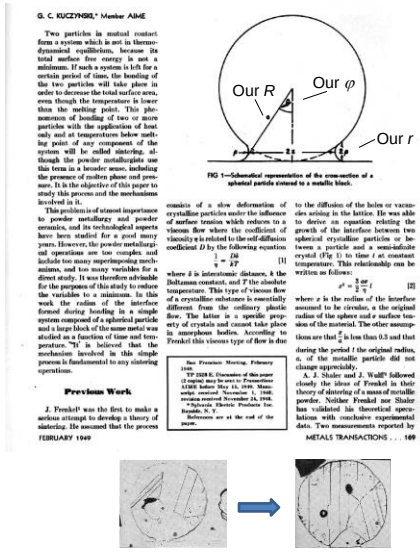

G. C. KUCZYNSKI,* Member AIME

Two particles in mutual contact form a system which is not in thermodynamical equilibrium, because its total surface free energy is not a minimum. If such a system is left for a certain period of time, the bonding of the two particles will take place in order to decrease the total surface area, even though the temperature is lower than the melting point. This phenomenon of bonding of two or more particles with the application of heat only and at temperatures below melting point of any component of the system will be called sintering, although the powder metallurgists use this term in a broader sense, including the presence of molten phase and pressure. It is the objective of this paper to study this process and the mechanisms involved in it.

This problem is of utmost importance to powder metallurgy and powder ceramics, and its technological aspects have been studied for a good many years. However, the powder metallurgical operations are too complex and include too many superimposing mechanisms, and too many variables for a direct study. It was therefore advisable for the purposes of this study to reduce the variables to a minimum. In this work the radius of the interface formed during bonding in a simple system composed of a spherical particle and a large block of the same metal was studied as a function of time and temperature. "It is believed that the mechanism involved in this simple process is fundamental to any sintering operations.

Previous Work

J. Frenkel[1] was the first to make a serious attempt to develop a theory of sintering. He assumed that the process consists of a slow deformation of crystalline particles under the influence of surface tension which reduces to a viscous flow where the coefficient of viscosity η is related to the self-diffusion coefficient D by the following equation

$$\frac{1}{\eta} = \frac{D\delta}{kT} \quad [1]$$

where δ is interatomic distance, k the Boltzmann constant, and T the absolute temperature. This type of viscous flow of a crystalline substance is essentially different from the ordinary plastic flow. The latter is a specific property of crystals and cannot take place in amorphous bodies. According to Frenkel this viscous type of flow is due to the diffusion of the holes or vacancies acting in the lattice. He was able to derive an equation relating the growth of the interface between two spherical crystalline particles or between a particle and a semi-infinite crystal (Fig 1) to time t at constant temperature. This relationship can be written as follows:

$$x^5 = \frac{5}{3}\frac{\alpha\delta}{\eta} t \quad [2]$$

where x is the radius of the interface assumed to be circular, α the original radius of the sphere and α surface tension of the material. The other assumptions are that $\frac{x}{\alpha}$ is less than 0.3 and that during the period t the original radius, α, of the metallic particle did not change appreciably.

A. J. Shaler and J. Wulff[2] followed closely the ideas of Frenkel in their theory of sintering of a mass of metallic powder. Neither Frenkel nor Shaler has validated his theoretical speculations with conclusive experimental data. Two measurements reported by

Sao Francisco Meeting, February 1949.
TP 2528 E. Discussion of this paper (2 pages) may be submitted before 12 noon Sunday May 15, 1949. Manuscript received November 1, 1948; revision received November 24, 1948.
*Sylvania Electric Products Inc. Bayside, N. Y.
References are at the end of the paper.

FIG 1—Schematical representation of the cross-section of a spherical particle sintered to a metallic block.

FEBRUARY 1949 METALS TRANSACTIONS . . . 169

Volume diffusion

First Fick's equation:

$$\frac{dV}{dt} = D\frac{dC}{dy}\cdot A$$

V -diffusing volume
C -concentration
y -coordinate
A -elementary surface area (normal to the diffusion flux)
D -coefficient of self-diffusion

$\varphi \approx \sin\varphi$

$$r = R(1-\cos\varphi) = 2R\sin^2\frac{\varphi}{2} \approx \frac{x^2}{2R}$$

A -area of junction of particles:

$$A = 2x\cdot\frac{2\pi r}{2} = 2\pi r x = \pi\frac{x^3}{R}$$

V -volume of the junction:

$$V = \pi x^2\cdot r = \pi\frac{x^4}{2R}$$

For volume diffusion:

$$\frac{dV}{dt} = A\cdot\frac{\Delta C}{r}\cdot D_v,\ D_v\text{-coefficient of the volume diffusion}$$

$$\Delta C = C - C_0 = \frac{2\alpha}{r}\cdot\frac{\Omega}{kT}$$ - Pines(Kelvin) Equation, Ω - atomic volume

$$\frac{d}{dt}[\pi\frac{x^4}{2R}] = \pi\frac{x^3}{R}\cdot\frac{2\alpha}{r^2}\cdot\frac{\Omega}{kT}D_v$$

$$2\pi\frac{x^3}{R}\cdot\dot{x} = \pi\frac{x^3}{R}\frac{2\alpha}{x^4}\cdot 4R^2\frac{\Omega D_v}{kT}$$

$$x^4\cdot\dot{x} = \frac{4\alpha R^2\Omega D_v}{kT}$$

$$x^4dx = \frac{4\alpha R^2\Omega D_v}{kT}dt$$

$$x^5 = \frac{20\alpha R^2\Omega D_v}{kT}t$$

$$x = (\frac{20\alpha R^2\Omega D_v}{kT}t)^{\frac{1}{5}}$$

Surface diffusion

$$A = 2\pi x\delta;\delta^3 = \Omega$$

$$\frac{d}{dt}[\pi\frac{x^4}{2R}] = 2\pi x\delta\cdot\frac{2\alpha}{r^2}\frac{\delta^3}{kT}\cdot D_s$$

$$2\pi\frac{x^3}{R}\cdot\dot{x} = 4\pi\cdot\frac{\alpha\delta^4\cdot D_s}{kTx^3}4R^2$$

$$x^6dx = \frac{8\alpha\delta^4R^3D_s}{kT}dt$$

$$x^7 = \frac{56\alpha\delta^4R^3D_s}{kT}t \Rightarrow x = (\frac{56\alpha\delta^4R^3D_s}{kT}t)^{\frac{1}{7}}$$

Mass Transport in Sintering

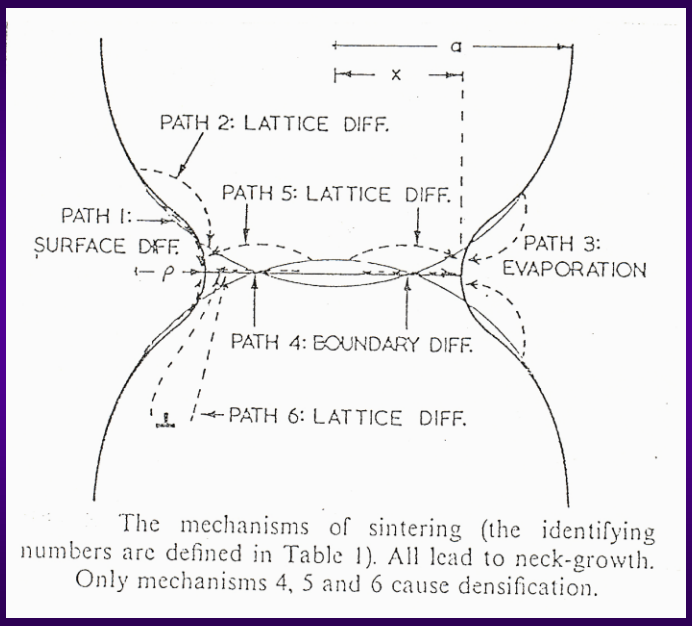

The mechanisms of sintering (the identifying numbers are defined in Table 1). All lead to neck-growth. Only mechanisms 4, 5 and 6 cause densification.

From Swinkels and Ashby

Ashby Sintering Maps

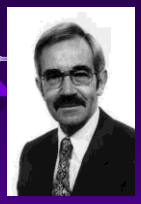

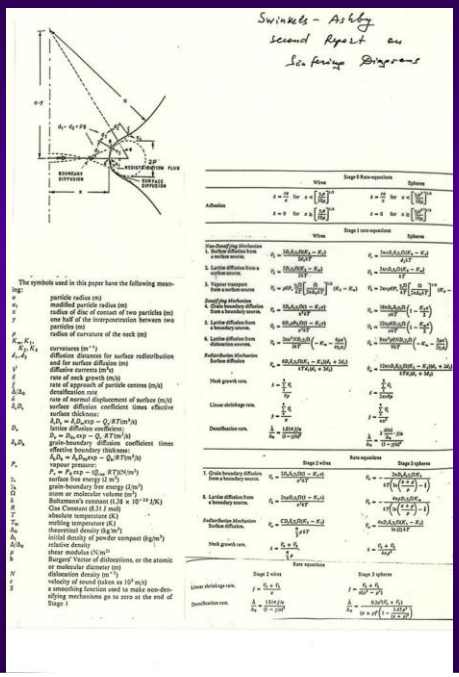

Ashby Sintering Maps

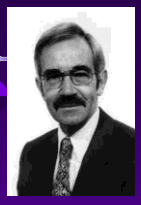

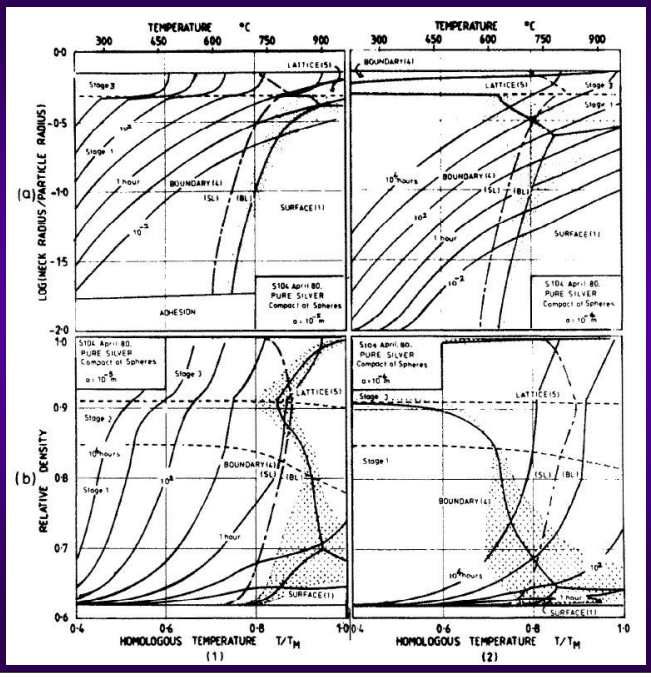

Questions / Problems

1. What is the moving force for sintering?
2. What is the main difference in Frenkle's and Pines' approaches in the description of sintering?
3. What is the main problem inherent in the model basis of Frenkel approach?
4. What is the main problem of the model of Pines?
5. Which general approaches does the Kuczynsky model belong to: Frenkel or Pines?
6. What serious assumption is used as a basis for the construction of Ashby sintering diagrams?

TUTORIAL CONTENTS

- Sintering Fundamentals: Classic Concepts
- **Sintering Fundamentals: Continuum Theory**
- Introduction to Field-Assisted Sintering
- Spark-Plasma Sintering
- High-Voltage Electric Discharge Compaction
- Flash Sintering
- Microwave Sintering
- Integrated Additive Manufacturing – Field-Assisted Sintering
- Electric Nano-Pulse Technology

COMPLEX SHAPE PARTS PRODUCED VIA POWDER METALLURGY ROUTE

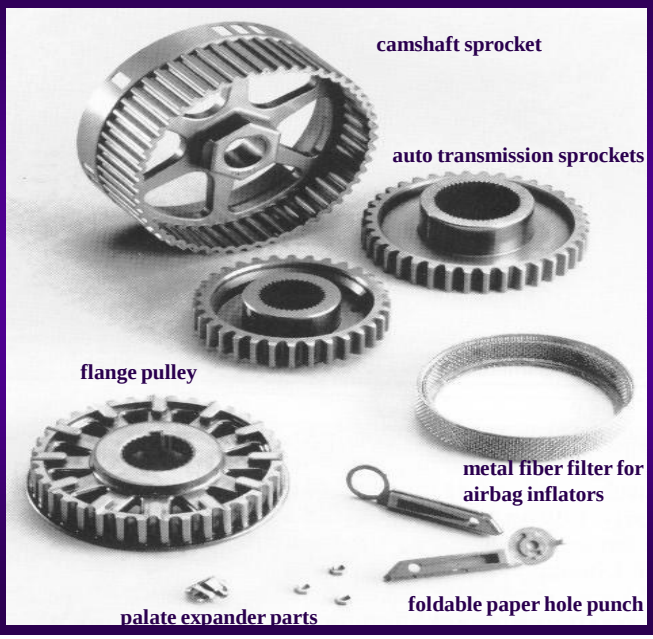

SINTERING: SHAPE DISTORTIONS

Napoleon

Wellington

Theory of Sintering: Practical Implementation

- It was necessary to combine ideas of
- **MECHANICS**
  - **&**
    - **MATERIALS SCIENCE**
- **The breakthrough happened in the end of 1980s**

TUTORIAL CONTENTS

- Sintering Fundamentals: Classic Concepts
- **Sintering Fundamentals: Continuum Theory**
- Introduction to Field-Assisted Sintering
- Spark-Plasma Sintering
- High-Voltage Electric Discharge Compaction
- Flash Sintering
- Microwave Sintering
- Integrated Additive Manufacturing – Field-Assisted Sintering
- Electric Nano-Pulse Technology

Continuum Theory of Sintering: The Main Constitutive Relationship

Strain rate component

Bulk modulus: Resistance to the volume change function of porosity

Shear modulus: Resistance to the shape change function of porosity

$$\sigma_{ij} = \frac{\sigma(W)}{W}\left[\varphi\dot{e}_{ij} + \left(\psi - \frac{1}{3}\varphi\right)\dot{e}\delta_{ij}\right] + P_L\delta_{ij}$$

Volume strain rate

Generalized viscosity: corresponds to the constitutive properties of particle material

Effective sintering stress: function of porosity

externally applied stresses | material resistance | sintering

Olevsky E.A. (1998), Theory of sintering: from discrete to continuum. Review, *Mater. Sci. & Eng. R: Reports*, 40-100

Continuum Theory of Sintering

Without considering sintering stress

$$\sigma_{ij} = \frac{\sigma(w)}{w}[\varphi\dot{\varepsilon}_{ij} + (\psi - \frac{1}{3}\varphi)\dot{e}\delta_{ij}]$$

σ_{ij} is the ij component of the stress tensor; $\sigma(w)$ effective stress

$\sigma(w) = 2\eta_0 w$ Linear viscous (hot deformation of amorphous materials; free sintering)

$\sigma(w) = \sigma_y$ Plastic (cold pressing)

$\sigma(w) = Aw^m$ Power-law creep (hot deformation of crystalline materials)

Continuum Theory of Sintering

$$\sigma_{ij} = \frac{\sigma(w)}{w}[\varphi\dot{\varepsilon}_{ij} + (\psi - \frac{1}{3}\varphi)\dot{e}\delta_{ij}]$$

$$\psi = \frac{2}{3}\frac{(1-\theta)^3}{\theta}$$ Bulk modulus

δ_{ij} Kronecker delta

$$\varphi = (1-\theta)^2$$ Shear modulus

η_0 Shear viscosity of the fully-dense material

$$w = \frac{1}{\sqrt{1-\theta}}\sqrt{\varphi\dot{\gamma}^2 + \psi\dot{e}^2}$$ Equivalent effective strain rate

$$\dot{e} = \dot{\varepsilon}_{ii} = \dot{\varepsilon}_{11} + \dot{\varepsilon}_{22} + \dot{\varepsilon}_{33}$$ volume change rate

Shape change rate

$$\dot{\gamma} = \frac{1}{\sqrt{3}}\sqrt{(\dot{\varepsilon}_1 - \dot{\varepsilon}_2)^2 + (\dot{\varepsilon}_2 - \dot{\varepsilon}_3)^2 + (\dot{\varepsilon}_3 - \dot{\varepsilon}_1)^2}$$

23

23

Continuum Theory of Sintering

Including sintering stress:

$$\sigma_{ij} = \frac{\sigma(w)}{w}[\varphi\dot{\varepsilon}_{ij} + (\psi - \frac{1}{3}\varphi)\dot{e}\delta_{ij}] + p_l\delta_{ij}$$

$$p_l = \frac{3}{2}\frac{\alpha}{r_0}(1-\theta)^2$$

p_l The effective sintering stress

α Surface tension

r_0 Radius of the particle

σ_{ij} external stress

For free sintering, no external stress, $\sigma_{ij} = 0$

24

24

Continuum Theory of Sintering

Problem of free sintering of a porous body

$$\sigma_{ij} = 0 \Rightarrow \frac{\sigma(w)}{w}[\varphi\dot{\varepsilon}_{ij} + (\psi - \frac{1}{3}\varphi)\dot{e}\delta_{ij}] = -p_l\delta_{ij}$$

For linear viscous phase $\sigma(w) = 2\eta_0 w$

Projection on r direction: $2\eta_0[\varphi\dot{\varepsilon}_r + (\psi - \frac{1}{3}\varphi)\dot{e}] = -p_l$ (a)

Projection on z direction: $2\eta_0[\varphi\dot{\varepsilon}_z + (\psi - \frac{1}{3}\varphi)\dot{e}] = -p_l$ (b)

(a)*2+(b)➔ $2\eta_0[\varphi(2\dot{\varepsilon}_r + \dot{\varepsilon}_z) + 3(\psi - \frac{1}{3}\varphi)\dot{e}] = -3p_l$

$$\dot{e} = 2\dot{\varepsilon}_r + \dot{\varepsilon}_z \Rightarrow 2\eta_0 3\psi\dot{e} = -3p_l \Rightarrow p_l = -2\eta_0\psi\dot{e}$$

Continuity equation $\dot{e} = \frac{\dot{\theta}}{1-\theta}$

25

25

Continuum Theory of Sintering

$$\dot{e} = \frac{-p_l}{2\eta_0\psi} = \frac{\dot{\theta}}{1-\theta} = \frac{-\frac{3}{2}(1-\theta)^2\frac{\alpha}{r_0}}{2\eta_0\frac{2}{3}\frac{(1-\theta)^3}{\theta}} \Rightarrow$$

$$\dot{\theta} = -\frac{9\alpha\theta}{8\eta_0 r_0} \Rightarrow \frac{\dot{\theta}}{\theta} = -\frac{9\alpha}{8\eta_0 r_0} \Rightarrow \ln\theta = -\int\frac{9\alpha}{8\eta_0 r_0}dt$$

τ_s :Specific time of sintering

$$\tau_s = \int\frac{9\alpha}{8\eta_0 r_0}dt \Rightarrow \theta = \theta_1\exp(-\tau_s)$$

26

26

Pressing in rigid die and free sintering of a powder cylinder

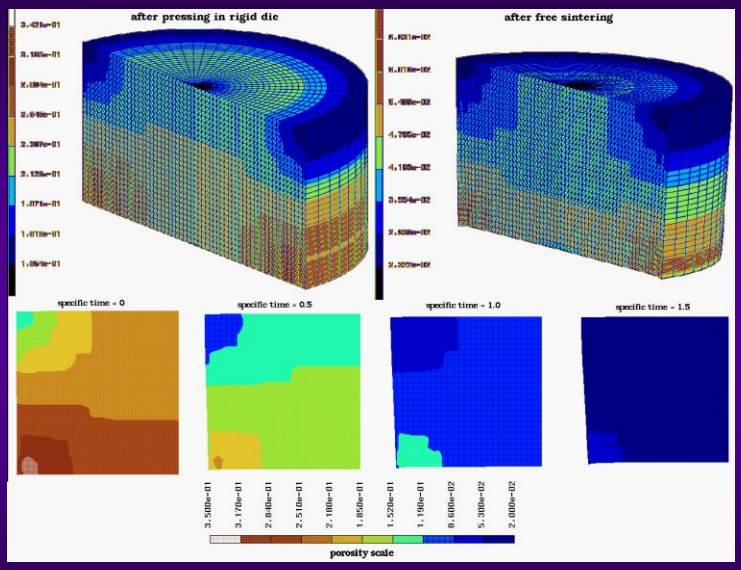

E. Olevsky, G. Timmermans, M. Shtern, L. Froyen, and L. Delaey, The permeable element method for modeling of deformation processes in porous and powder materials: Theoretical basis and checking by experiments, *Powd. Technol.* - 93/2, 123-141 (1997)

27

27

Gravity Influence on Sintering

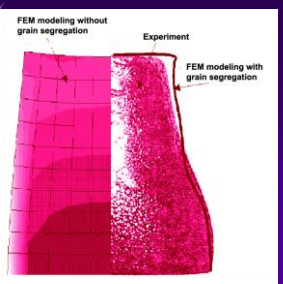

The calculated "elephant foot" profile and relative density distribution formed during liquid-phase sintering of 78W-15.4Ni-6.6Fe powder sample (from E.A. Olevsky and R.M. German, *Acta Mater.*, 48, 1167-1180 (2000))

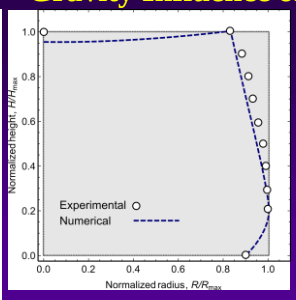

J.A. Alvarado-Contreras, R.M. German, A.L. Maximenko, E.A. Olevsky, Coupled Densification—Shape Distortion Analysis of Liquid Phase Sintering Affected By Gravity, *Met. Mater. Trans. A* 45 (2), 927-933 (2014)

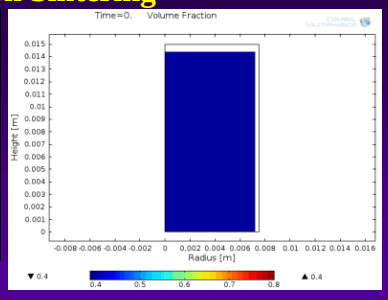

J.A. Alvarado-Contreras, E.A. Olevsky, A.L. Maximenko, R.M. German, A continuum approach for modeling gravitational effects on grain settling and shape distortion during liquid phase sintering of tungsten heavy alloys, *Acta Mater.*, 65, 176-184 (2014)

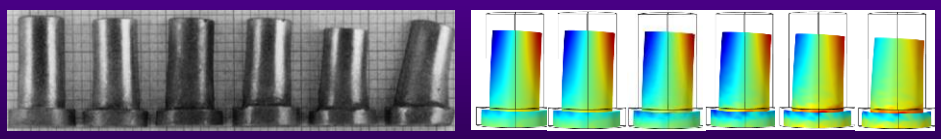

Comparison between the experimental and simulated gravity-induced distortions (with slumping)

J.A. Alvarado-Contreras, E.A. Olevsky, A.L. Maximenko, R.M. German, Kinetics of shrinkage and shape evolution during liquid phase sintering of tungsten heavy alloy, *J. Mater. Sci.*, 49 (3), 1130-1137 (2014)

28

28

Mesoscale Simulation Using the Potts Model

- E. Olevsky, V. Tikare, and T. Garino, Multi-scale modeling of sintering – A Review, *J. Amer. Ceram. Soc.*, 89 (6), 1914-1922 (2006)
- E. A. Olevsky, B. Kushnarev, A. Maximenko, V. Tikare, and M. Braginsky, Modeling anisotropic sintering in nanocrystalline ceramics, *Phil. Mag.*, 85, 2123-2146 (2005)
- V. Tikare, M. Braginsky, E. Olevsky, and D. L. Johnson, Numerical simulation of anisotropic shrinkage in a 2D compact of elongated particles, *J. Amer. Ceram. Soc.*, 88, 1, 59-65 (2005)
- M. Braginsky, V. Tikare, and E. Olevsky, Numerical simulation of solid state sintering, *Int. J. Solids and Structures*, 42, 621-636 (2005)
- E. Olevsky, B. Kushnarev, A. Maximenko, and V. Tikare, Modeling of sintering at multiple length scales: anisotropy phenomena, *TMS Letters*, 3, 55-56 (2004)
- V. Tikare, M. Braginsky, and E.A. Olevsky, Numerical simulation of solid-state sintering: I, Sintering of three particles, *J. Amer. Ceram. Soc.*, 86, 49-53 (2003)

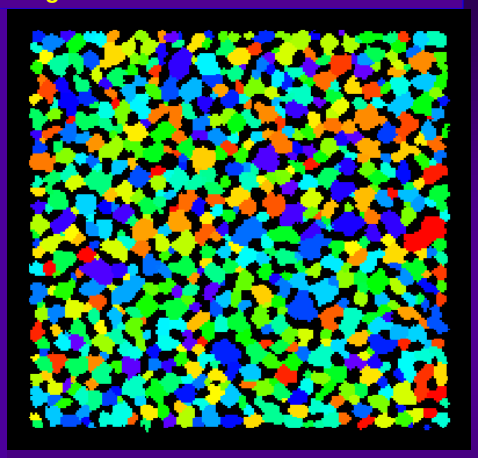

First publication:

V. Tikare, E.A. Olevsky, and M.V. Braginsky, Combined macro-meso scale modeling of sintering, in: Recent Developments in Computer Modeling of Powder Metallurgy Processes, ed. A. Zavaliangos and A. Laptev, IOS Press, 85-104 (2001)

Multi-Scale Virtual Reality of Powder Processing

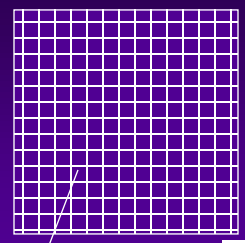

Boundary conditions

each element

initial state

current state

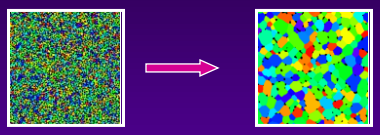

at each time step

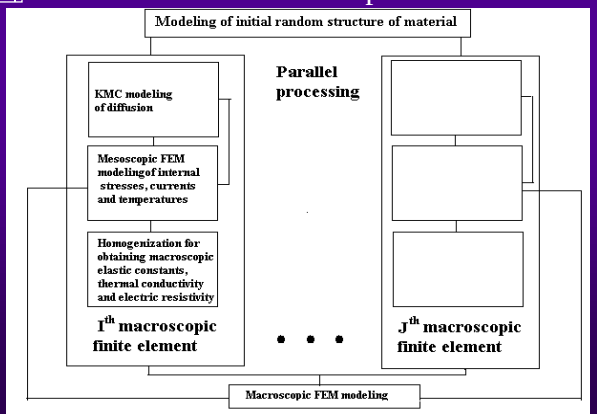

Sample problem solution: sintering with inclusion

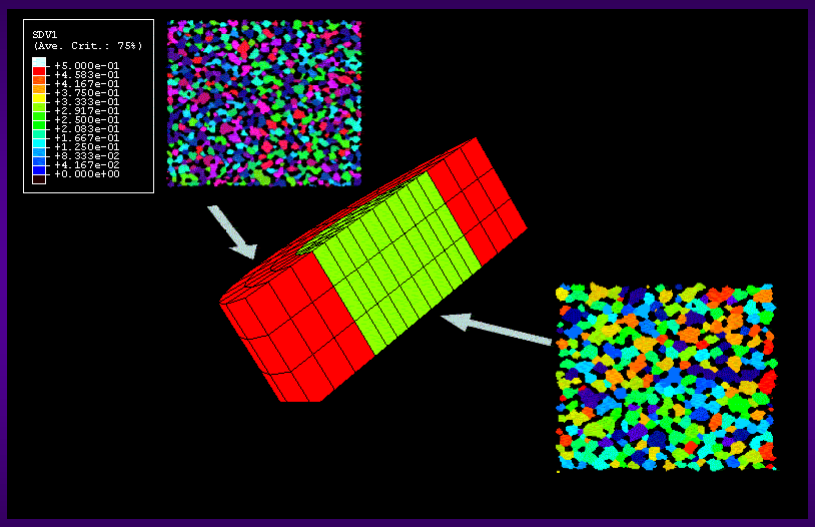

R. Bordia, S.J. Kang, E.A. Olevsky, Current understanding and future research directions at the onset of the next century of sintering science and technology, J. Am. Ceram. Soc., 100, 2314-2335 (2017)

Questions / Problems

1. What was the main incentive for the development of the Continuum Theory of Sintering?
2. Calculate the sintering stress for a porous component made by Al_2O_3 powder with surface tension=0.9 J/m^2 particle size 10 μm and 60% porosity.
3. Indicate different expressions of the effective stress used in the main constitutive equation of the continuum theory of sintering. For each expression, indicate which case is used.
4. The initial porosity before sintering is 40%. The specific time of sintering is 0.8. What is the total free sintering shrinkage?
5. In sintering of glass spheres with a radius of 15 μm, it took 200 min at 627°C to get a shrinkage of 30%. Knowing that the initial porosity was 0.4, and the surface energy of the glass 0.3 J/m^2 calculate the viscosity of the glass.
6. Derive from the main constitutive equation of the continuum theory of sintering the expression for the specific time of sintering.
7. Derive the expression for the viscous analogy of the Poisson's ratio in the sinter-forging of a linear viscous material.
8. For 2 hours of free sintering, the specific time of sintering is equal to 1. Find the dependence of the axial strain rate on porosity, which does not cause any change of radius of a cylindrical specimen subjected to sinter-forging.

TUTORIAL CONTENTS

- Sintering Fundamentals: Classic Concepts
- Sintering Fundamentals: Continuum Theory
- **Introduction to Field-Assisted Sintering**
- Spark-Plasma Sintering
- High-Voltage Electric Discharge Compaction
- Flash Sintering
- Microwave Sintering
- Integrated Additive Manufacturing – Field-Assisted Sintering
- Electric Nano-Pulse Technology

E. Olevsky and D. Dudina
Field-Assisted Sintering: Science and Applications,
Springer Nature IP, ISBN 978-3-319-76031-5, 425p., 2018

This book represents the first ever scientific monograph including an in-depth analysis of all major field-assisted sintering techniques.

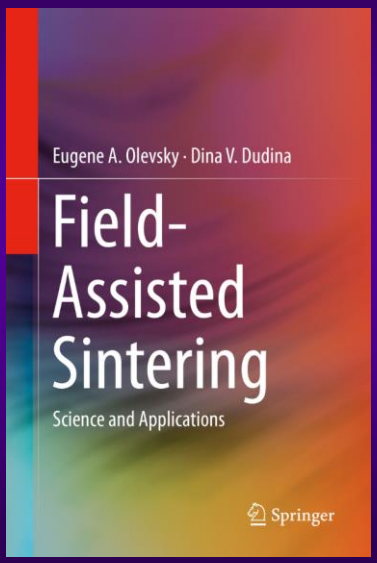

SPARK-PLASMA SINTERING, MICROWAVE SINTERING, MAGNETIC PULSE COMPACTION, AND HIGH-VOLTAGE IMPULSE COMPACTION

Spark-Plasma Sintering System LABOX 625 (Japan)

Система высоковольтного компактирования (РТУ)

Microwave Sintering System System VIS-300-01a at the Powder Technology Laboratory in San Diego, supervised by EO

Magnetic Pulse Compaction device by Nano Technology Inc., South Korea

TUTORIAL CONTENTS

- Sintering Fundamentals: Classic Concepts
- Sintering Fundamentals: Continuum Theory
- Introduction to Field-Assisted Sintering
- **Spark-Plasma Sintering**
- High-Voltage Electric Discharge Compaction
- Flash Sintering
- Microwave Sintering
- Integrated Additive Manufacturing – Field-Assisted Sintering
- Electric Nano-Pulse Technology

Spark-Plasma Sintering

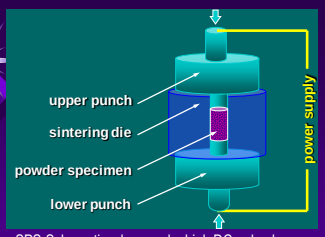

SPS Schematics; low-mode: high DC pulsed current, low voltage

INTRODUCTION

Spark-plasma sintering (SPS) is an emerging powder consolidating technique, which provides potentially revolutionary capabilities to the processing of materials into configurations previously unattainable. SPS consists essentially of the conjoint application of high temperature, high axial pressure and electric current assisted sintering.

Spark-Plasma Sintering System (MPS) Dr. Sinter 515S at SDSU. Max Load 50kN, max current 1500 A

BRIEF HISTORY OF SPARK-PLASMA SINTERING

1898 W.L. Voelker, G.B. Patent 6149.
1906 J. Lux, GB Patent No. 9020
1922 F. Sauerwald, Apparatus for direct resistance heating to high temperatures under high pressure, Zeitschrift fur Elektrochemie, 28, 181-183
1933 G.F. Taylor, Apparatus for making hard metal compositions, US Patent N1,896,854
1955 F. V. Lenel, Resistance sintering under pressure, Trans. AIME, 203, (1), 158-167
1962 K. Inoue, Electric-Discharge Sintering, US Patent N3,241,956
1966 K. Inoue, Apparatus for Electrically Sintering Discrete Bodies, US Patent N3,250,892
1970s Research on Spark Sintering and Electric-Spark Sintering in USA and USSR, respectively
1980s Research on Plasma Activated Sintering in Japan
1990s SPS Machines are developed by Sodick Co. and Sumitomo Coal Mining Co. Ltd., Japan
2000s Extensive experimentation throughout the world on SPS of various material systems

SPS APPROACHES AND MODIFICATIONS

- Resistance Sintering
- Electric-Discharge Sintering
- Field-Assisted Sintering
- Electric Spark Sintering
- Electroconsolidation
- Discharge Powder Compaction
- Plasma Activated Sintering
- Electric Pulse Sintering
- Pulse Electric Current Sintering

COMMERCIALLY AVAILABLE SPS DEVICES

- Metal Processing Systems, Inc. (MPS) - North American representative of SPS Syntax, Inc., Japan.
- FCT (Fine Ceramics Technologies) Systeme GmbH, Germany.
- Thermal Technology LLC, USA.
- ELTec Co., South Korea.

SPS-processed (SDSU) TaC powder specimen: 99% dense; maximum temperature 2300°C; maximum pressure 50 MPa; SPS time – 8 min

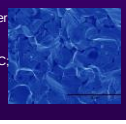

Consolidated pure bulk carbon nano-tubes (SDSU); 1700°C under a pressure of 50 MPa, 10 min, approximately 80% final relative density

Microstructure of Al2O3–TiC nanocomposites fabricated by spark plasma sintering from high-energy ball milled reactants

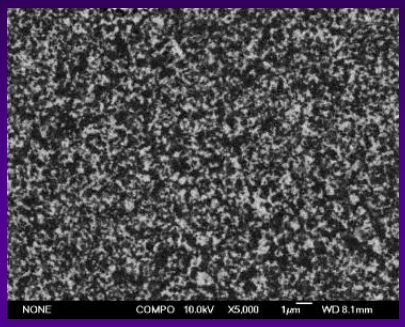

Backscattered SEM image of polished surface of the sintered sample. The gray-white phase is the TiC, and the dark phase is the Al2O3 matrix.

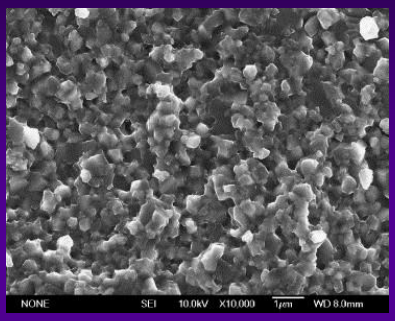

SEM micrograph of fracture surface of the sintered sample

The relative density of the samples consolidated by SPS technique in vacuum at 1480 °C for 4 min reached 99.2%. The final products exhibited very fine microstructure, and the grain sizes of Al_2O_3 and TiC were about 400 nm and 200 nm, respectively, with a flexure strength of 944 ± 21 MPa, Vickers hardness 21.0 ± 0.3 GPa, fracture toughness 3.87 ± 0.2 MPa $m^{1/2}$, and electrical conductivity 1.2787×10^5 S m^{-1}.

Microstructure of TaC specimens fabricated by spark plasma sintering

SPS-processed (SDSU) TaC powder specimen: 99% dense; maximum temperature 2300°C; maximum pressure 50 MPa; SPS time – 8 min

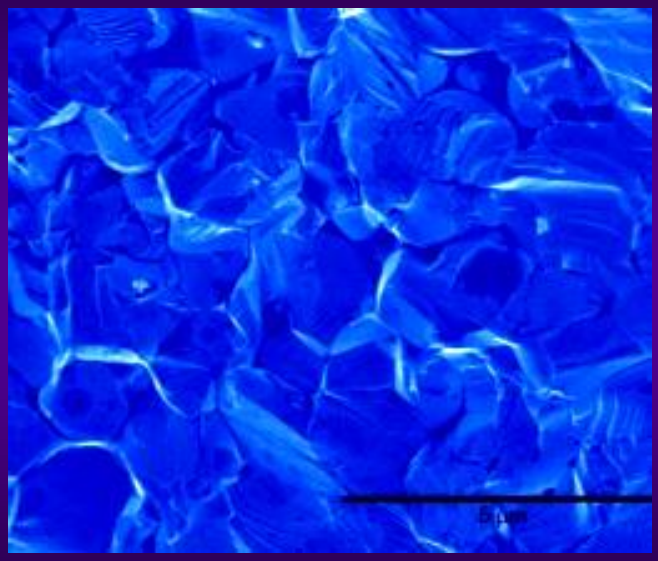

E. Khaleghi, Y.-S. Lin, E. Olevsky, and M. Meyers, Spark plasma sintering of tantalum carbide, Scripta Mater., 63, 577-580 (2010)

FLASH SiC SPS RESULTS

- Limited Grain growth
- Excellent Densification

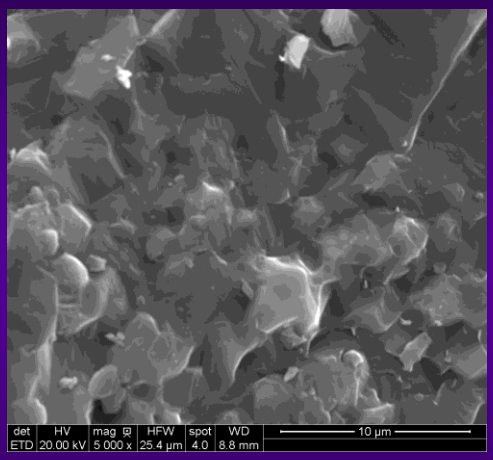

B4C SPS RESULTS

- Limited Grain growth
- Good Densification
- 1800C

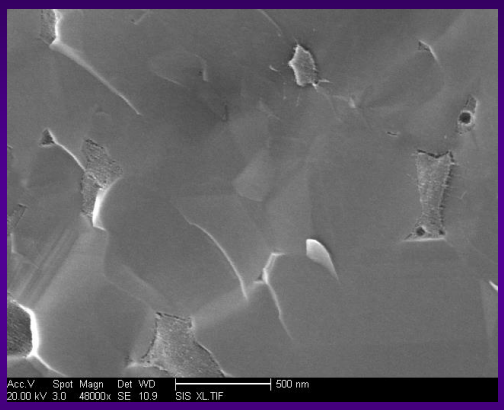

Synthesis of Bulk Carbon Nanotube Material

Bulk multi-walled carbon nanotube was prepared by spark plasma sintering at 1700 °C under a pressure of 50 MPa in vacuum. The density of the bulk sample reaches 72% of the theoretical density of the carbon nanotube, 2 g/cm3.

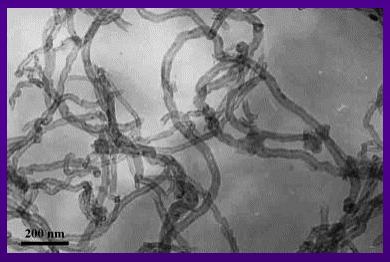

TEM observation of original nanotubes.

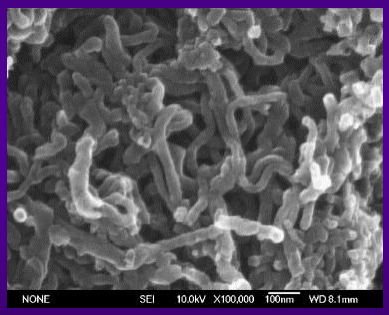

FESEM morphology of the sintered bulk CNTs

A high-strength bulk nanocrystalline Al–Fe alloy processed by mechanical alloying and spark plasma sintering

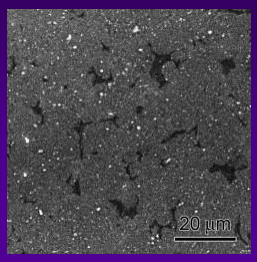

spark plasma sintered Al–5 at.% Fe alloy.

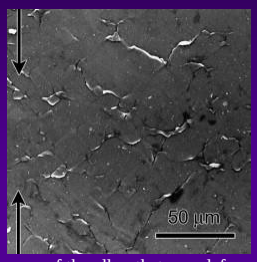

SEM image of the alloy that was deformed to a strain of 0.08. This micrograph indicates the coarse α-Al grains were mainly deformed.

A bulk nanocrystalline Al–5 at.% Fe alloy was synthesized by mechanical alloying and spark plasma sintering. The alloy exhibited a very high compressive yield strength of 1 GPa with a plastic strain of 0.3. The alloy consists of coarse α-Al grains that form from powder boundaries and nanocrystalline regions composed of α-Al and Al_6Fe phases. The combination of the coarse and nanoscale grains are considered to be the reason for the large plastic strain in such a high-strength material.

E. Olevsky, S. Kandukuri, and L. Froyen, Consolidation enhancement in spark-plasma sintering: Impact of high heating rates, *J. App. Phys.*, 102, 114913-114924 (2007)

Thermal and mechanical properties of uranium nitride prepared by SPS technique

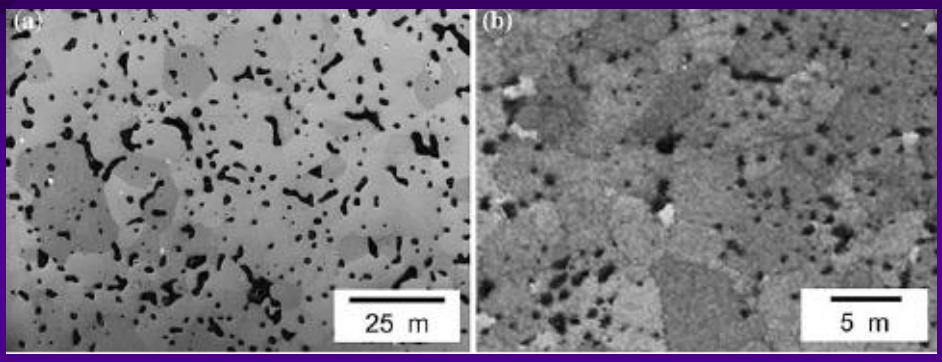

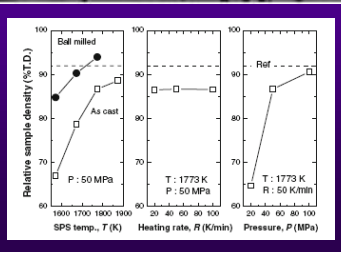

polished sample surface prepared by (a) conventional sintering method and (b) SPS technique

Division of Sustainable Energy and Environmental Engineering, Graduate School of Engineering, Osaka University,

Graphene-induced strengthening in spark plasma sintered tantalum carbide–nanotube composite

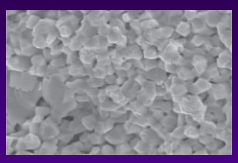

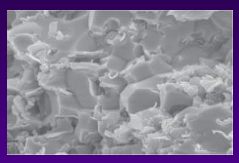

Fracture surfaces for TaC, TaC–LC and TaC–SC

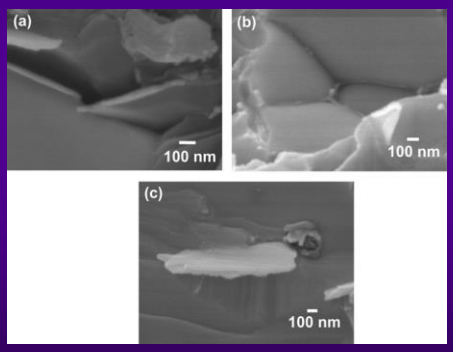

High-magnification SEM micrographs of TaC–SC fracture surface revealing: (a) transformed graphene platelets with straight edges; (b) graphene platelets sandwiched at TaC grain boundaries; (c) pulledout graphene platelet forming a strong interface with the TaC matrix

The SPS was carried out in an argon atmosphere at 1850 C and 100 MPa

Debrupa Lahiri, Evan Khaleghi, Srinivasa Rao Bakshi, Wei Li, Eugene A. Olevsky, and Arvind Agarwal, Graphene-induced strengthening in spark plasma sintered tantalum carbide–nanotube composite, Scripta Materialia 68 (2013) 285–288

SEM OF FRACTURE SURFACES: HUMAN DENTIN

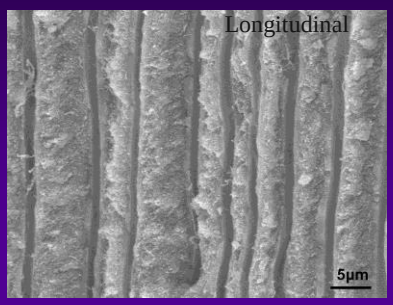

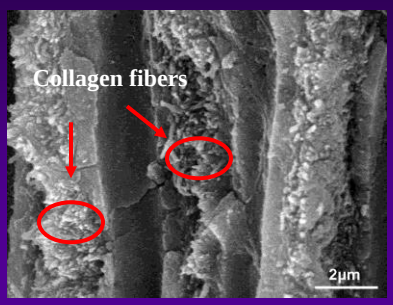

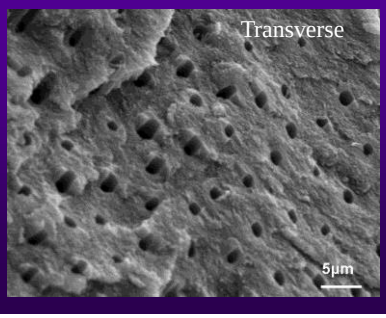

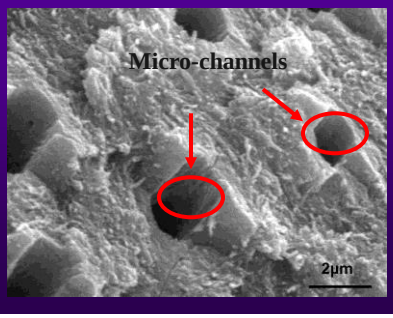

SPARK-PLASMA SINTERING OF HAP POWDER

- **Hydroxyapatite($Ca_{10}(PO_4)_6(OH)_2$), 0.5μ**
- **Melting point: 1670^0C, density: 3.14g/cm^3**
- **The main component in human bones and teeth**

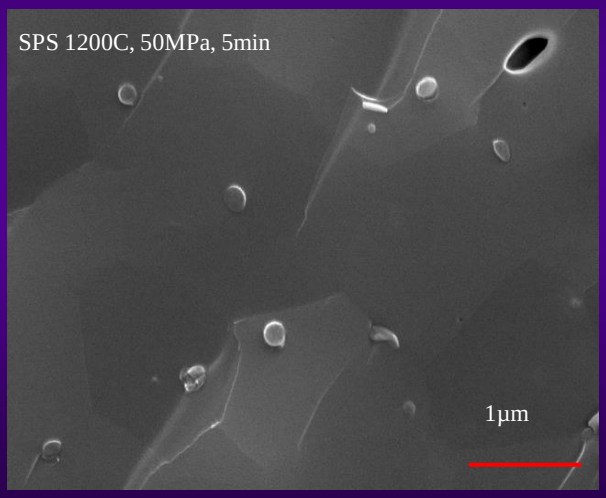

SEM IMAGES OF MICRO CHANNEL STRUCTURE AFTER FPSPS

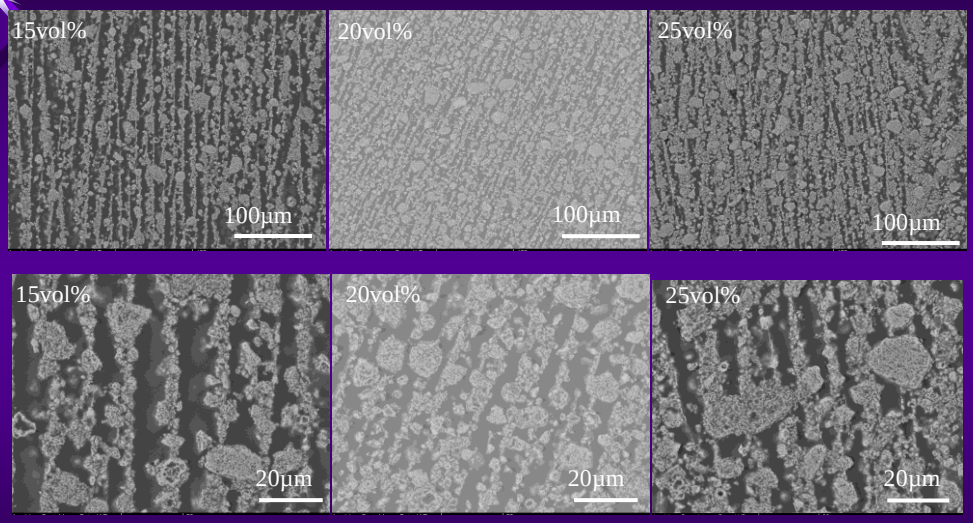

The channel diameters decrease with the increase of the initial slurry concentration

Y.-S. Lin, M. A. Meyers, and E. A. Olevsky, Microchannelled hydroxyapatite components by sequential freeze drying and free pressureless spark plasma sintering, *Adv. App. Ceram.*, 111, 269-274 (2012)

SPS-FPSPS PROCESSING SEQUENCE

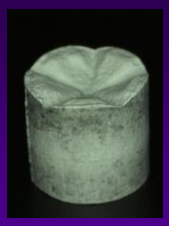

Complex shape HAp-based dental implant prototype produced by SPS-FPSPS sequence

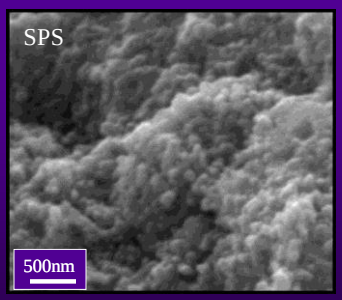

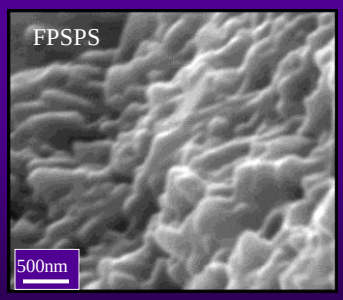

Y.-S. Lin, M. A. Meyers, and E. A. Olevsky, Microchannelled hydroxyapatite components by sequential freeze drying and free pressureless spark plasma sintering, *Adv. App. Ceram.*, 111, 269-274 (2012)

Comparative study of SPS – HP of hypereutectic Al-Si-Fe-X powder

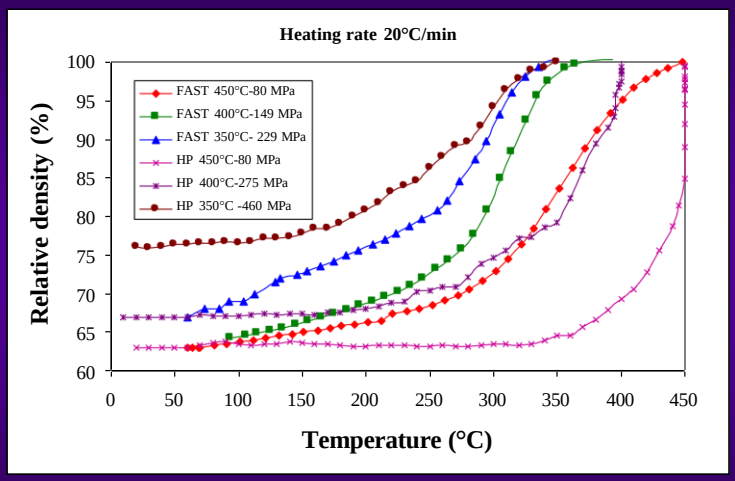

E. Olevsky, S. Kandukuri, and L. Froyen, Consolidation enhancement in spark-plasma sintering: Impact of high heating rates, *J. App. Phys.*, 102, 114913-114924 (2007)

SPS: ENHANCEMENT OF MASS TRANSPORT

Thermal Effects in SPS

- high heating rates
- high local non-uniformities of temperature distribution (local melting and sublimation)
- macroscopic temperature gradients
- thermal diffusion
- thermal stresses

Field Effects in SPS

- electromigration (diffusion enhancement)
- electroplasticity (electron wind, magnetic depinning of dislocations)
- dielectric breakdown of oxide films at grain boundaries
- ponderomotive forces
- "pinch effect"
- surface plasmons

E. Olevsky and L. Froyen, Constitutive modeling of spark-plasma sintering of conductive materials, *Scripta Mater*., 55, 1175-1178 (2006)
E. Olevsky, S. Kandukuri, and L. Froyen, Consolidation enhancement in spark-plasma sintering: Impact of high heating rates, *J. App. Phys*., 102, 114913-114924 (2007)
E. Olevsky and L. Froyen, Influence of thermal diffusion on spark-plasma sintering, *J. Amer. Ceram. Soc*., 92, S122-132 (2009)

SPS: Influence of High Heating Rates

- Experimentally, it has been shown in a number of investigations that an increase in heating rate considerably increases the consolidation rate of conductive and non-conductive powders during SPS.
- For example, it was shown for an alumina powder (Zhou *et al*.) that the increase of heating rate from 50 to 300°C/min with the same maximum temperature and the corresponding six time decrease of sintering time allowed obtaining the same final density. Physically, this was attempted to be explained as a result of the existence of additional defects in the material directly related to high heating rates and short time of the process. They could be initial "biographic" defects resulting from processes of powder synthesis (Ivensen or defects in grain-boundaries between particles (Dabhade *et al*.).
- Gillia and Bouvard have conducted a series of fundamental comparative experiments on sintering of WC-Co powder system with different heating cycles. They employed cycles with the same average heating rate but with various temperature histories (by employing sequences of steady ramps and isothermal periods). Their results indicate the dependence of the densification rate on the average heating rate but no dependence on the temperature history.

SPS: Micromechanical Model

$$r_a = \frac{c_p^2}{a_p} \qquad r_c = \frac{a_p^2}{c_p}$$

$$\sigma_x = b_{1x} \cdot y^2 + b_{2x} \cdot y + b_{3x}$$

$$\sigma_y = b_{1y} \cdot x^2 + b_{2y} \cdot x + b_{3y}$$

$$\int_0^a \sigma_x dx = -\alpha \sin\frac{\phi}{2} - \left(\bar{\sigma}_x \frac{c+c_p}{c}\right) \cdot c$$

$$\sigma_x(c) = \frac{\alpha}{r_c};$$

$$\nabla\sigma_x(0) = \frac{\partial \sigma_x}{\partial y}(y=0) = 0$$

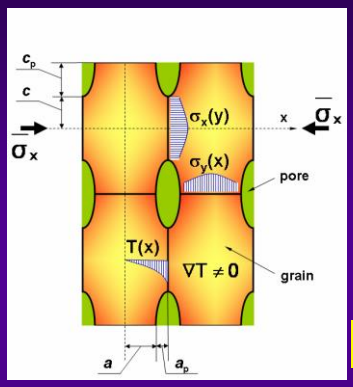

E. A. Olevsky, B. Kushnarev, A. Maximenko, V. Tikare and M. Braginsky, Modelling of anisotropic sintering in crystalline ceramics, *Philosophical Magazine*, 85, (19), 2123-2146 (2005)

J_y^{gb} is the flux of matter in the direction of the axis *y* caused by the grain boundary diffusion, D_{gb} is the coefficient of the grain boundary diffusion, δ_{gb} is the grain boundary thickness, *k* – Boltzman constant; *T* – absolute temperature.

$$J_y^{gb} = \frac{\delta_{gb} D_{gb}}{kT}\left[\frac{\partial \sigma_x}{\partial y}\right]$$

$$\dot{\varepsilon}_{gbx} = -\frac{J_y^{gb}(c)}{2(a+a_p)(c+c_p)}\Omega$$

where α is the surface tension, ϕ is the dihedral angle, *a* and *c* are the grain semi-axes; $\bar{\sigma}_x$ - effective (far-field) external stress in the x-direction (compressive $\bar{\sigma}_x$ is negative). Parameter $\bar{\sigma}_x \frac{c+c_p}{c}$ is a local stress on the grain boundary ($\frac{c+c_p}{c}$ is the stress concentration factor).

$$\dot{\varepsilon}_{gbx} = -\frac{\delta_{gb} D_{gb}}{kT}\frac{\Omega}{(a+a_p)(c+c_p)}\left\{\left[\frac{3\alpha}{c}\left[\frac{1}{r_c} - \frac{1}{c}\sin\frac{\phi}{2}\right] - \bar{\sigma}_x \frac{c+c_p}{c^2}\right]\right\}$$

$$\sigma_x = \left\{\left[\frac{3\alpha}{2c^2}\left[\frac{1}{r_c} + \frac{1}{c}\sin\frac{\phi}{2}\right] + \frac{3}{2c^3}\bar{\sigma}_x(c+c_p)\right]\right\} y^2 + \alpha\left[-\frac{3}{2\cdot c}\sin\frac{\phi}{2} - \frac{1}{2}\frac{1}{r_c}\right] - \frac{3}{2c}\bar{\sigma}_x(c+c_p)$$

SPS: Influence of High Heating Rates

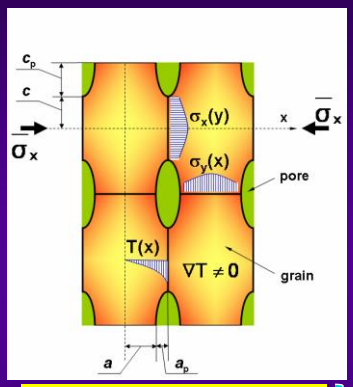

E. Olevsky, S. Kandukuri, and L. Froyen, Consolidation enhancement in spark-plasma sintering: Impact of high heating rates, *J. App. Phys*. 102, 114913-114924 (2007)

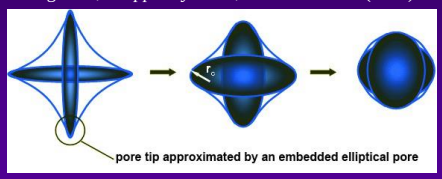

$$\dot{\varepsilon}_x = \dot{\varepsilon}_{gbx} + \dot{\varepsilon}_{crx} = f(\theta, \xi, G)$$

$$\dot{\xi} = \frac{3\delta_s D_s \alpha \Omega}{8kTG^4\xi^2}\left(1-\xi^2\right)\left(\sqrt{(1-\xi)^2 + \frac{\pi}{\theta}\xi} - (1+\xi)\right)^4$$

$$\frac{\dot{\theta}}{1-\theta} = \dot{e} = \dot{\varepsilon}_x$$

$$\dot{G} = \begin{cases} 6.67\times10^{-4}\left(\frac{1}{^\circ K}\right)\varpi \ln\frac{235^\circ K/s}{\varpi} G_0 \left(\frac{G_0}{G}\right)^3 \theta^{-1.34}, & if \quad T > 533^\circ K \\ 0, \quad if \quad T \le 533^\circ K \end{cases}$$

$\varpi = \frac{dT}{dt} = const$ is the heating rate, °K/s

Du and Cocks

$$\dot{G} = \dot{G}_0^{fd}\left(\frac{G_0}{G}\right)^3 \theta^{-1.34}$$

Beck et al.

$$G^{fd} = G_0^{fd} e^{6.67\times10^{-4}T - 3.55\times10^{-3}}$$

For an aluminum alloy powder

$\dot{G}$ is the porous material's grain growth rate, G_0^{fd} is the grain growth rate of the fully-dense material with the grain size G_0, G_0 is the initial grain size of the porous (powder) material

G^{fd} is the current grain size of the fully-dense material; G_0^{fd} is the initial grain size of the fully-dense material; *t* is time, s; and *T* is temperature, °K

SPS: Influence of High Heating Rates

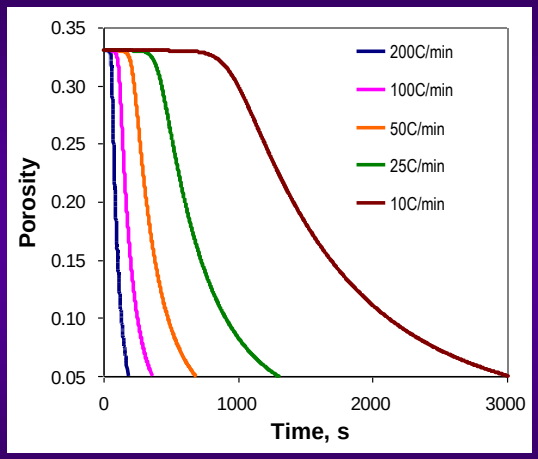

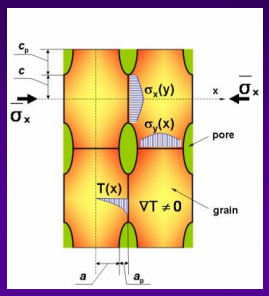

For aluminum powder

E. Olevsky, S. Kandukuri, and L. Froyen, Consolidation enhancement in spark-plasma sintering: Impact of high heating rates, *J. App. Phys*., 102, 114913-114924 (2007)

55

55

SPS: Influence of High Heating Rates

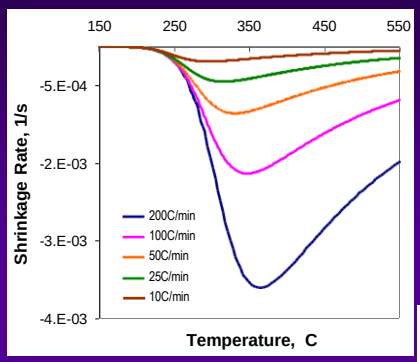

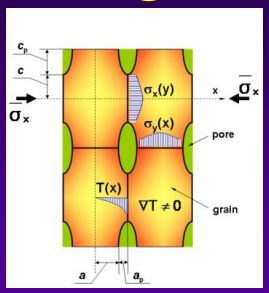

Model

Experiment

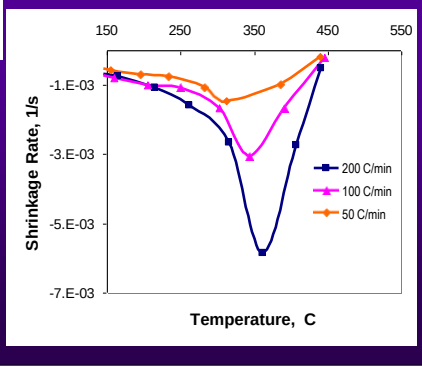

E. Olevsky, S. Kandukuri, and L. Froyen, Consolidation enhancement in spark-plasma sintering: Impact of high heating rates, *J. App. Phys*., 102, 114913-114924 (2007)

For aluminum powder

56

56

SPS: Influence of Thermal Diffusion

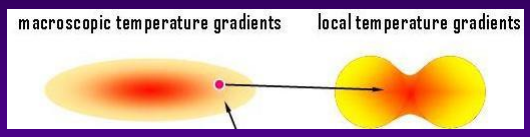

$$J = -D\left(\nabla C_v + C_v \frac{Q^*}{kT}\frac{\nabla T}{T}\right)$$

J is the vacancy flux, D is the coefficient of diffusion, C_v is the vacancy concentration, ∇C_v is the vacancy concentration gradient, Q^* is the heat of vacancy transport, ∇T is the temperature gradient.

E. Olevsky and L. Froyen, Influence of thermal diffusion on spark-plasma sintering, J. Amer. Ceram. Soc. 92, S122-132 (2009)

57

57

SPS: Influence of Thermal Diffusion

- Ludwig-Soret effect of thermal diffusion causes concentration gradients in initially homogeneous two-component systems subjected to a temperature gradient.

  J. Chipman, The Soret effect, *Journal of the American Chemical Society*, 48, 2577-2589 (1926)

- For the case of atomic and vacancy diffusion in crystalline solids, this effect was studied by a number of authors including it's theoretical interpretation by Shewmon and Schottky.

  P. Shewmon, Thermal diffusion of vacancies in zinc, *Journal of Chemical Physics*, 29, (5), 1032-1036 (1958)

  G. Schottky, A theory of thermal diffusion based on lattice dynamics of a linear chain, *Physica Status Solidi*, 8, (1), 357 (1965)

- For the electric-current assisted sintering, the effect of thermal diffusion was analyzed by Kornyushin and co-workers. Later, for rapid densification, the role of temperature gradients was studied by Searcy and by Young and McPherson.

  Y. V. Kornyushin, Influence of external magnetic and electric-fields on sintering, structure and properties, *Journal of Materials Science*, 15, (3), 799-801 (1980)

  A. W. Searcy, Theory for sintering in temperature-gradients - role of long-range mass-transport, *Journal of the American Ceramic Society*, 70, (3), C61-C62 (1987)

  R. M. Young and R. McPherson, Temperature-gradient-driven diffusion in rapid-rate sintering, *Journal of the American Ceramic Society*, 72, (6), 1080 (1989)

- Johnson argued against thermal diffusion significance in microwave sintering

  D. L. Johnson, Microwave-heating of grain-boundaries in ceramics, *Journal of the American Ceramic Society*, 74, (4), 849-850 (1991)

- We demonstrate a possible significance of thermal diffusion for SPS

  E. Olevsky and L. Froyen, Influence of thermal diffusion on spark-plasma sintering, *J. Amer. Ceram. Soc.* 92, S122-132 (2009)

58

58

SPS: Influence of Thermal Diffusion

Schottky: $$J = -D\left(\nabla C_v + C_v \frac{Q^*}{kT}\frac{\nabla T}{T}\right)$$

Young & McPherson: $$\nabla C = \frac{C_v H_f}{kT^2}\nabla T$$

$$J = -\frac{DC_v}{kT}\left(H_f + Q^*\right)\frac{\nabla T}{T}$$

Wirtz: $$Q^* = H_m - H_f$$

$$J = -\frac{DC_v}{kT} H_m \frac{\nabla T}{T}$$

J is the vacancy flux, D is the coefficient of diffusion, C_v is the vacancy concentration, ∇C_v is the vacancy concentration gradient, Q^* is the heat of vacancy transport, ∇T is the temperature gradient.
H_m is the enthalpy of vacancy migration;
H_f is the enthalpy of vacancy formation

Kornyushin: $$\kappa_T' = \frac{C_v\left(H_m - H_f\right)}{k\langle T\rangle}; \quad J = -D\frac{\kappa_T'}{\langle T\rangle}\nabla T$$

κ_T' is the thermal diffusion ratio ($\langle T\rangle$ is the spatial average of temperature)

did not include the term ∇C_v! Otherwise:

Heat transfer equation:

$$\lambda_T \Delta T = C\frac{\partial T}{dt} - q$$

λ_T is the thermal conductivity; C is heat capacity; t is time; and q is the heat production per unit volume of the material and per unit time, which in the case of SPS can be represented as $q = \lambda_e E^2$, where λ_e is the specific electric conductivity, and E is the electric field intensity

We re-define: $$\kappa_T = \frac{C_v H_m}{k\langle T\rangle}$$

The driving force for the vacancy migration: $$divJ = -D\frac{\kappa_T}{\langle T\rangle}\Delta T$$

$$divJ = -D\frac{\kappa_T}{\lambda_T\langle T\rangle}\left(C\frac{\partial T}{\partial t} - \lambda_e E^2\right)$$

E. Olevsky and L. Froyen, Influence of thermal diffusion on spark-plasma sintering, J. Amer. Ceram. Soc. 92, S122-132 (2009)

59

59

SPS: Influence of Thermal Diffusion

$$divJ = -D\frac{\kappa_T}{\lambda_T\langle T\rangle}\left(C\frac{\partial T}{\partial t} - \lambda_e E^2\right)$$

$$J_{td}^{gb} = 2\left(divJ\right)G = -2\delta_{gb}D_{gb}\frac{\kappa_T}{\lambda_T\langle T\rangle}\left(C\frac{\partial T}{\partial t} - \lambda_e E^2\right)G$$

λ_T is the thermal conductivity; C is heat capacity; t is time; and q is the heat production per unit volume of the material and per unit time, which in the case of SPS can be represented as $q = \lambda_e E^2$, where λ_e is the specific electric conductivity, and E is the electric field intensity

$$\dot{\varepsilon}_{gbx}^{td} = -\frac{J_{td}^{gb}\Omega}{2\left(G + r_p\right)^2} = \frac{\delta_{gb}D_{gb}\kappa_T\Omega}{\lambda_T\langle T\rangle}\left(C\frac{\partial T}{\partial t} - \lambda_e E^2\right)\frac{G}{\left(G + r_p\right)^2}$$

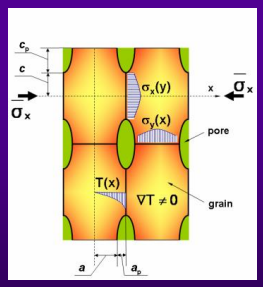

$$\dot{\varepsilon}_x = \dot{\varepsilon}_{gbx}^{curvature\ \ driven} + \dot{\varepsilon}_{gbx}^{th\_diffusion\ \ driven} + \dot{\varepsilon}_{crx} = f\left(\theta, G\right)$$

$$\frac{\dot{\theta}}{1-\theta} = \dot{e} = \dot{\varepsilon}_x$$

θ is porosity; G is the average grain size

$$\dot{G} = \left(1.5\times10^{-10}\, m/s\right)\left(\frac{G_0}{G}\right)^3 \theta^{-1.34}$$

E. Olevsky and L. Froyen, Influence of thermal diffusion on spark-plasma sintering, J. Amer. Ceram. Soc. 92, S122-132 (2009)

60

60

SPS: Influence of Thermal Diffusion

$$\frac{\dot{\theta}}{1-\theta} = \dot{\varepsilon}_{gbs} = -\frac{9\alpha\delta_{gb}D_{gb}\Omega}{4\pi kTG^2}\frac{\left(\sqrt{\pi}-2\sqrt{\theta}\right)^3\sqrt{\theta}}{1-\theta}\left\{\left(\sqrt{\pi}-3\sqrt{\theta}\right)-\frac{2\sqrt{\pi\theta}\left(\frac{\bar{\sigma}_s G}{\alpha}\right)}{9(1-\theta)^2\left(\sqrt{\pi}-2\sqrt{\theta}\right)}\right\}-\left\{\frac{\alpha G_{ref}^{\,3}}{A_0\exp\left(\frac{Q_{cr}}{RT}\right)G^4}\frac{\left(\frac{3\theta}{2}\right)^{\frac{m+1}{2}}\left[\frac{3}{2}(1-\theta)^2-\frac{\bar{\sigma}_s G}{\alpha}\right]}{(1-\theta)^{\frac{m+3}{2}}}\right\}^{\frac{1}{m}}-$$

$$\frac{\delta_{gb}D_{gb}\Omega C_v H_m}{\lambda_T k\langle T\rangle^2}\left(C\frac{\partial T}{\partial t}-\lambda_e E^2\right)\frac{3\left(\sqrt{\pi}-2\sqrt{\theta}\right)^2\theta}{2\pi G(1-\theta)}$$

curvature-driven grain boundary diffusion **thermal diffusion** **power-law creep**

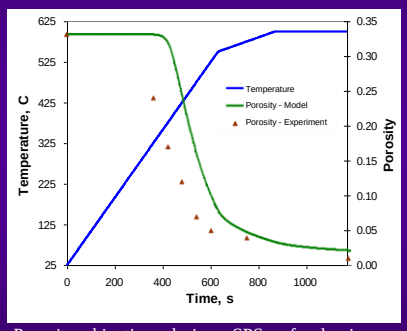

Porosity kinetics during SPS of aluminum powder. Comparison of the developed model taking into account the impact of thermal diffusion with experimental data of Xie *et al.*, Effect of interface behavior between particles on properties of pure al powder compacts by spark plasma sintering, *Materials Transactions*, 42, (9), 1846-1849 (2001)

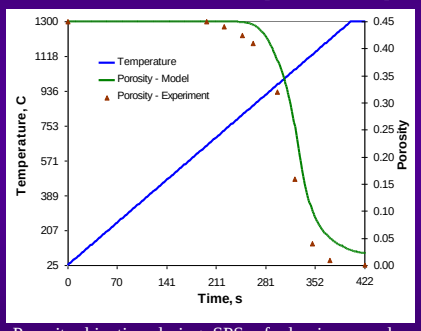

Porosity kinetics during SPS of alumina powder. Comparison of the developed model taking into account the impact of thermal diffusion with experimental data of Shen *et al.*, Spark plasma sintering of alumina, *J. Amer. Ceram. Soc.*, 85, (8), 1921 (2002)

SPS: Influence of Thermal Diffusion

$$J = -D\frac{\kappa_T}{\langle T\rangle}\nabla T$$

- The intensity of thermal diffusion increases for higher pulse frequencies.
- The thermal diffusion promotes components' (atoms and vacancies) separation. At early stages of sintering, this should lead to the growth of inter-particle necks, which corresponds to the enhancement of sintering. At the final stages of sintering, however, the pores may serve as vacancy sinks under thermal diffusion conditions, which impedes sintering.
- It is possible that the increased pulse frequencies *enhance sintering at the early stages* of SPS and *hinder sintering at the late stages* of SPS process.
- In some experimental studies the pulse frequency was found to have a limited impact on SPS results - its contributions at early and late stages of SPS could offset each other.

E. Olevsky and L. Froyen, Influence of thermal diffusion on spark-plasma sintering, J. Amer. Ceram. Soc. 92, S122-132 (2009)

Major Components of Densification-Contributing Mass Transfer During SPS (model including electromigration):

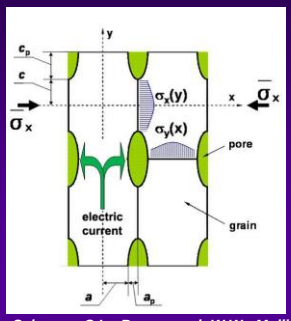

- ***M. Scherge, C.L. Bauer, and W.W. Mullins, Acta Met. Mater., 43 (9), 3525-3538 (1995):*** electromigration stress of 23MPa along grain boundaries under an electric field of 500 V/m (in a 1-thick film) and up to GPa range stresses for grain structures with closed surface junctions
- ***M.R. Gungor and D. Maroudas, Int. J. Fracture, 109 (1), 47-68 (2001):*** electromigration stress of 140MPa in a 1 -thick film under the field of about 425 V/m
- ***Q.F. Duan and Y.L. Shen, J. Appl. Phys. 87 (8), 4039-4041 (2000):*** electromigration stress of 450MPa along fast-diffusion length of 15 under 650 V/m
- ***Z. Suo, Q. Ma, and W.K. Meyer, MRS Symposium Proceedings, 6p. (2000):*** electromigration stress in 0.5 -thick Al film under 300 V/m field should reach the level of 1.5GPa

grain-boundary diffusion — power-law creep

driving sources

externally applied load — sintering stress — electromigration

Nernst-Einstein equation

$$\vec{\mathbf{J}} = C_E \vec{\mathbf{E}} + C_\sigma \vec{\nabla}\sigma$$

Blech's formula

$$C_E = \frac{\delta_{gb} D_{gb}}{\Omega k T} Z^* e_q \qquad C_\sigma = \frac{\delta_{gb} D_{gb}}{kT}$$

where Ω is the atomic volume, Z^* is the valence of a migrating ion, and e_q is the electron charge (the product $Z^* e_q$ is called "the effective charge").

$$J_y^{gb} = \frac{\delta_{gb} D_{gb}}{kT}\left[\frac{1}{\Omega} Z^* e_q \frac{U}{l} + \frac{\partial \sigma_x}{\partial y}\right] \qquad \dot{\varepsilon}_{gbx} = -\frac{J_y^{gb}(c)}{2(a+a_p)}\frac{\Omega}{c}$$

U and l are the electric potential and the characteristic length along the electric field.

$$\dot{\varepsilon}_{gbx} = -\frac{\delta_{gb} D_{gb}}{kT}\frac{\Omega}{(G+r_p)^2}\left\{\frac{Z^* e_q}{\Omega}\frac{U}{l} + \frac{3\alpha}{G}\left[\frac{1}{r_p} - \frac{1}{2G}\right] - \bar{\sigma}_x \frac{G+r_p}{G^2}\right\}$$

α is the surface tension, $\bar{\sigma}_x$ - effective (far-field) external stress in the x-direction

$G = a = c$ is the grain size, $r_p = a_p = c_p$ is the pore radius.

Constitutive Model of Spark-Plasma Sintering Including Electromigration

shrinkage due to grain-boundary diffusion

shrinkage due to dislocation creep

$$\dot{\varepsilon}_x = \dot{\varepsilon}_{gbx} + \dot{\varepsilon}_{crx} = -\frac{\delta_{gb} D_{gb}}{kT}\frac{\Omega}{(G+r_p)^2}\left\{\frac{Z^* e_q}{\Omega}\frac{U}{l} + \frac{3\alpha}{G}\left[\frac{1}{r_p} - \frac{1}{2G}\right] - \bar{\sigma}_x \frac{G+r_p}{G^2}\right\} - \left\{\left(\frac{3\theta}{2}\right)^{\frac{3}{2}}\left[\frac{3\alpha}{2G}(1-\theta)^2 - \bar{\sigma}_x\right] \Big/ A(1-\theta)^{\frac{5}{2}}\right\}^{\frac{1}{m}}$$

G is the grain size; r_p is the pore radius; A and m are power-law creep frequency factor and power-law creep exponent, respectively; D_{gb} is the coefficient of the grain boundary diffusion, δ_{gb} is the grain boundary thickness, k is the Boltzman's constant, T is the absolute temperature; Ω is the atomic volume, Z^* is the valence of a migrating ion, and e_q is the electron charge (the product $Z^* e_q$ is called "the effective charge"); U and l are the electric potential and the characteristic length along the electric field; α is the surface tension; $\bar{\sigma}_x$ - effective (far-field) external stress in the x-direction; θ is porosity.

E. Olevsky and L. Froyen, Constitutive modeling of spark-plasma sintering of conductive materials, *Scripta Mater.* 55, 1175-1178 (2006)

Shrinkage kinetics during SPS of aluminum powder: comparison with experiments

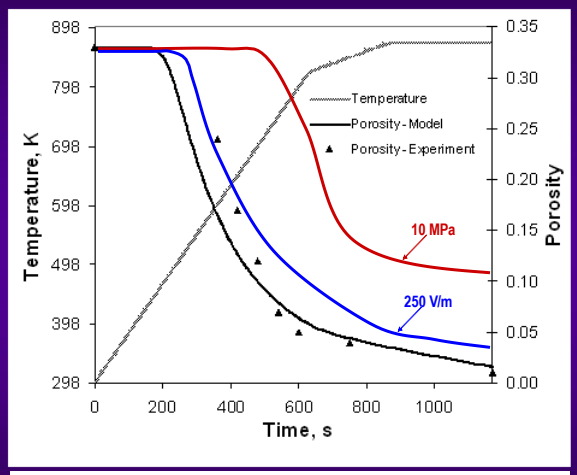

The average particle size is 55μm. The applied field is accepted to be of $500\frac{V}{m}$ (Joule heat generation balance –based estimation), the pressure is constant and equal to 23.5 MPa.

E. Olevsky and L. Froyen, Constitutive modeling of spark-plasma sintering of conductive materials, *Scripta Mater.* 55, 1175-1178 (2006)

Contribution of different factors to shrinkage under SPS

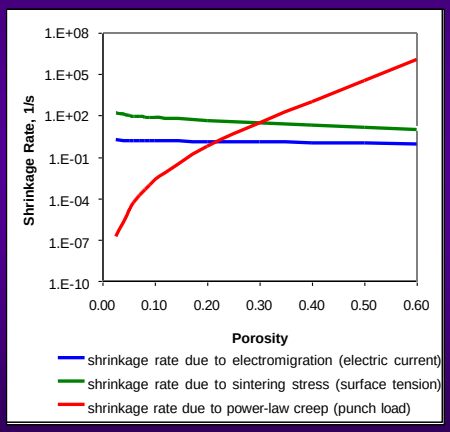

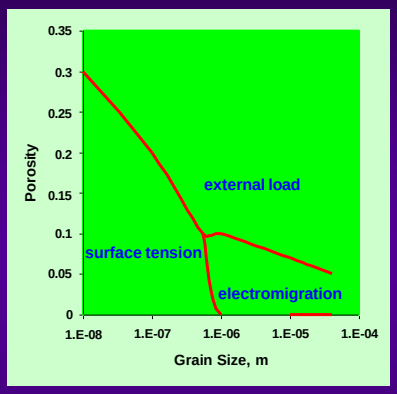

Densification map for aluminum powder, T=673K, =28.3MPa

E. Olevsky and L. Froyen, Constitutive modeling of spark-plasma sintering of conductive materials, *Scripta Mater.* 55, 1175-1178 (2006)

Contribution of different factors to shrinkage rate of aluminum powder under SPS

$\frac{U}{l} = 417\frac{V}{m}$, T=673^{0}K, $\bar{\sigma}_x$ =28.3MPa

Coupled electro-thermo-mechanical FEM calculations

$$-\nabla \cdot (\sigma_{el} \nabla V) = 0$$

Conductive DC

$$\rho C_p \frac{\partial T}{\partial t} - \nabla \cdot (k_T \nabla T) = \sigma_{el} \left| \nabla V \right|^2$$

Heat Transfer by Conduction

$$\sigma_{ij} = \frac{\sigma(W)}{W} \left[\varphi \dot{\varepsilon}_{ij} + \left(\psi - \frac{1}{3} \varphi \right) \dot{e} \delta_{ij} \right] + P_L \delta_{ij}$$

Stress-Strain Analysis

$$\frac{\dot{\theta}}{1-\theta} = \dot{e}$$

Densification

D. Giuntini, J. Raethel, M. Herrmann, A. Michaelis, E. A. Olevsky, Advancement of tooling for spark-plasma sintering, *J. Amer. Ceram. Soc.*, 98 (11), 3529-3537 (2015)

TEMPERATURE DISTRIBUTION DURING SPS

prismatic die

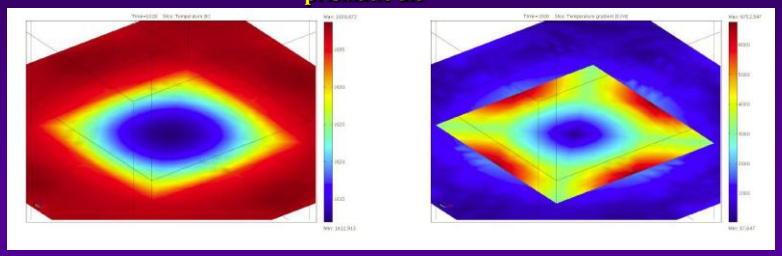

temperature | temperature gradient

cylindrical die

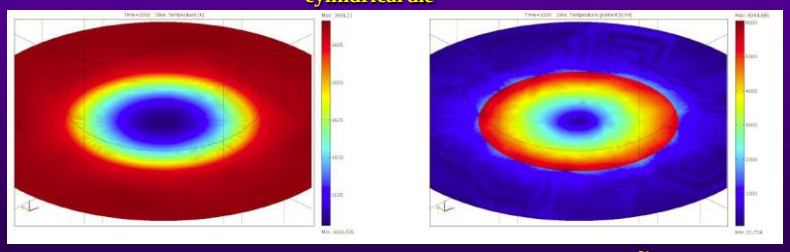

temperature | temperature gradient

The Problem Overheating of SPS Tooling

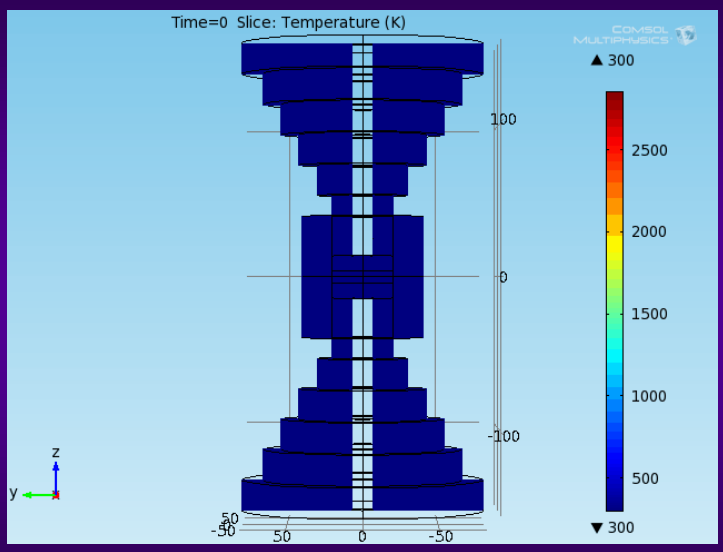

D. Giuntini, E. A. Olevsky, C. Garcia-Cardona , A. L. Maximenko, M. S. Yurlova, C.D. Haines, D. G. Martin, and D. Kapoor, Localized Overheating Phenomena and Optimization of Spark-Plasma Sintering Tooling Design, *Materials*, 6, 7, 2612-2632 (2013)

Experimental Setup: SPS Tooling for Current-assisted and Current-insulated Free SPS-Forging

Current-assisted mode | **Current-insulated mode**

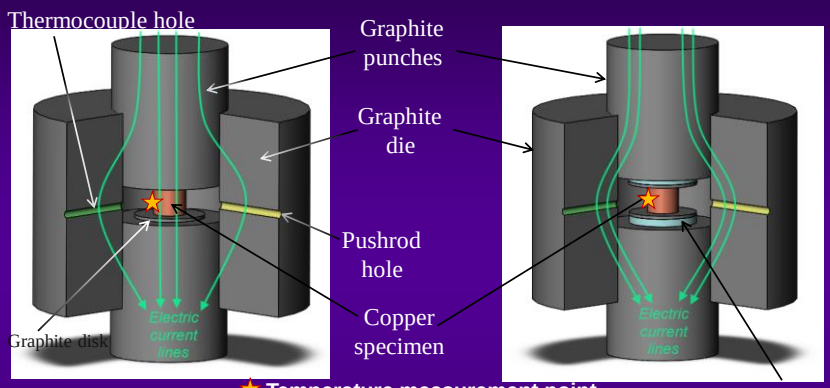

★ **Temperature measurement point**

Electrical isolative inserts

Advantages of the SPS-Tooling for the Free SPS-forging:

- ✓ **Direct Heating Control**: heating control directly at the specimen's surface
- ✓ Bi-axial dilatometry: *In-situ* measurement of the sample's height and radius
- ✓ Equal weight of the powder

E.A. Olevsky et al., Contribution of electric current into densification kinetics during spark-plasma sintering of conductive powder, *J. Amer. Ceram. Soc.*, 98 (11), 3509-3517 (2015)

SPS-Forging: In-Situ Observation

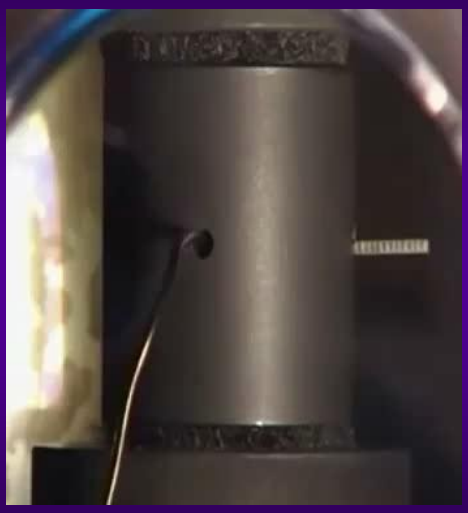

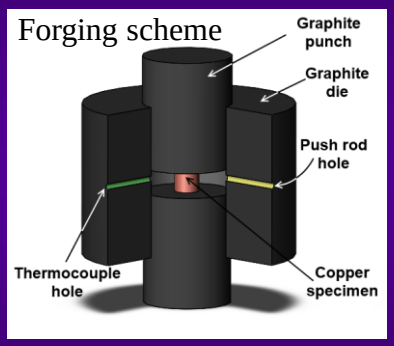

E.A. Olevsky *et al*., Contribution of electric current into densification kinetics during spark-plasma sintering of conductive powder, *J. Amer. Ceram. Soc*., 98 (11), 3509-3517 (2015)

Comparative Sample Analysis: Current-Assisted vs. Current-Insulated SPS-Forging

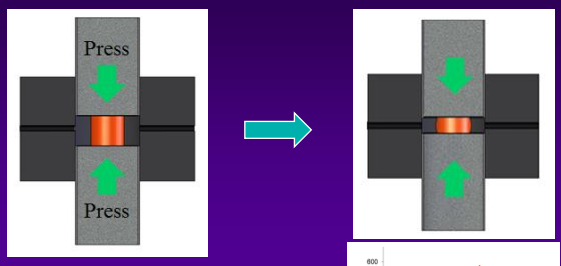

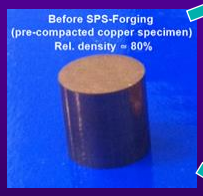

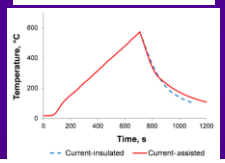

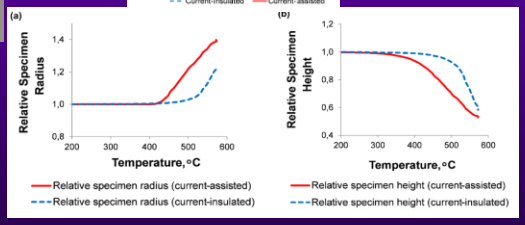

E.A. Olevsky *et al*., Contribution of electric current into densification kinetics during spark-plasma sintering of conductive powder, *J. Amer. Ceram. Soc*., 98 (11), 3509-3517 (2015)

Spark Plasma Sintering (SPS) vs Hot Pressing (HP)

SPS

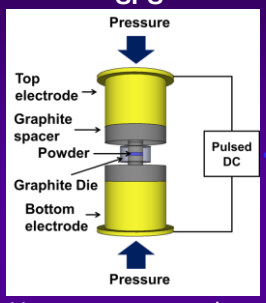

Heat, pressure, and electric current

Lee, McKittrick, Olevsky et al., Ceram. Int. (2014)

Hot pressing (HP)

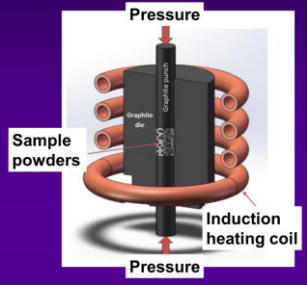

Heat and Pressure

Henriques et al. Gold Bull (2013)

Possible intrinsic current effects

1. Surface cleaning effect
2. Electromigration
3. Electroplastic effect
4. Change of densification mechanism

Groza et al., Mater. Sci. Eng. A, (2000)
Frei et al., J. Appl. Phys., (2007)
Roth et al., Trans. North Am. Manuf. Res. Inst. SME., (2008)
Garay et al., Appl. Phys. Lett., (2004)
Langer et al., J. Am. Ceram. Soc., (2011)

Advantages of SPS

- Fast densification
- Lower sintering temperature
- High heating rate (~ 300 °C/min)
- Grain growth prevention

What are the electric current effects on the densification mechanism in SPS?

CONSTITUTIVE EQUATION OF HP

- Power-law creep (deformation of solid) + Constitutive equation for sintering (deformation of porous material)

$$\left(\frac{\sigma}{G}\right)^n = \frac{\dot{\varepsilon} kT}{A_{Cr} DGb}\left(\frac{d}{b}\right)^p$$

$\dot{\varepsilon}$: Steady-state creep rate (1/s)
k : Boltzmann's constant (J/K),
D : Diffusion coefficient (cm2/s),
G : Shear modulus(MPa),
T : Absolute temperature (K),
b : Burgers vector (m),
σ : Applied stress (MPa),
A_{cr} : Material constant for creep,
d : Grain size (m),
p : Grain size exponent,
n : Stress exponent (n is equal to 1/m, where m is the strain rate sensitivity)

$$\sigma(W) = G\left\{\frac{A_0 T}{G}\exp\left(\frac{Q}{RT}\right)\right\}^m \left(\frac{d}{b}\right)^{pm} W^m$$

$$D = D_0 \exp\left(\frac{-Q}{RT}\right)$$

$$A_0 = \frac{k}{A_{Cr} b D_0}$$

D0 : Diffusion constant (cm^2/s),
Q : Activation energy for the creep (kJ/mol),
R : Gas constant

< Creep mechanism >

n : Stress exponent (n is equal to 1/m, where m is the strain rate sensitivity)

1. Diffusion creep: n=1 (m=1)
2. Grain boundary sliding: n=2 (m=0.5)
3. Dislocation creep
   a. Glide controlled creep: n=3 (m=0.33)
   b. Climb controlled creep: n=4~5 (m=0.2~0.25)
4. Dispersion strengthened alloys: n>8 (m<0.1)

Nieh, T.G. Wadsworth, J. Sherby, O.D., Superplasticity in Metals and Ceramics, (1997)

Constitutive equation for HP

$$\dot{\theta} = -\left[\frac{G}{A_0 T}\left(\frac{b}{d}\right)^p \exp\left(\frac{-Q}{RT}\right)\right]\left(\frac{3\theta}{2}\right)^{\frac{m+1}{2m}}(1-\theta)^{\frac{m-3}{2m}}\left(\frac{\sigma_z}{G}\right)^{\frac{1}{m}}$$

$\dot{\theta}$: Densification rate (1/s)
θ : Porosity

Olevsky, Mater. Sci. Eng., (1998)
Lee, McKittrick, and Olevsky et al., Ceram. Int., (2015)
Lee, McKittrick, and Olevsky et al., Int. J. Refract. Met. H., (2016)

Electroplasticity Theory

- Reduction of the material flow stress under electric current or field

1. Metal deformation at low T

$$\dot{\gamma} = \dot{\gamma}_0 \exp(\frac{-\Delta H}{kT}) = \rho_m A_s b \nu_d s \exp(\frac{-\Delta S}{k}) \exp(\frac{-\Delta H}{kT})$$

→ Electric current affects ρm, νd , As, or ΔS

Conrad, Mater. Sci. Eng. A., (2002)

2. Ceramic deformation at high T

$$\left(\frac{\sigma}{G}\right)^n = \frac{\dot{\varepsilon} kT}{A_{Cr} DGb}\left(\frac{d}{b}\right)^p \qquad D = D_0 \exp\left(\frac{-Q}{RT}\right)$$

→ Electric current affects D0 or Q

Yang and Conrad, Scripta Mater., (1999)
Campbell et al., Metall and Mat Trans A., (1999)

ρ_m : Mobile dislocation density,
b : Magnitude of the Burgers vector (m),
A_s : Area of the slip plane swept out per successful thermal fluctuation,
ν_d : Frequency of vibration of the dislocation segment involved in thermal activation (1/s),
s : Average distance of the dislocation travel (m),
ΔS: Entropy of the activation,
ΔH: Activation enthalpy (KJ/mol),
T : Absolute temperature (K),
k : Boltzmann constant (J/K)

$\dot{\varepsilon}$: Steady-state creep rate (1/s)
k : Boltzmann's constant (J/K),
D : Diffusion coefficient (cm2/s),
G : Shear modulus(MPa),
σ : Applied stress (MPa),
A_{cr} : Material constant for creep(unitless),
d : Grain size (m),
p : Grain size exponent,
n : Stress exponent (n is equal to 1/m, where m is the strain rate sensitivity)
D_0 : Diffusion constant (cm^2/s),
Q : Activation energy for the creep(kJ/mol),
R : Gas constant

Cascade effects

Electric current → Local Joule heating at defects ⇔ Defect generation → Enhanced dislocation mobility

G. Lee, E.A. Olevsky, C. Manière, A. Maximenko, O. Izhvanov, C. Back, J. McKittrick, Effect of electric current on densification behavior of conductive ceramic powders consolidated by spark plasma sintering, *Acta Mater*., 144, 524-533 (2018)

Constitutive Equation of SPS

Constitutive equation of sintering for HP

$$\dot{\theta} = -\left[\frac{G}{A_0 T}\left(\frac{b}{d}\right)^p \exp(\frac{-Q}{RT})\right](\frac{3\theta}{2})^{\frac{m+1}{2m}}(1-\theta)^{\frac{m-3}{2m}}(\frac{\sigma_z}{G})^{\frac{1}{m}}$$

$$E_J = J^2 \lambda_d \Delta t$$

$$\dot{\theta} = -\left[\frac{G}{A_0 T}\left(\frac{b}{d}\right)^p \exp(\frac{-Q}{RT}) + \left[\int_{t_0}^{t_f} \frac{J^2 \lambda_d}{\tau_{PN}} dt\right]^{\omega}\right](\frac{3\theta}{2})^{\frac{m+1}{2m}}(1-\theta)^{\frac{m-3}{2m}}(\frac{\sigma_z}{G})^{\frac{1}{m}}$$

Constitutive equation of sintering for SPS

$$\dot{\theta} = -\left[\frac{G}{A_0 T}\left(\frac{b}{d}\right)^p \exp(\frac{-Q}{RT}) + \beta^{\omega}\left[\int_{t_0}^{t_f} \frac{J_{OL}{}^2 \lambda}{G} dt\right]^{\omega}\right](\frac{3\theta}{2})^{\frac{m+1}{2m}}(1-\theta)^{\frac{m-3}{2m}}(\frac{\sigma_z}{G})^{\frac{1}{m}}$$

$$W = W_{Thermal} + W_{Electric\ current\ assisted}$$

$$\dot{\theta} = -[A_{TD} + A_{ECAD}](\frac{3\theta}{2})^{\frac{m+1}{2m}}(1-\theta)^{\frac{m-3}{2m}}(\frac{\sigma_z}{G})^{\frac{1}{m}}$$

$$A_{TD} = \frac{G}{A_0 T}\left(\frac{b}{d}\right)^p \exp(\frac{-Q}{RT})$$

ATD: Thermal deformability of the powders during the sintering (1/s)

$$A_{ECAD} = \beta^{\omega}\left[\int_{t_0}^{t_f} \frac{J_{OL}{}^2 \lambda}{G} dt\right]^{\omega}$$

AECAD: Electric current assisted deformability of the powders (1/s)

$\dot{\theta}$: Densification rate (1/s)
θ : Porosity
W: Total equivalent effective strain rate (1/s),
k : Boltzmann's constant (J/K),
D : Diffusion coefficient (cm2/s),
G : Shear modulus(MPa),
T : Absolute temperature (K),
b : Burgers vector (m),
σ_z : Z-axis applied stress (MPa),
Q : Activation energy (kJ/mol),
R : Gas constant
t_0, t_f : Starting and final time for SPS (s),
ω : Electric current sensitivity exponent,
τ_{PN} : Peiers-Nabarro stress (MPa),
J_{OL} : OLECD (A/m^2),
β : Electric current effect coefficient
d : Grain size (m),
p : Grain size exponent,
m : Strain rate sensitivity
λ : Electrical resistivity of defect free lattice

<Assumptions>

- Electric current affects A0 or Q
- Original energy : Local Joule heating at defects
- Defects generation effects are accumulated with time
- Dislocation movements are limited by Peiers-Nabarro stress

Lee, Olevsky et al., Acta Mater., (2018)

Determination of Electric Current Related Constitutive Parameters

- Three constitutive parameters related to electric current effect

AECAD: Electric current assisted deformability of the powders (1/s)

$$A_{ECAD} = \beta^{\omega} \left[\int_{t_0}^{t_f} \frac{J_{OL}^{2} \lambda}{G} dt \right]^{\omega}$$

- λ : Electrical resistivity of defect free lattice (Ω·m),
- t0, tf : Starting and final time for SPS (s),
- G : Shear modulus (MPa)

1. JOL : Local current density (A/m^2) → Known
2. ω : Electric current sensitivity exponent
3. β : Electric current effect coefficient

G. Lee, E.A. Olevsky, C. Manière, A. Maximenko, O. Izhvanov, C. Back, J. McKittrick, Effect of electric current on densification behavior of conductive ceramic powders consolidated by spark plasma sintering, *Acta Mater*., 144, 524-533 (2018)

Electric Current Effect on Densification during SPS

$$\dot{\theta} = -\left[\frac{G}{A_0 T} \left(\frac{b}{d} \right)^{p} \exp\left(\frac{-Q}{RT}\right) + \left[\int_{t_0}^{t_f} \frac{J^2 \lambda_d}{\tau_{PN}} dt \right]^{\omega} \right] \left(\frac{3\theta}{2}\right)^{\frac{m+1}{2m}} (1-\theta)^{\frac{m-3}{2m}} \left(\frac{\sigma_z}{G}\right)^{\frac{1}{m}}$$

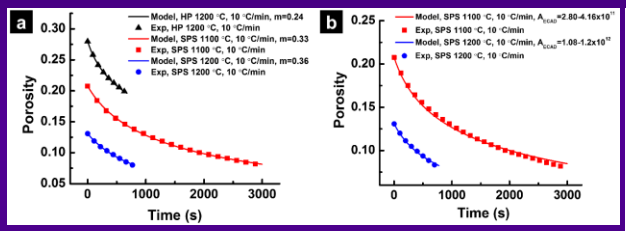

Experimental porosity evolution curves of ZrN specimens processed by HP or SPS fitted by the new constitutive equation

$\dot{\theta}$: Densification rate (1/s)
θ : Porosity
k : Boltzmann's constant (J/K),
D : Diffusion coefficient (cm2/s),
G : Shear modulus(MPa),
T : Absolute temperature (K),
b : Burgers vector (m),
σ_z : Z-axis applied stress (MPa),
Q : Activation energy (kJ/mol),
R : Gas constant
t_0, t_f : Starting and final time for SPS (s),
ω : Electric current sensitivity exponent,
τ_{PN} : Peiers-Nabarro stress (MPa),
J_{OL} : OLECD (A/m^2),
β : Electric current effect coefficient
d : Grain size (m),
p : Grain size exponent,
m : Strain rate sensitivity
λ : Electrical resistivity of defect free lattice
W: effective equivalent strain rate of porous material

Lee, Olevsky et al., Acta Mater., (2018)

Three Modes of Deconvolution: Different Current Density

- ω : Electric current sensitivity exponent,
- β : Electric current effect coefficient
- J: Electric current density (A/m^2)

- Different current density (J) → ω and β deconvolution

Insulation | Normal J | High J

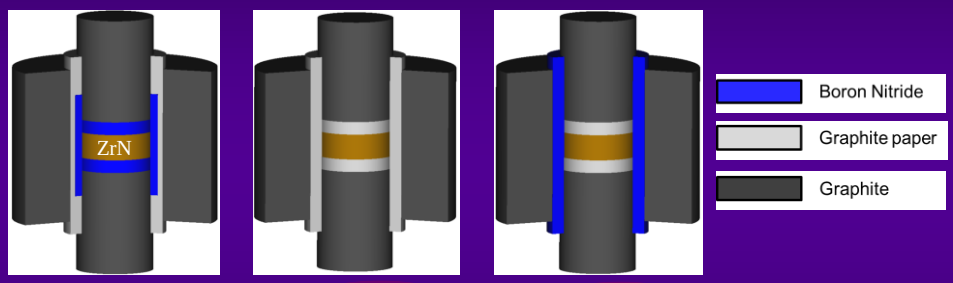

J = 0% | J = ~20~60% | J = 100%

1. Different current density but same T for all 3 modes: T directly measured by pyrometer
2. Boron nitride controls the flow of the electric current
3. Spark plasma sintering (SPS) used for all 3 modes: 100°C/min
4. Fine sized ZrN powders (2 µm)

Lee, Olevsky et al., Scripta Mater., 2019

79

79

Three Modes of Deconvolution: Local Current Density and Densification Behavior

First step: determination of local electric current density

Experimental: 1600°C, 60MPa, 100°C/min and 60min holding

1. FEM simulation

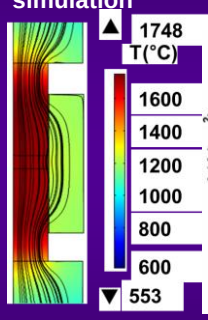

Normal J

2. local electric current density (JOL)

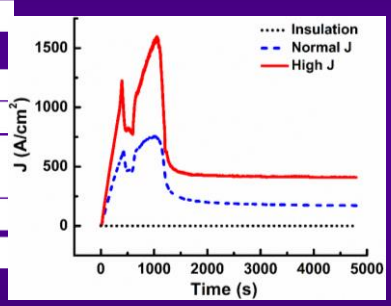

3. Porosity change at same temperature (1600 °C)

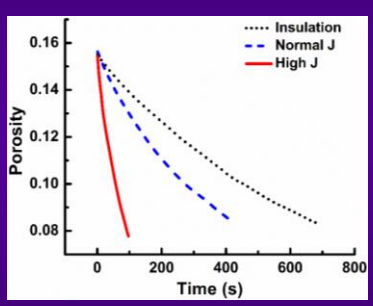

- **Electric current density : High J > Normal J > Insulation**
- **Densification rate : High J > Normal J > Insulation**

1. **Electric current facilitates the densification of ZrN**
2. **Different level of electric current density → Easy determination of electric current sensitivity exponent (ω)**

Lee et al., Sc
Lee, Olevsky et al., Scripta Mater., 2019

80

80

Three Modes of Deconvolution : Electric Current Density vs Dislocation Density

- **Higher J→ enhances dislocation movement → lower dislocation density ρ?**

A. Modified Williamson–Hall equation (MWH)

$$\Delta K \simeq 0.9/D + (\pi M^2 b^2/2)^{1/2} \rho^{1/2} K C^{1/2} + O(K^2 C)$$

B. MWH quadratic form

$$(\Delta K)^2 \simeq (0.9/D)^2 + (\pi M^2 b^2/2)\rho K^2 C \pm O(K^4 C^2)$$

- D: Average particle size (nm)
- b: magnitude of Burgers vector
- M: Constant depending on both the effective outer cut-off radius of dislocations and dislocation density
- ρ: Dislocation density (1/cm²)
- O: Higher order terms

$$\Delta K = 2\cos\theta(\Delta 2\theta)/\lambda \qquad K = \sin\theta/\lambda$$

- θ: Diffraction angle (rad)
- Δ2θ: Full width at half maximum (FWHM) (rad)
- λ: wavelength of X-rays (Cu Kα1 = 0.15406 nm)

$$\bar{C} = C_{h00}^{-}\left(1 - qH^2\right) \qquad H^2 = \frac{h^2l^2 + h^2k^2 + l^2k^2}{(h^2+k^2+l^2)^2}$$

- C: Average dislocation contrast factor
- Choo: Average dislocation contrast factor for h00 reflection (0.1353 for ZrN)
- q: Parameter depending on elastic constants of the crystal and the character of dislocations (-0.636 for ZrN)

Ungár et al., Appl. Phys. Lett., (1996)
Ungár et al., J. Appl. Cryst., (1999)
Holec et al., Phys. Rev. B., (2012)

XRD

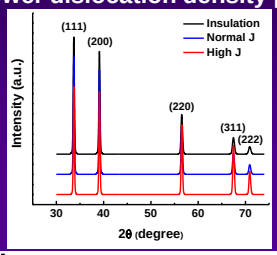

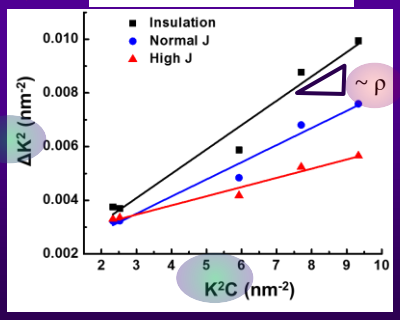

Lee, Olevsky et al., Scripta Mater., 2019

- Higher J renders lower dislocation density

Shape Impact on Relative Density Kinetics

Density evolution curves for -325 mesh alumina powder, sintered for 14 minutes at pressure 37 MPa in a cylindrical (A) and prismatic (B) die, at 1200, 1300 and 1400C.

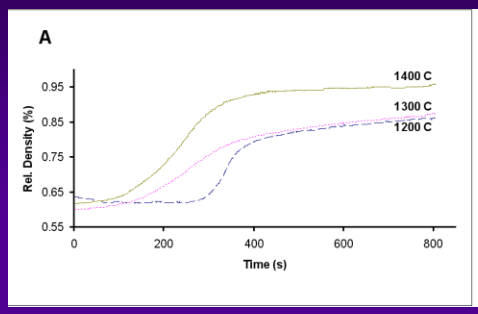

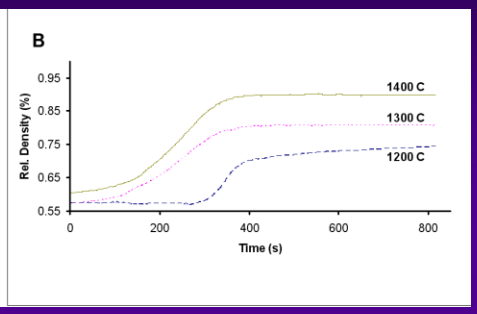

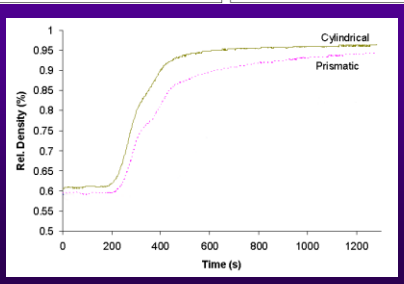

Density evolution for -325 mesh alumina powder in cylindrical and prismatic dies, sintered at 1300C for 20 minutes, with an applied pressure of 50 MPa.

SPS SCALABILITY (SIZE DEPENDENCE)

Alumina Disk-Shape Specimens (Same Aspect Ratio):
Alumina powder, -325 mesh, 99.99 % pure from Cerac Inc. (now Materion Advanced Chemicals Inc.) Initial average grain size: 0.38 µm

		15 mm	40 mm	48 mm	56 mm
Sample	Height [mm]	3	7.9	9.5	11.1
	Radius [mm]	7.5	20	24	28
Die	Height [mm]	30	80	96	111.4
	Radius [mm]	15	40	47.85	55.7
Punch	Height [mm]	15	40	47.8	56
Insert	Height [mm]	3.8	10	12	13.9
External Spacers	Height [mm]	8	20	20	20
	Radius [mm]	30	80	80	80
Transition	Height [mm]	30	80	95.7	111.4
	Radius 1 [mm]	7.5	20	23.9	27.85
	Radius 2 [mm]	30	80	95.7	111.4

experimental calibration

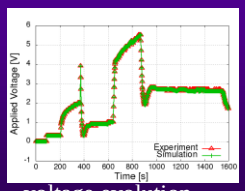

voltage evolution

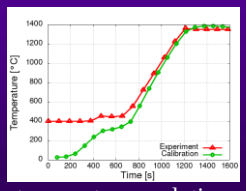

temperature evolution

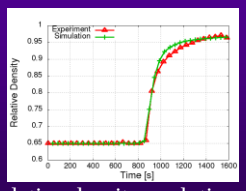

relative density evolution

E.A. Olevsky, W.L. Bradbury, C.D. Haines, D.G. Martin, and D. Kapoor, Fundamental Aspects of Spark Plasma Sintering: I. Experimental Analysis of Scalability, *J. Amer. Ceram. Soc.*, 95, 2406-2413 (2012)

SPS SCALABILITY (SIZE DEPENDENCE)

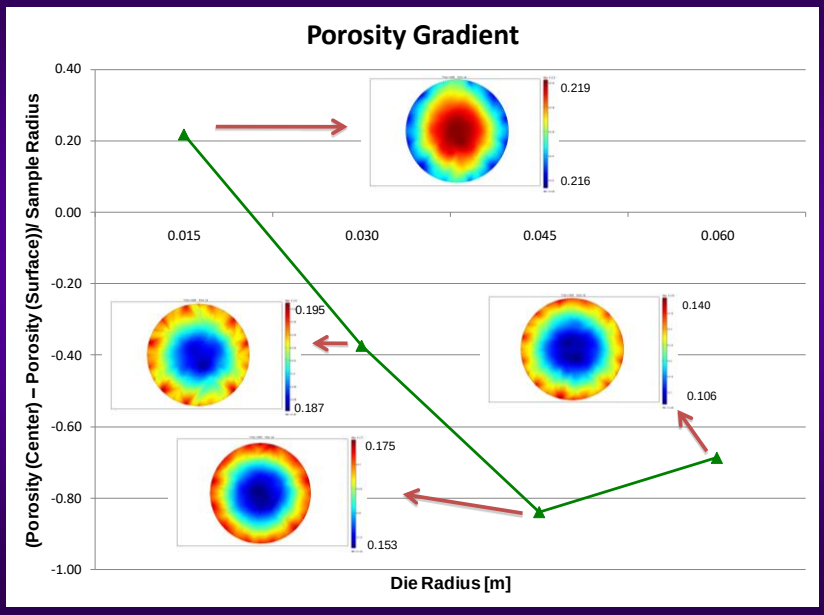

SPS SCALABILITY (SIZE DEPENDENCE)

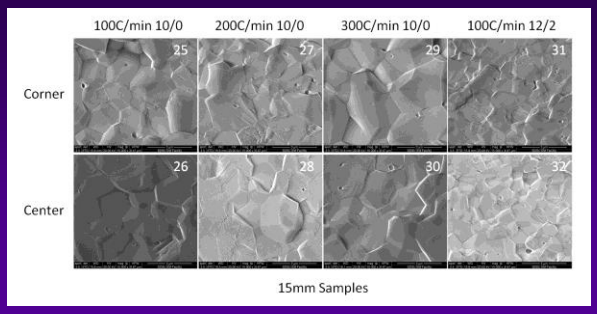

Alumina powder, -325 mesh, 99.99 % pure from Cerac Inc. (now Materion Advanced Chemicals Inc.) Initial average grain size: 0.38 µm

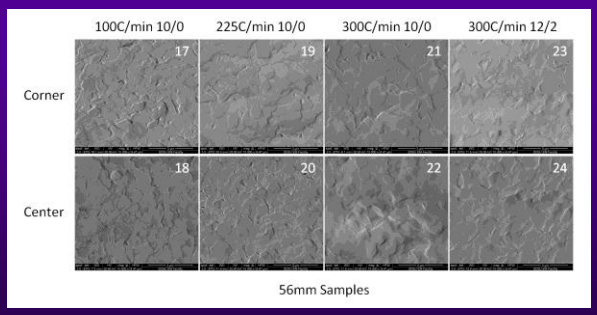

E.A. Olevsky, W.L. Bradbury, C.D. Haines, D.G. Martin, and D. Kapoor, Fundamental Aspects of Spark Plasma Sintering: I. Experimental Analysis of Scalability, *J. Amer. Ceram. Soc.*, 95, 2406-2413 (2012)

SPS SCALABILITY (SIZE DEPENDENCE)

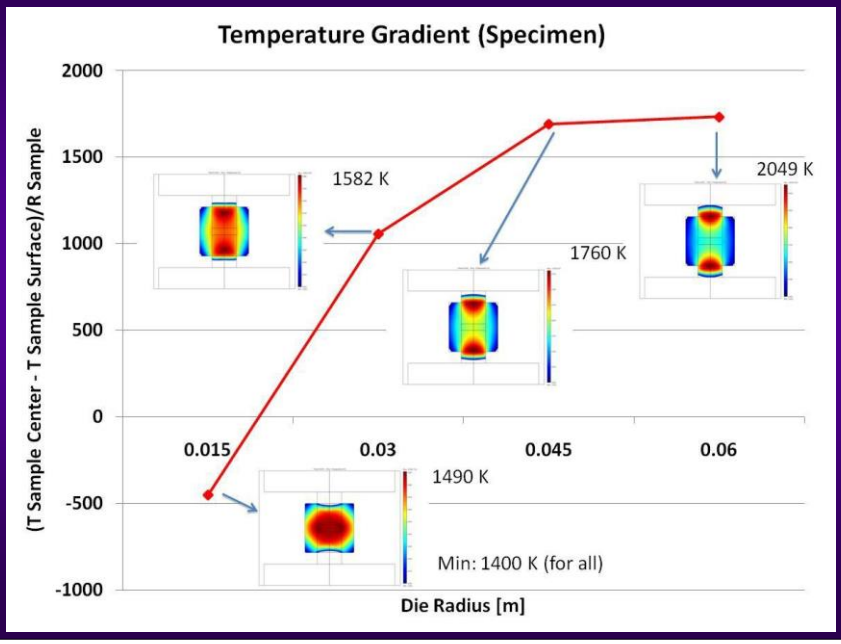

SPS SCALABILITY (SIZE DEPENDENCE): GRAIN GROWTH

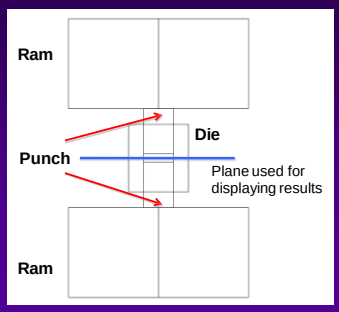

SPS Setup Geometry

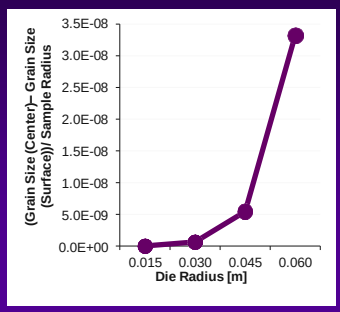

Grain Size Gradient

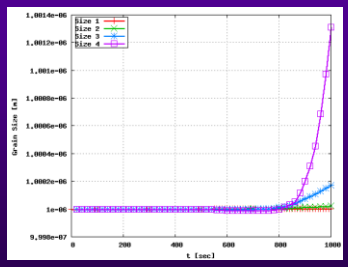

Grain Size Evolution at Sample Center

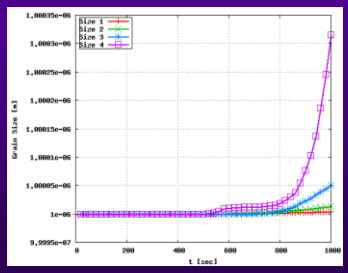

Grain Size Evolution at Sample Surface

Questions / Problems

1. The heating rate is within the thermal effects present in the Spark Plasma Sintering technology. Explain what effect this thermal effect has on the densification of the material.
2. After the SPS-forging of a porous cylindrical specimen, the final radius is 2.61 cm, the final height is 0.21 cm, the final porosity of 8%. Knowing that the initial porosity was 54%, what was the initial volume of this specimen?
3. How do parameters like porosity and grain size influence the contribution of different factors to the shrinkage rates of sintering materials subjected to spark plasma sintering?

TUTORIAL CONTENTS

- Sintering Fundamentals: Classic Concepts
- Sintering Fundamentals: Continuum Theory
- Introduction to Field-Assisted Sintering
- Spark-Plasma Sintering
- **High-Voltage Electric Discharge Compaction**
- Flash Sintering
- Microwave Sintering
- Integrated Additive Manufacturing – Field-Assisted Sintering
- Electric Nano-Pulse Technology

High Vs. Low Mode Field-Assisted Techniques

Field-Assisted Powder Consolidation

High-Voltage Techniques | Low-Voltage Techniques

High-Voltage Electric Discharge Compaction

< 300 µs	Up to 30kV	500 kA/cm²

Spark-Plasma Sintering

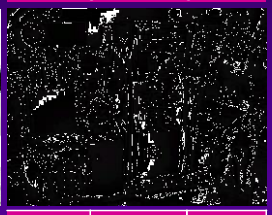

< 50kN	< 10V	< 1500 A

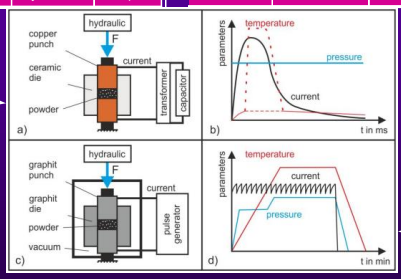

M.S. Yurlova, V.D. Demenyuk, D.V. Dudina, L.Yu. Lebedeva, E.G. Grigoryev, E.A. Olevsky, Review: Electric pulse consolidation: An alternative to spark plasma sintering, *J. Mater. Sci*. (2013) : http://dx.doi.org/10.1007/s10853-013-7805-8

Specifics of Processes under SPS and HVEDC

high voltage electric-pulse consolidation (e.g., HVEDC)

single, short, powerful pulses

low-voltage electric-pulse consolidation (e.g., SPS)

1st stage: low pressure lower pulse frequency

2nd stage: high pressure high power high frequency pulses

Electric Resistance of the Inter-Particle Contacts

The nonlinear contact electrical resistance of a powder compact depends on the properties of surface films on powder particles, on the externally applied pressure, and on the pulse current parameters.

There is a power law dependence of the conductivity of the investigated powders on the applied pressure.

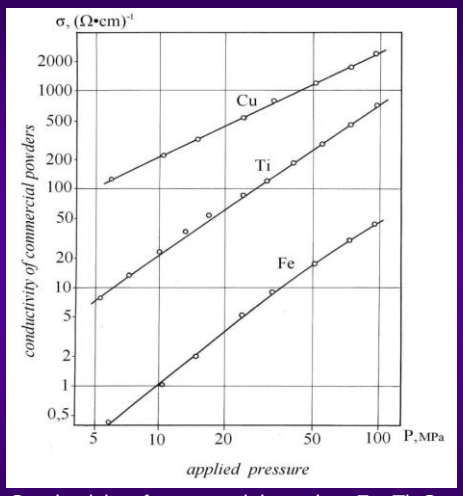

Conductivity of commercial powders Fe, Ti, Cu vs. applied pressure

E. G. Grigoryev and E. A. Olevsky, Thermal processes during high-voltage electric discharge consolidation of powder materials, *Scripta Mater*., 66, 662–665(2012)

Contact between Mo Particles under HVEDC Conditions

Spherical Mo powder particles (~ 150 μm), formed by the action of the constant compressive pressure of 80 MPa and of the heat sources of various intensity

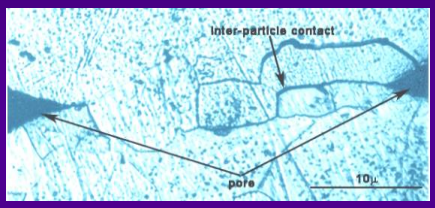

Plastic deformation of contact between the Mo particles

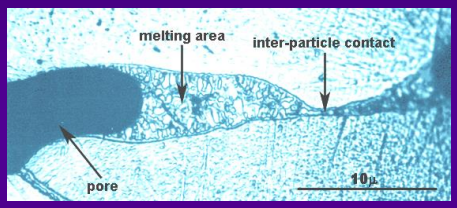

Melting of contact between Mo particles

- A more powerful heat source leads to the local melting of inter-particle contacts and to the high rate crystallization.
- If the power of a contact heat source exceeds the upper critical limit, it causes an electric thermal explosion of the inter-particle contact.

E. G. Grigoryev and E. A. Olevsky, Thermal processes during high-voltage electric discharge consolidation of powder materials, *Scripta Mater*., 66, 662–665(2012)

Mathematical Model of Physical Processes Occurring under HVEDC

$$\frac{\partial \rho}{\partial t} + div\,(\rho \vec{v}) = 0$$

$$\left(\frac{\partial \vec{v}}{\partial t} + (\vec{v}, \nabla)\vec{v}\right)_i = \left(\frac{\partial \sigma_{ik}}{\partial x_k}\right) + F_i$$

$$\frac{\partial}{\partial t}\rho\left(\varepsilon + \frac{\vec{v}^2}{2}\right) = -div\left(\rho\vec{v}\left(w + \frac{v^2}{2}\right) - (\vec{v}, \hat{\sigma}') - k\nabla T\right) + \frac{\vec{j}^2}{\sigma}$$

$$rot\,\vec{E} = -\frac{\partial \vec{B}}{\partial t},\ rot\,\vec{H} = \vec{j},\ \ div\,\vec{B} = 0$$

$$\vec{F} = [\vec{j}, \vec{B}], \quad \vec{j} = \sigma(\vec{E} + [\vec{v}, \vec{B}])$$

$\vec{v}$ – velocity, $\hat{\sigma}$ – internal stress tensor, ε – internal energy, w – enthalpy,
ρ – density, $\hat{\sigma'}$ – viscoplasticity tensor, T – temperature, $\vec{F}$ – Ampere force,
k – thermal conductivity, $\vec{j}$ – electrical current density,
σ – conductivity of the powder material, $\vec{B}$ – magnetic field induction,
$\vec{E}, \vec{H}$ – intensity of the electrical and magnetic fields, respectively

HVEDC: The Analysis of the Thermal Explosion (the Localization of Heat)

The time dependence of the electric current density in the inter-particle contact:

$$j(t) = j_0 \cdot \exp(-\beta t)\, \sin(\omega t)$$

j_0 – amplitude, ω – frequency and $1/\beta$ – duration of the pulse current, t – time

- The time of the energy injection into the powder is determined by the current pulse width: $t_0 < 10^{-3}$ s.
- The time t_1 of the formation of a consolidated material from the powder, depends on the loading system and is within the range of $2\times10^{-3} < t_1 < 2\times10^{-2}$ s.
- The cooling time of the consolidated material, t_2, is determined by the thermal conductivity of the materials and the characteristic size of the compacted sample: $t_2 \sim 2.5$ s.
- In this case, the time scales of the processes obey the following relationship:

$$t_0 < t_1 << t_2$$

E. G. Grigoryev and E. A. Olevsky, Thermal processes during high-voltage electric discharge consolidation of powder materials, *Scripta Mater*., 66, 662–665(2012)

HVEDC: Dimensionless Power of the Heat Source And Dimensionless Temperature in an Inter-particle Contact

Parameter	*Parameter description*
γ, c, χ, T_m	density, heat capacity, thermal diffusivity, melting temperature, respectively
ρ_0	specific contact resistance
R	characteristic size of the powder particles
$t_R = R^2/\chi$	characteristic time of heat diffusion in the particle
$\theta = T/T_m$	dimensionless temperature
$\tau = t/t_R$, $x = r/R$	dimensionless time, dimensionless coordinate, respectively
$\varepsilon = (\rho_0 j_0^2 t_R)/(\gamma c T_m)$	dimensionless power of heat source
$\Omega = \omega t_R$	dimensionless frequency of pulse current density
$\delta = 2\beta t_R$	dimensionless duration of pulse heat source
$f = \varepsilon e^{-\delta\tau} \sin^2(\Omega\tau)$	dimensionless instantaneous power of the heat source

Dimensionless parameters of thermal processes

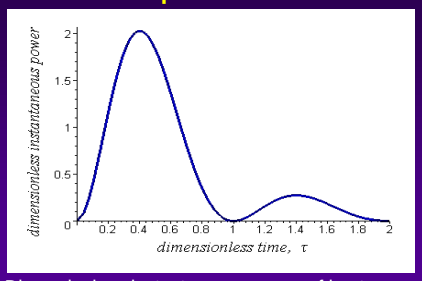

Dimensionless instantaneous power of heat source

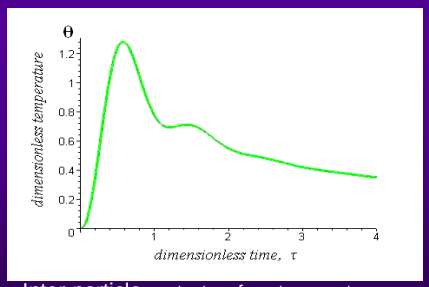

Inter-particle contact surface temperature vs. dimensionless time

E. G. Grigoryev and E. A. Olevsky, Thermal processes during high-voltage electric discharge consolidation of powder materials, *Scripta Mater*., 66, 662–665(2012)

HVEDC: Localization of the Spatial Temperature Distribution in the Contact Region

Parameter	Parameter description
γ, c, χ, T_m	density, heat capacity, thermal diffusivity, melting temperature, respectively
ρ_0	specific contact resistance
R	characteristic size of the powder particles
$t_R = R^2/\chi$	characteristic time of heat diffusion in the particle
$\theta = T/T_m$	dimensionless temperature
$\tau = t/t_R$, $x = r/R$	dimensionless time, dimensionless coordinate, respectively
$\varepsilon = (\rho_0 J_0^2 t_R)/(\gamma c T_m)$	dimensionless power of heat source
$\Omega = \omega t_R$	dimensionless frequency of pulse current density
$\delta = 2\beta t_R$	dimensionless duration of pulse heat source
$f = \varepsilon e^{-\delta\tau} \sin^2(\Omega\tau)$	dimensionless instantaneous power of the heat source

Dimensionless parameters of thermal processes

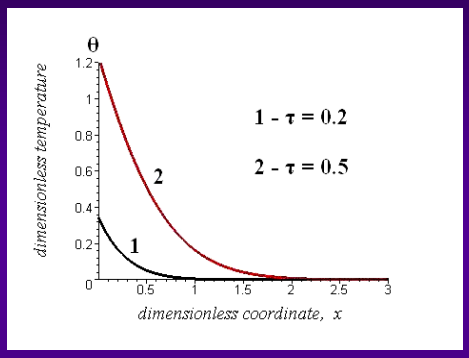

Instantaneous spatial temperature distributions

$\varepsilon = 5$; $\Omega = 3$; $\delta = 2$. These values of the dimensionless parameters correspond to the high-voltage pulse electric current sintering conditions, for which there is partial melting of the inter-particle contacts.

E. G. Grigoryev and E. A. Olevsky, Thermal processes during high-voltage electric discharge consolidation of powder materials, *Scripta Mater*., 66, 662–665(2012)

97

97

Experimental Vs. Calculation Data for the High Voltage Electric Discharge Consolidation of the Heat Resistant Steel (EP-741) Powder

Critical amplitude of the pulse current density, at which there is an electric thermal explosion of contact:

$$j_0 = \sqrt{\frac{2\xi\sigma}{\rho h} T_b^2}$$

$\xi \leq 1$
σ – the Stefan-Boltzmann constant
T_b – boiling point material
ρ – the electrical resistivity of contact spot
h – thickness of contact area

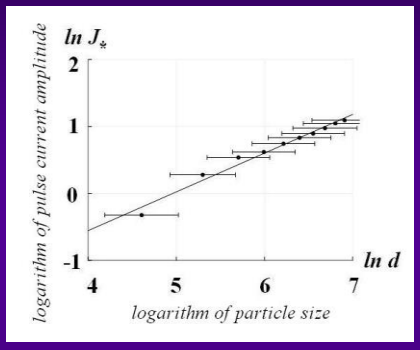

Experimental points and the theoretical prediction for the pulse current amplitude of the contact explosion ***J***$_*$ as a function of particle size ***d***

The calculation data is based on the thermal explosion criterion: $j_0 = \sqrt{\frac{2\xi\sigma}{\rho h} T_b^2}$

E. G. Grigoryev and E. A. Olevsky, Thermal processes during high-voltage electric discharge consolidation of powder materials, *Scripta Mater*., 66, 662–665(2012)

98

98

High-Voltage Electric Discharge Consolidation: Structure Inhomogeneity and Control

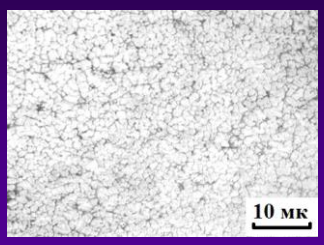

Steel P6M5,
J = 296 кА/см^2, P = 350 MPa

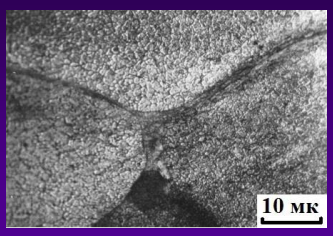

Steel P6M5,
J = 256 кА/см^2, P = 350 MPa

Specimen WC, axial cross-section:

Specimen WC, diameter 9мм
J = 90 кА/см^2, P = 200 MPa

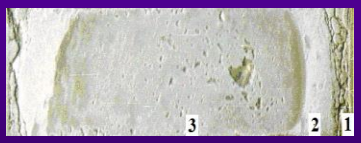

Specimen WC, diameter 9мм
J = 90 кА/см^2, P = 130 MPa

M.S. Yurlova, V.D. Demenyuk, D.V. Dudina, L.Yu. Lebedeva, E.G. Grigoryev, E.A. Olevsky, Review: Electric pulse consolidation: An alternative to spark plasma sintering, *J. Mater. Sci*. (2013) : http://dx.doi.org/10.1007/s10853-013-7805-8

High-Voltage Electric Discharge Consolidation: Manufacturing of Pressing Tools with High Wear Resistance

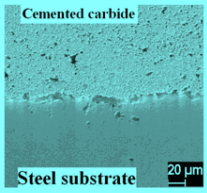

interface WC-Co / steel

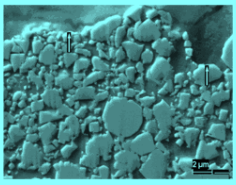

arrows indicate the contact surface

M.S. Yurlova, V.D. Demenyuk, D.V. Dudina, L.Yu. Lebedeva, E.G. Grigoryev, E.A. Olevsky, Review: Electric pulse consolidation: An alternative to spark plasma sintering, *J. Mater. Sci*. (2013) : http://dx.doi.org/10.1007/s10853-013-7805-8

Questions / Problems

1. Indicate and describe the phenomena that limit the scalability of high-voltage sintering technologies, such as high-voltage electric discharge compaction.
2. Describe the main processing parameters differences between SPS and HVEDC.

TUTORIAL CONTENTS

- Sintering Fundamentals: Classic Concepts
- Sintering Fundamentals: Continuum Theory
- Introduction to Field-Assisted Sintering
- Spark-Plasma Sintering
- High-Voltage Electric Discharge Compaction
- **Flash Sintering**
- Microwave Sintering
- Integrated Additive Manufacturing – Field-Assisted Sintering
- Electric Nano-Pulse Technology

Flash Sintering Experimentation

- Performed by Rishi Raj et.al.
- Yitria stabilized Zirconia powder
- Vertical Tube Furnace
- Dog bone specimen
- Pt Electrodes
- Shrinkage recorded via CCD camera

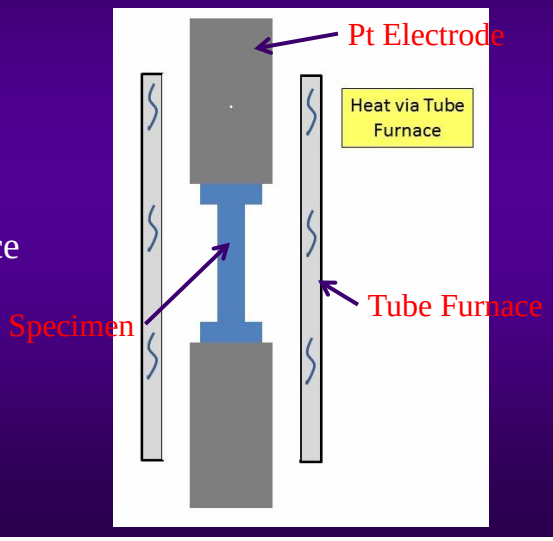

Flash Sintering Results

- Sintering rate depends on applied electric field
- Sintering rate becomes unstable ~40V/cm
- Small particle contacts necessary for flash sintering to occur

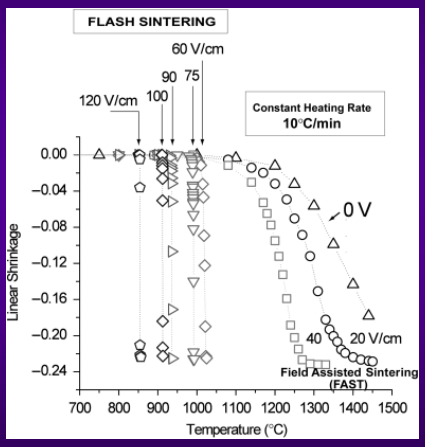

Source: *Flash Sintering of Nanograin Zirconia in o5 s at 850^{0}C*, Rishi Raj et. al., J. Am. Ceram. Soc., 93 [11] 3556–3559 (2010)

THERMAL RUNAWAY IN SIC CERAMICS

Electrical conductivity $\sigma(T)$ of SiC as a function of temperature T

$$\sigma(T) = eu_n \left\{ \frac{1}{2} N(1-\frac{1}{b}) + \left[\frac{1}{4} N^2 (1+\frac{1}{b})^2 + \left(\frac{\sigma_{i0}}{eu_n} \right)^2 \exp(-\frac{E}{kT}) \right]^{\frac{1}{2}} \right\}$$

where u_n is the mobility of free electrons $u_n = 52T^{-\frac{3}{2}}$; b is the electron-hole mobility ratio taken equal to 5; N is the concentration of impurities estimated according to[Racette] as $N \approx 10^{24}$; E is the SiC intrinsic conductivity activation energy which is taken in our calculations equal to 3.1eV; σ_{i0} is equal to $8 \cdot 10^5$; k is the Boltzmann constant.

Electrical conductivity as a function of porosity θ

$$\sigma_{eff} = \sigma(T) \frac{2(1-\alpha\theta)}{2+\theta}$$

E.A. Olevsky, S.M. Rolfing, A.L. Maximenko, Flash (ultra-rapid) spark-plasma sintering of silicon carbide, *Nature Sci. Rep.*, 6, 33408 (2016)

105

105

THERMAL RUNAWAY IN SIC CERAMICS

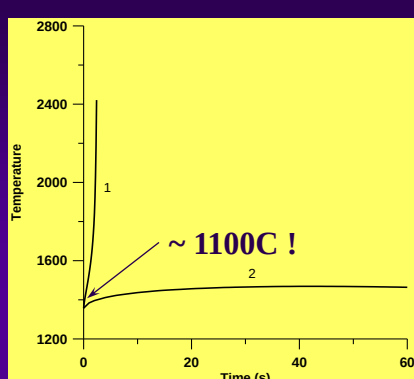

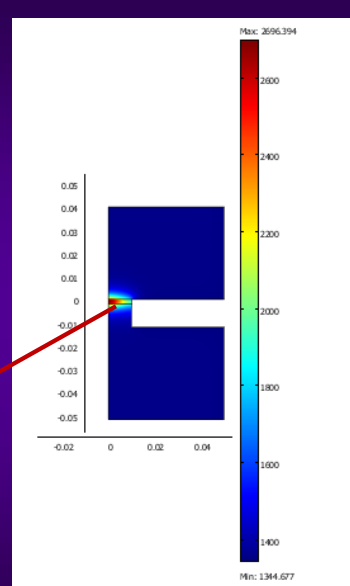

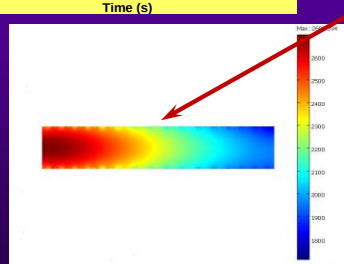

E.A. Olevsky, S.M. Rolfing, A.L. Maximenko, Flash (ultra-rapid) spark-plasma sintering of silicon carbide, *Nature Sci. Rep.*, 6, 33408 (2016)

106

106

FLASH SPS DIE OPERATION

- Uses Copper Tube
- Current through Copper
- Copper Tube Melts
- Punch Contacts Specimen
- Current through Specimen
- Densification of Specimen

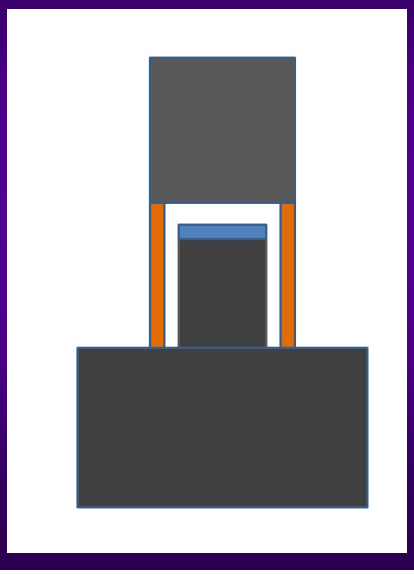

E.A. Olevsky, S.M. Rolfing, A.L. Maximenko, Flash (ultra-rapid) spark-plasma sintering of silicon carbide, *Nature Sci. Rep.*, 6, 33408 (2016)

FLASH SPS DIE

- The “switch” is a sacrificial conductor that carries the current load at the start of the experiment, current is then forced through the specimen.
- Geometry and alloy of conductive tube can be changed to control the temperature at which the current is passed through the specimen.

EXPERIMENTAL PROCEDURE

- Pre-Consolidate SiC Sample using SPS
  - Low starting density ~75%
- Flash SPS
- Measure Density
  - Utilizing Archimedes principle
- Characterize with scanning electron microscope
  - Gauge densification
  - Examine grain structure

Initial powder: 99.99% pure SiC
Cerac Inc., 1 μm average size
SiC(6H)

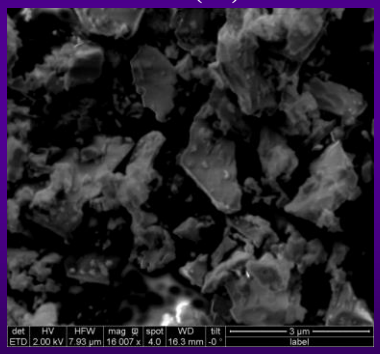

E.A. Olevsky, S.M. Rolfing, A.L. Maximenko, Flash (ultra-rapid) spark-plasma sintering of silicon carbide, *Nature Sci. Rep.*, 6, 33408 (2016)

PRE-SINTER SIC SPECIMEN

- SPS process used
- 10mm x 2mm specimen
- Target density is 75%
- Specimen heated to 1650^0C
- Used in all experiments

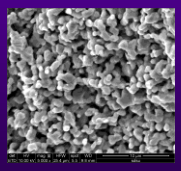

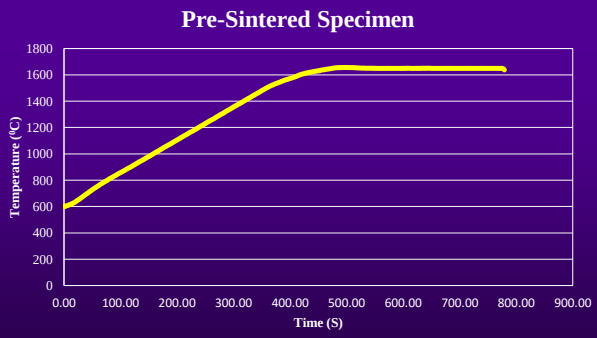

E.A. Olevsky, S.M. Rolfing, A.L. Maximenko, Flash (ultra-rapid) spark-plasma sintering of silicon carbide, *Nature Sci. Rep.*, 6, 33408 (2016)

HIGH TEMPERATURE SIC SPS

- Temperature of 2100°C
- Grain Growth, limited densification

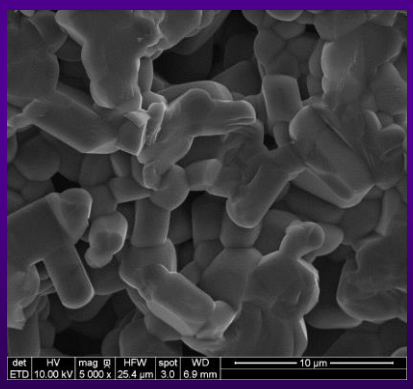

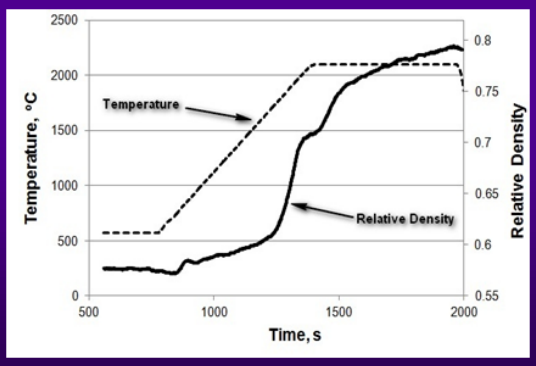

E.A. Olevsky, S.M. Rolfing, A.L. Maximenko, Flash (ultra-rapid) spark-plasma sintering of silicon carbide, *Nature Sci. Rep.*, 6, 33408 (2016)

HIGH TEMPERATURE SINTERING OF SIC

- 10 °C/min, maximum temperature 2500 °C, holding 25 min, cooling 30 °C/min.
- Grain Growth, limited densification

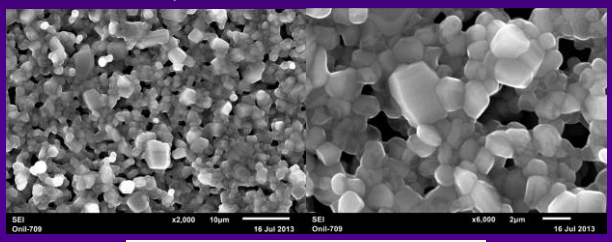

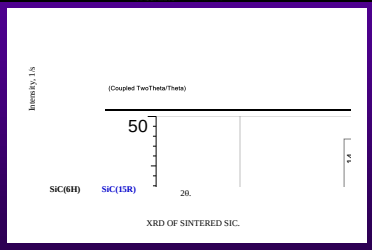

E.A. Olevsky, S.M. Rolfing, A.L. Maximenko, Flash (ultra-rapid) spark-plasma sintering of silicon carbide, *Nature Sci. Rep.*, 6, 33408 (2016)

FLASH SPS

E.A. Olevsky, S.M. Rolfing, A.L. Maximenko, Flash (ultra-rapid) spark-plasma sintering of silicon carbide, *Nature Sci. Rep.*, 6, 33408 (2016)

FLASH SPS RESULTS

- Copper tube melts and deforms

Before Flash Sintering

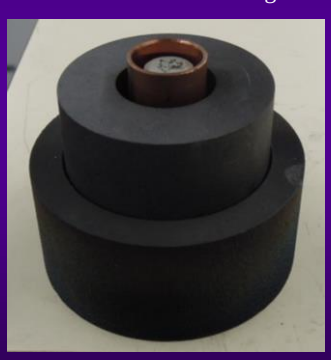

After Flash Sintering

E.A. Olevsky, S.M. Rolfing, A.L. Maximenko, Flash (ultra-rapid) spark-plasma sintering of silicon carbide, *Nature Sci. Rep.*, 6, 33408 (2016)

FLASH SPS RESULTS

Short copper tube

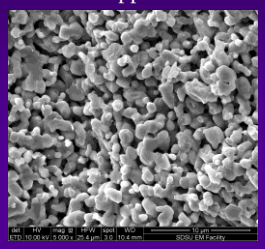

- Limited densification
- No Grain growth
- Intra-particle contacts formed, but not developed strongly
- Porosity remains high
- Not much different from Pre-Sintered Specimen

Medium copper tube

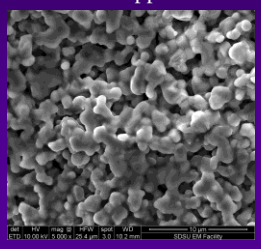

- Pre-heat specimen for a longer time
- Strongly developed intra-particle contacts
- Better Densification

Longer copper tube

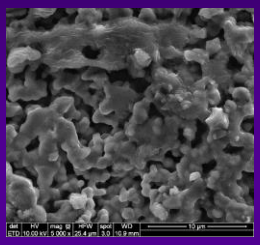

- Very strong intra-particle contact
- Moderate Grain Growth
- Even better densification

E.A. Olevsky, S.M. Rolfing, A.L. Maximenko, Flash (ultra-rapid) spark-plasma sintering of silicon carbide, *Nature Sci. Rep.*, 6, 33408 (2016)

FLASH SPS: PRESSURE INFLUENCE

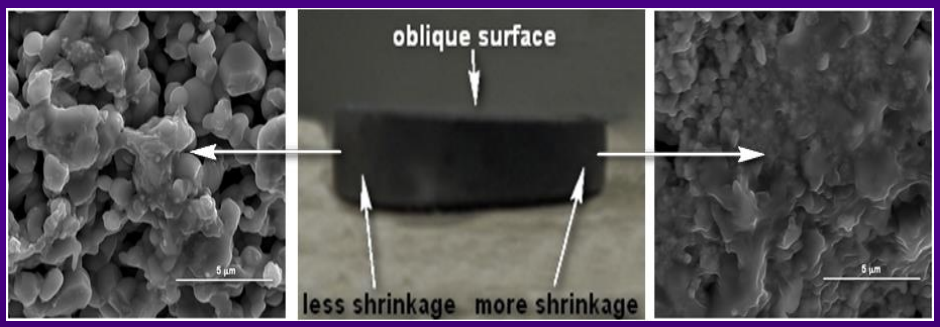

E.A. Olevsky, S.M. Rolfing, A.L. Maximenko, Flash (ultra-rapid) spark-plasma sintering of silicon carbide, *Nature Sci. Rep.*, 6, 33408 (2016)

FLASH SPS RESULTS

- Limited Grain growth
- Excellent Densification

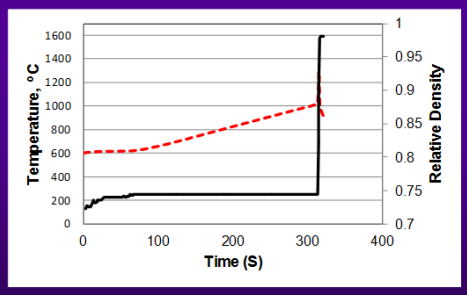

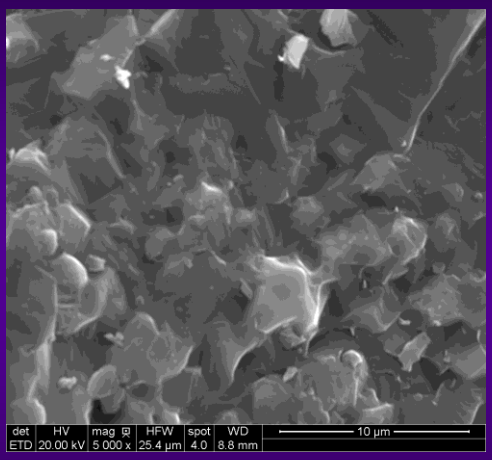

E.A. Olevsky, S.M. Rolfing, A.L. Maximenko, Flash (ultra-rapid) spark-plasma sintering of silicon carbide, *Nature Sci. Rep.*, 6, 33408 (2016)

Net shape flash spark plasma sintering configuration

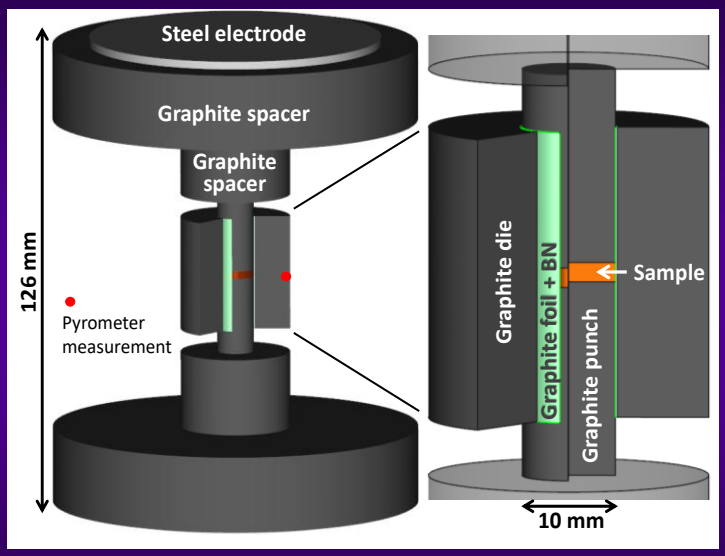

The lateral graphite foil is coated with a boron nitride spray to electrically insulate the die and concentrate the electric current on the sample.

Net shape flash spark plasma sintering configuration

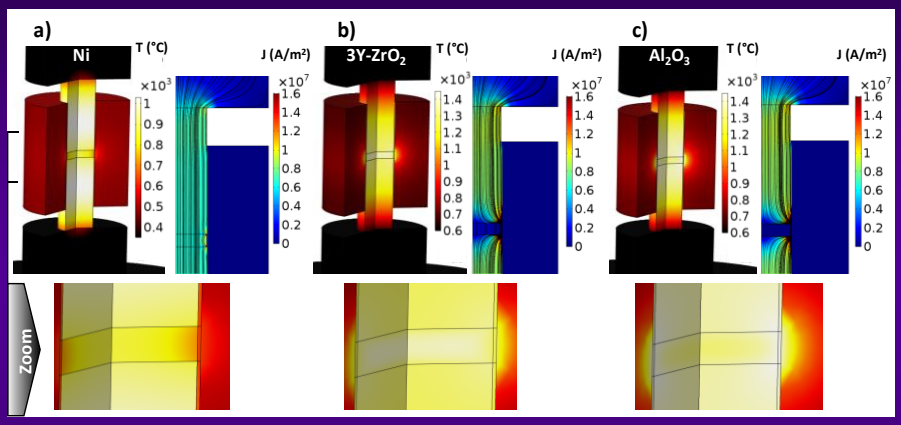

Simulated temperature, electric current density field, and electric current for nickel, zirconia, and alumina samples

Net shape flash spark plasma sintering configuration

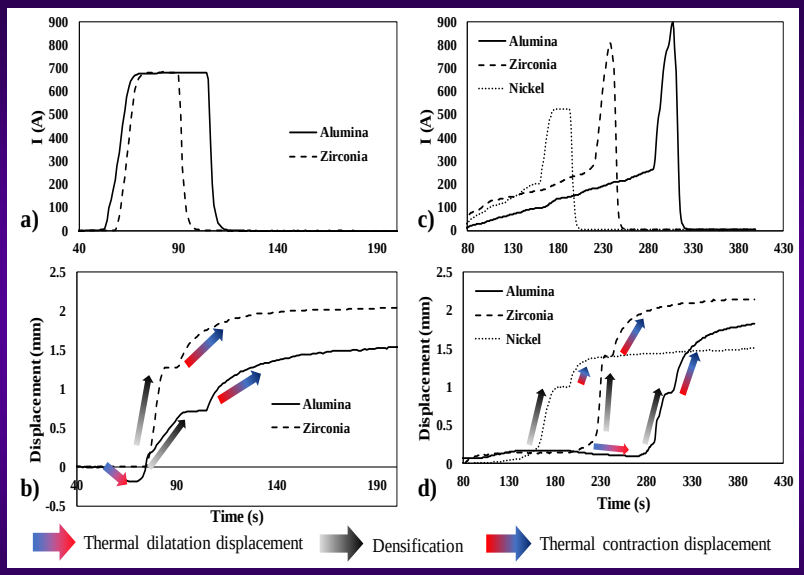

Experimental electric current (a,c) and displacement (b,d) curves under constant current mode (a,b) and forced mode (c,d)

Net shape flash spark plasma sintering configuration

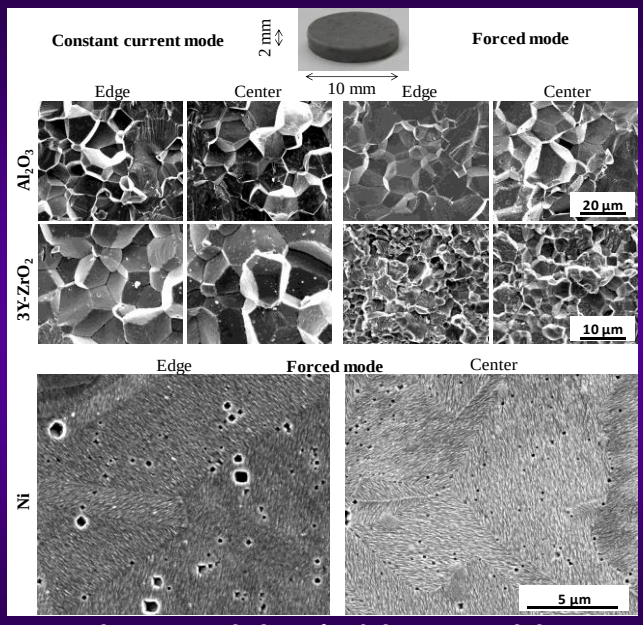

SEM images in the centers and edges of nickel, zirconia and alumina samples for constant and forced current modes

12

121

121

Questions / Problems

1. Describe the flash sintering process and physical phenomena that induce it.
2. What thermal and non-thermal phenomena may contribute to mass transfer under flash sintering conditions?

122

122

TUTORIAL CONTENTS

Ponderomotive Forces in Microwave Sintering

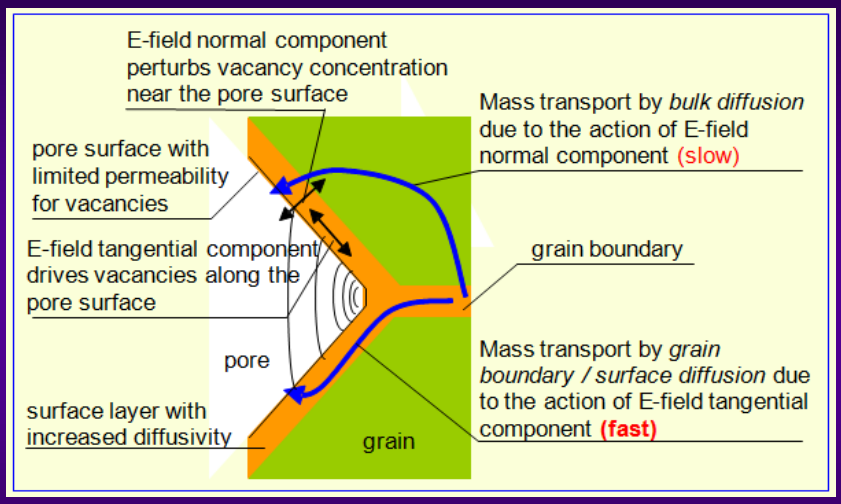

- K. I. Rybakov, E. A. Olevsky, E. V. Krikun, Microwave Sintering: Fundamentals and Modeling, *J. Am. Ceram. Soc.*, 96, 1003–1020 (2013)
- E.A. Olevsky, A.L. Maximenko, and E.G. Grigoryev, Ponderomotive effects during contact formation in microwave sintering, *Modelling Simul. Mater. Sci. Eng.*, 21, 055022 (2013)
- K. Rybakov, E. Olevsky, and V. Semenov, Microwave ponderomotive effect on ceramics sintering, *Scripta Mater.*, 66, 1049-1052 (2012)

Ponderomotive Forces in Microwave Sintering

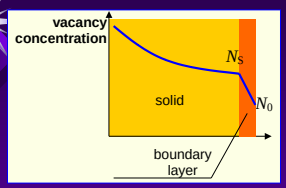

$$\langle N_{\pm}\mathbf{E}\rangle \neq 0\ !$$

The model of ponderomotive action of microwave field starts from the observation that mobile vacancies in ionic crystalline solids carry effective electric charges. When an electric field, **E**, is applied, vacancies participate in drift motion, and the overall flux of each sort of vacancies, **J**, consists of the diffusion and drift parts:

$$\mathbf{J} = -D^{(v)}\nabla C_v + D^{(v)}C_v\frac{q\mathbf{E}}{kT},$$

where C_v is concentration, $D^{(v)}$ is diffusivity, and q is effective electric charge of vacancies. For the typical conditions of microwave sintering, the amplitude of the drift part of the flux exceeds the diffusion part by 2–3 orders of magnitude. However, the drift flux is oscillating at the microwave frequency, and needs to be "rectified" in order to influence the relatively slow mass transport phenomena. Such non-linear rectification can be caused by the perturbations of vacancy flow near pore surfaces that have limited permeability for vacancies. The concentration of vacancies builds up in a thin layer near the surface when the electric field drives them toward the surface and/or depletes during the next half-period when the field changes its direction and drives them from the surface into the bulk. The thickness of the layer in which the vacancy concentration is perturbed by the electric field is the smaller of the Debye-Huckel radius $\lambda = \sqrt{\varepsilon'\Omega kT/8\pi q^2 C_{v0}}$ (where ε' is lattice dielectric constant of the material, Ω is the vacancy volume and C_{v0} is equilibrium vacancy concentration normalized on the overall number of sites in the crystalline lattice) and the characteristic diffusion width $l = \sqrt{D^{(v)}/\omega}$ (where ω is the microwave field cyclic frequency).

Vacancy Flux:

$$\langle \mathbf{J}\rangle \cong -D\nabla\langle N\rangle + \frac{D\Omega}{kT}\langle \rho\mathbf{E}\rangle$$

Average ponderomotive force

❖ K. Rybakov, E. Olevsky, and V. Semenov, Microwave ponderomotive effect on ceramics sintering, *Scripta Mater.*, 66, 1049-1052 (2012)

Ponderomotive Forces in Microwave Sintering

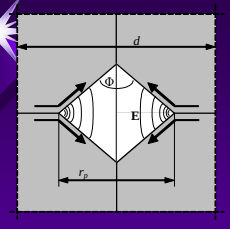

The vacancy flux $\frac{dA}{dt} = -\frac{1}{2}\left|\int J dl\right| \cdot \frac{D_{gb}}{D_S}\cdot\frac{r_p}{d}$, where D_{gb} is the coefficient of grain boundary diffusion, D_S is the coefficient of surface diffusion, r_p is the pore width and d is the grain size. The multiplier D_{gb}/D_S reflects the fact that the pore closure process is limited by the grain boundary rather than surface diffusion, and the factor $\frac{1}{2}\cdot\frac{r_p}{d}$ arises due to diffusion redistribution of vacancies over the pore surface and intergrain boundaries.

$$\frac{dA}{dt} = -D_{gb}\frac{\varepsilon_0\Omega}{2C_{v0}kT}\frac{r_p}{d}\overline{\langle E_n E_\tau\rangle}$$

The obtained results make it possible to describe the evolution of porosity, Θ, defined as the ratio of pore volume to the total volume of the porous body. It is linked with the rate of deformation $\dot{e}$, i.e. change in volume

$$\frac{1}{1-\Theta}\frac{d\Theta}{dt} = \dot{e} = \frac{1}{A}\frac{dA}{dt}$$

The ratio of the characteristic times of densification due to microwave ponderomotive effect and conventional free sintering is

$$\frac{\tau_{MW}}{\tau_{FS}} \cong \frac{C_{v0}\alpha\delta_{gb}}{d^2\varepsilon_0 E_{int}^{\ 2}}$$

For $C_{v0}=10^{-5}$, $\alpha = 1$ J/m^2, $\delta_{gb} = 10^{-9}$ m, $d = 10^{-6}$ m, $\varepsilon_0 = 8.85\cdot 10^{-12}$ F/m and $E_{int} = 3\cdot 10^4$ V/m we obtain $\tau_{MW}/\tau_{FS} \sim 1$, i.e. the characteristic times are within the same order of magnitude. This means that under these conditions the contribution of the microwave ponderomotive effect into sintering is significant.

Ponderomotive Forces in Microwave Sintering

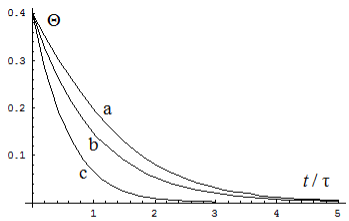

Evolution of porosity during sintering due to microwave ponderomotive effect (a), capillary stresses (b), and their combined effect (c). Initial porosity $\Theta_0 = 0.4$.

In the course of sintering, the pore surfaces will tend to smoothen due to surface diffusion, and the pore shape will change from faceted to ellipsoidal. The electric field will still be enhanced in this configuration, but not to infinite strength. Therefore, the resulting ponderomotive contribution into densification will be most pronounced at the initial stages of sintering and decrease towards the end of the sintering process. This is in agreement with most comparative studies of microwave vs. conventional sintering, which report the most drastic difference in kinetics at the first stages of densification. Yet, it should also be noted that the ponderomotive effects can be relevant in microwave sintering of nanocrystalline materials in which pore surfaces tend to retain faceted shape reflecting the material's crystalline structure

Bloomden microwave cavity

- Small monomodal cavity 2.45 GHz (easy to simulate)
- Hybrid heating with SiC suceptor
- Pyrometer T measure
- Argon atmosphere

Inner cavity

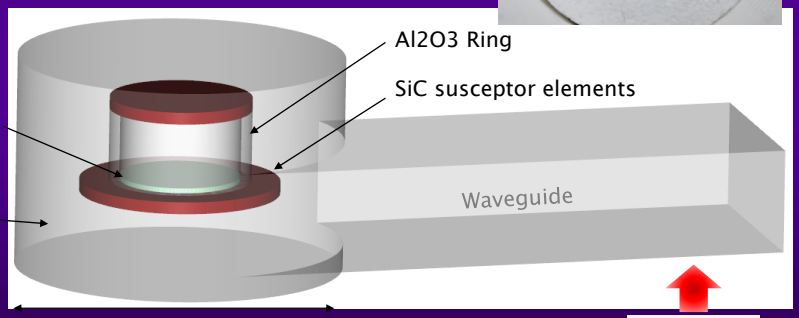

Hybrid heating of Ti-6Al-4V

Heating possible up to 700°C, then spark phenomena happen

Spark → Microwave turn off

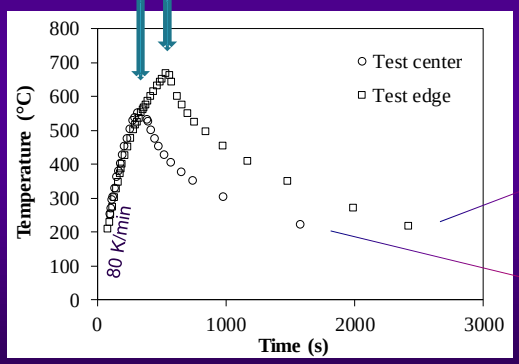

Before

After

C. Manière, G. Lee, T. Zahrah, E. A. Olevsky, Microwave flash sintering of metal powders: from experimental evidence to multiphysics simulation, *Acta Mater*. (2018) – *accepted*.

Ti heating surrounded by SiC powder

Extremely fast heating of the Ti-6Al-4V sample revealed

Ti sample melting!

Alumina container broken

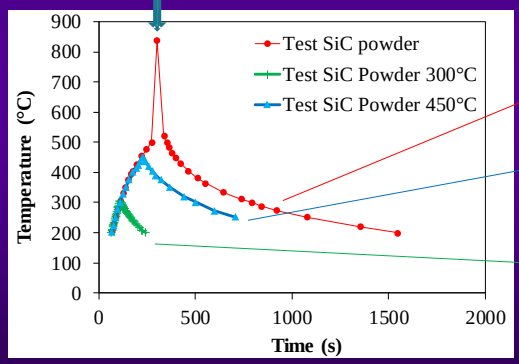

Before

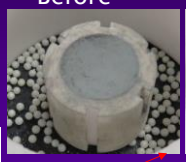

After

80% dense

C. Manière, G. Lee, T. Zahrah, E. A. Olevsky, Microwave flash sintering of metal powders: from experimental evidence to multiphysics simulation, *Acta Mater*. (2018) – *accepted*.

Microwave/conventional microstructure

Microwave sintering
→ Fast < 2 min
→ Inhomogeneous
→ 50–80% dense

Conventional sintering
→ Long ~ 10 h
→ Homogeneous

Powder

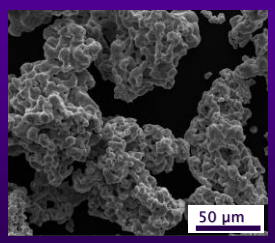

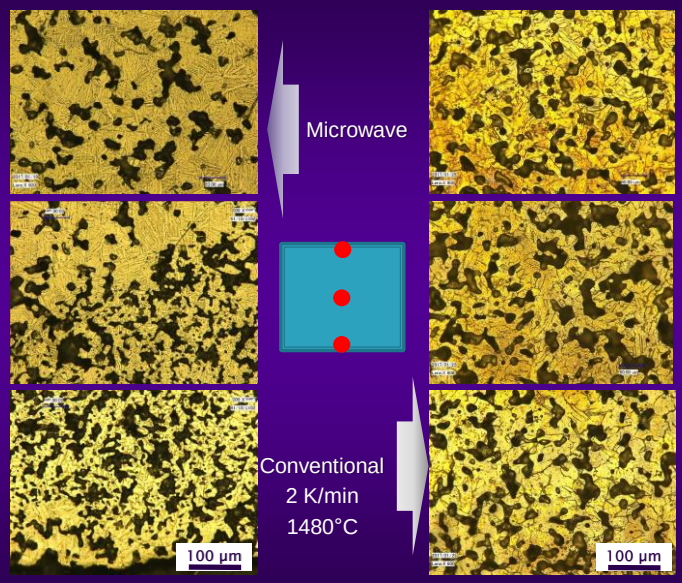

C. Manière, G. Lee, T. Zahrah, E. A. Olevsky, Microwave flash sintering of metal powders: from experimental evidence to multiphysics simulation, *Acta Mater*. (2018) – *accepted*.

Electromagnetic Thermal Mechanical Model

Microwave heating

Maxwell's equations combined in:

$$\nabla\times(\mu_r^{-1}\,\nabla\times\boldsymbol{E_r}) = k_0^2\left(\varepsilon_r - \frac{j\sigma}{\omega\,\varepsilon_0}\right)\boldsymbol{E_r}$$

Heat equation:

$$\rho C_p\frac{\partial T}{\partial t} + \nabla.(-\kappa\nabla T) = Q_e$$

Microwave power loss density $Q_e = \frac{1}{2}(\varepsilon_0\varepsilon_r''\boldsymbol{E}^2 + \mu_0\mu_r''\boldsymbol{H}^2)$

C. Manière, T. Zahrah, E.A. Olevsky, Fully coupled electromagnetic-thermal-mechanical comparative simulation of direct vs hybrid microwave sintering of 3Y-ZrO2, *J. Am. Ceram. Soc.*, 100, 2439-2450 (2017)

Continuum theory of sintering

Stress tensor

$$\underline{\sigma} = \frac{\sigma_{eq}}{\dot{\varepsilon}_{eq}}\left(\varphi\underline{\dot{\varepsilon}} + \left(\psi - \frac{1}{3}\varphi\right)tr(\underline{\dot{\varepsilon}})\mathbb{1}\right) + P\mathbb{1}$$

Equivalent strain rate

$$\dot{\varepsilon}_{eq} = \frac{1}{\sqrt{1-\theta}}\sqrt{\varphi\dot{\gamma}^2 + \psi\dot{e}^2}$$

Functions of the porosity θ: $\psi = \frac{2}{3}\frac{(1-\theta)^3}{\theta}$ $\varphi = (1-\theta)^2$

Dense creep behavior $\sigma_{eq} = K(T,G)\dot{\varepsilon}_{eq}{}^m$ for linear viscous materials $\sigma_{eq} = 2\eta_0\dot{\varepsilon}_{eq}$

R.K. Bordia, S.J.L. Kang, E.A. Olevsky, Feature Article: Current understanding and future research directions at the onset of the next century of sintering science and technology, *J. Amer. Ceram. Soc.*, 100, 2314-2352 (2017)

Direct MW heating of 3Y-ZrO2

EMTM fully coupled model

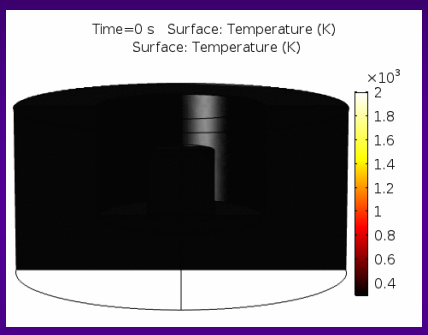

Relative density

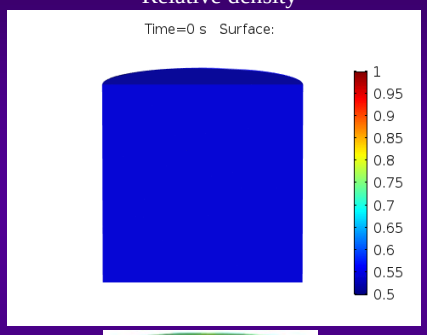

T grad → Non cylindrical final shape:

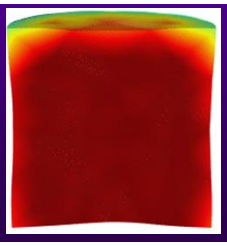

C. Manière, T. Zahrah, E.A. Olevsky, Fully coupled electromagnetic-thermal-mechanical comparative simulation of direct vs hybrid microwave sintering of 3Y-ZrO2, *J. Am. Ceram. Soc.*, 100, 2439-2450 (2017)

Ceramic/metal microwave heating

- Non magnetic ceramics are sensible to E
  - Lots of ceramics have a runaway of their conductivity then of ε''_{eff}
  - Low dissipation at room T and high dissipation at high T
- Metal powders are sensible to the alternative H field
  - μ''_{eff} decreases with T and have no runaway
  - The metal powder heating is moderate and without runaway

$$Q_e = \frac{1}{2}(\varepsilon_0 \varepsilon''_r \boldsymbol{E}^2 + \mu_0 \mu''_r \boldsymbol{H}^2)$$

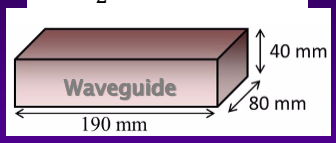

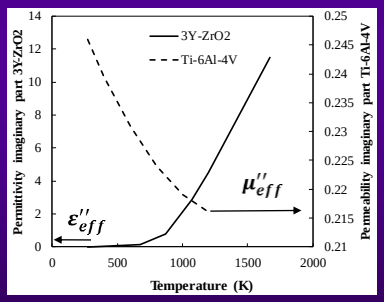

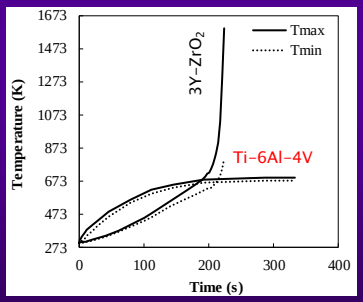

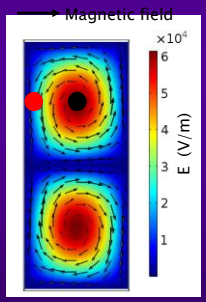

C. Maniere, C. Zahrah, T. Olevsky, E.A. Scripta Materialia 128 (2017) 49-52

Ceramic/metal microwave heating

- Non magnetic ceramics are sensible to E
  - Lots of ceramics have a runaway of their conductivity then of ε''_{eff}
  - Low dissipation at room T and high dissipation at high T
- Metal powders are sensible to the alternative H field
  - μ''_{eff} decreases with T and have no runaway
  - The metal powder heating is moderate and without runaway

$$Q_e = \frac{1}{2}(\varepsilon_0 \varepsilon''_r \boldsymbol{E}^2 + \mu_0 \mu''_r \boldsymbol{H}^2)$$

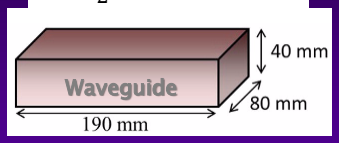

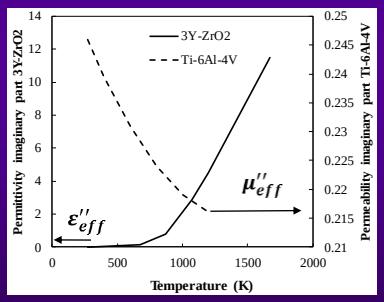

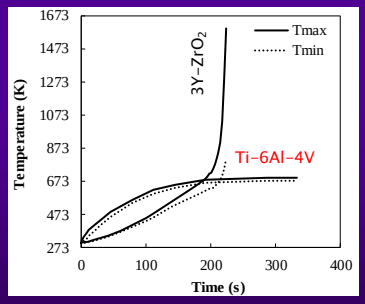

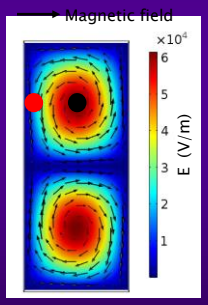

Maniere, C. Zahrah, T. Olevsky, E.A. Scripta Materialia 128 (2017) 49–52
San Diego State University (USA)

135

135

Questions / Problems

1. What distinguishes microwave sintering heating from conventional furnace heating?
2. Explain the nature of ponderomotive forces in microwave sintering.
3. Indicate and describe the field effects present in the Spark Plasma Sintering, Microwave Sintering and High Voltage Electric Discharge Compaction.

136

136

TUTORIAL CONTENTS

- Sintering Fundamentals: Classic Concepts
- Sintering Fundamentals: Continuum Theory
- Introduction to Field-Assisted Sintering
- Spark-Plasma Sintering
- High-Voltage Electric Discharge Compaction
- Flash Sintering
- Microwave Sintering
- **Integrated Additive Manufacturing – Field-Assisted Sintering**
- Electric Nano-Pulse Technology

Sintering-Assisted Additive Manufacturing

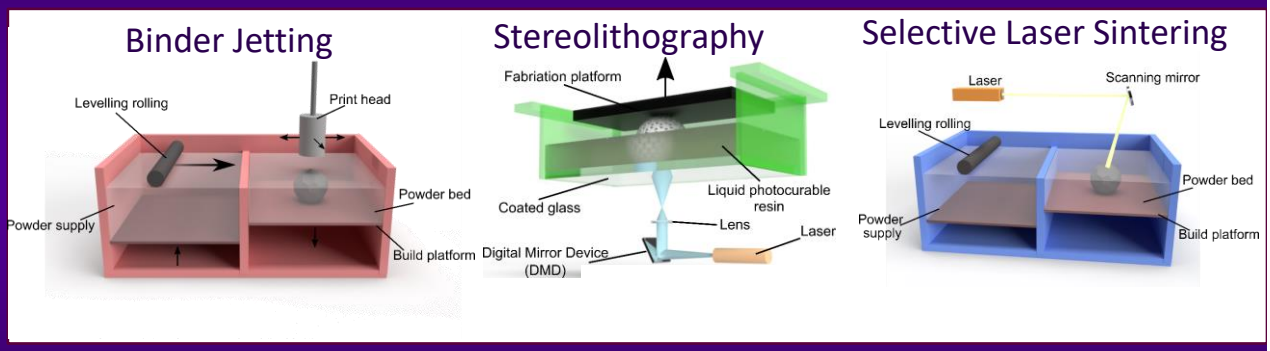

G. Lee, M. Carrillo, J. McKittrick, D.G. Martin, E.A. Olevsky, Fabrication of ceramic bone scaffolds by solvent jetting 3D printing and sintering: Towards load-bearing applications, Additive Manufacturing 33, 101107 (2020)

Sintering-Assisted Additive Manufacturing

Binder Jetting

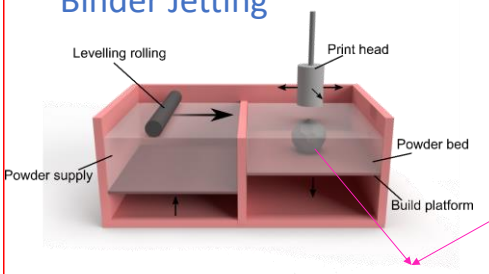

Stereolithography

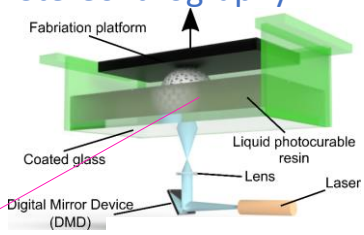

Selective Laser Sintering

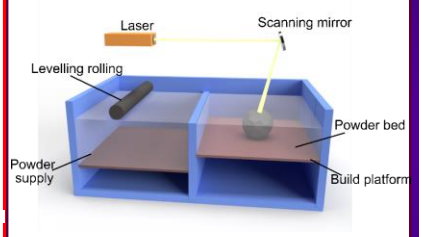

Green component

Debinding

Sintering

Final Component

Sintering Model

Free Sintering –Solid State

Olevsky model is utilized as the basis for our theoretical analysis:
E. Olevsky, Theory of sintering: From discrete to continuum, Mater. Sci. Eng. Rep., 1998

$$\sigma(W) = 2\eta_0 W$$

$$P_L = \frac{3\alpha}{r_0}(1-\theta)^2$$

$$\sigma_{ij} = \frac{\sigma(W)}{W}\left[\varphi\dot{\varepsilon}_{ij} + \left(\psi - \frac{1}{3}\varphi\right)\dot{e}\delta_{ij}\right] + P_L\delta_{ij}$$

$$\varphi = (1-\theta)^2 \qquad \psi = \frac{2}{3}\frac{(1-\theta)^3}{\theta}$$

σ_{ij} : external applied stress
$\sigma(W)$: effective stress model
W: effective strain rate
$\dot{\varepsilon}_{ij}$: total strain rate
φ: normalized shear modulus
ψ: normalized bulk modulus
$\dot{e}$: volume strain rate
δ_{ij} : Kronecker delta
P_L: sintering stress
θ: porosity
η_0 : viscosity bulk material

Sintering Model

Liquid Phase Sintering

Model needs to consider:

- presence of liquid and solid phases
- effect of gravity that induces settlement of solid particles

$$\sigma(W) = 2\eta_0 W$$

$$P_L = \frac{3\alpha}{r_0}(1-\theta)^2$$

$$\sigma_{ij} = \frac{\sigma(W)}{W}\left[\varphi\dot{\varepsilon}_{ij} + \left(\psi - \frac{1}{3}\varphi\right)\dot{e}\delta_{ij}\right] + P_L\delta_{ij}$$

$$\eta = \varphi(\theta)\eta_0(\phi, T) \quad \text{and} \quad \zeta = 2\psi(\theta)\eta_0(\phi, T)$$

$$\varphi = (1-\theta)^2 \qquad \psi = \frac{2}{3}\frac{(1-\theta)^3}{\theta}$$

$$\nabla_j\sigma_{ij} = (1-\theta)\rho g_i$$

ϕ: Volume fraction of solid phase
ρ^0_S : Density of solid phase
ρ^0_L : Density of liquid phase
J^c_i : Flux of mono-size grains due to nonhomogeneous shear flow
J^η_i : Flux of mono-size grains due to viscosity gradients
J^S_i : Settling flux of solid grains
σ_{ij} : external applied stress
$\sigma(W)$: effective stress model
W: effective strain rate
$\dot{\varepsilon}_{ij}$: total strain rate
φ: normalized shear modulus
ψ: normalized bulk modulus
$\dot{e}$: volume strain rate
δ_{ij} : Kronecker delta
P_L: sintering stress
θ: porosity

$$\sigma_{ij} = 2\eta\left(\dot{\varepsilon}_{ij} - \frac{1}{3}\dot{e}\delta_{ij}\right) + \zeta\dot{e}\delta_{ij} + P_L\delta_{ij}$$

Density: $\rho = \rho^0_S\phi + \rho^0_L(1-\phi)$

Flux : $J_i = J^C_i + J^\eta_i + J^S_i$

Torresani, E., German, R.M., Huff, R. and Olevsky, E.A., Influence of gravity on sintering of 3D-printed powder components. (2022) *Journal of the American Ceramic Society*.

141

141

Gravity Influence on Sintering

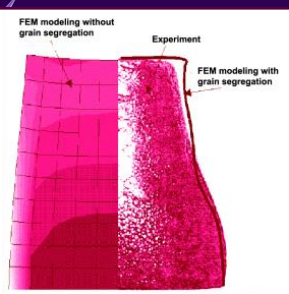

The calculated "elephant foot" profile and relative density distribution formed during liquid-phase sintering of 78W-15.4Ni-6.6Fe powder sample (from E.A. Olevsky and R.M. German, *Acta Mater.*, 48, 1167-1180 (2000))

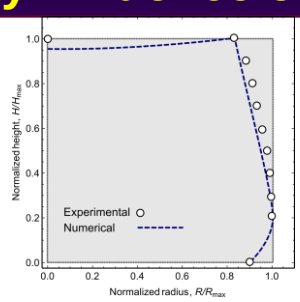

J.A. Alvarado-Contreras, R.M. German, A.L. Maximenko, E.A. Olevsky, Coupled Densification—Shape Distortion Analysis of Liquid Phase Sintering Affected By Gravity, *Met. Mater. Trans. A* 45 (2), 927-933 (2014)

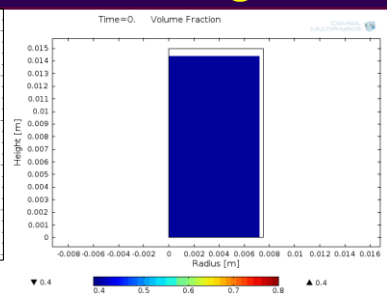

J.A. Alvarado-Contreras, E.A. Olevsky, A.L. Maximenko, R.M. German, A continuum approach for modeling gravitational effects on grain settling and shape distortion during liquid phase sintering of tungsten heavy alloys, *Acta Mater.*, 65, 176-184 (2014)

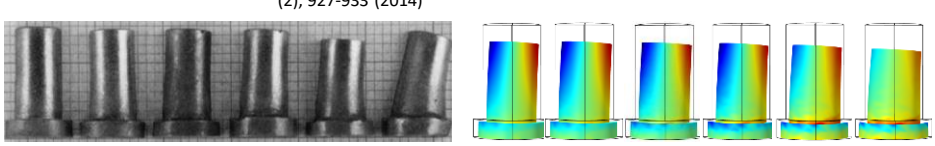

Comparison between the experimental and simulated gravity-induced distortions (with slumping)

J.A. Alvarado-Contreras, E.A. Olevsky, A.L. Maximenko, R.M. German, Kinetics of shrinkage and shape evolution during liquid phase sintering of tungsten heavy alloy, *J. Mater. Sci.*, 49 (3), 1130-1137 (2014)

142

142

Experimental Conditions

Binder Jetting

Powder: Fe-0.5V Sandvik - nominal composition:
Fe - 0.4-0.6% V - 0.1-0.3% C- 0.6% max Mn- 0.5% max Si

- size range: 90% - 22 micron
- 10% binder

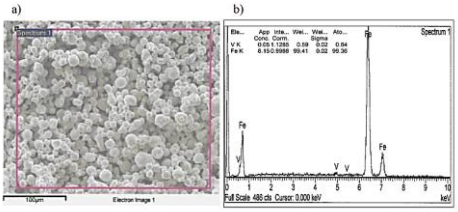

Stereolithography

Slurry: Ceramic powder with photocurable resin

Element	Weight%
O	55.25
Na	4.11
Al	5.8
Si	32.38
K	2.47
Totals	100

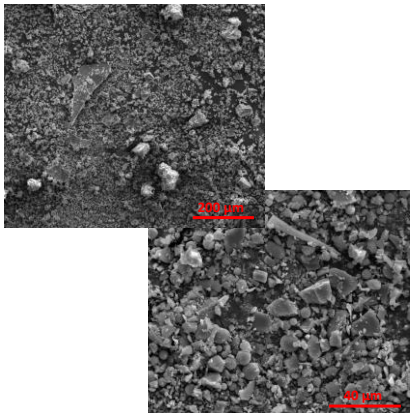

Experimental Conditions

Binder Jetting

Debinding 480°C x 2h + Sintering at 1350°C x 2h

Heating Rate 5°C/min

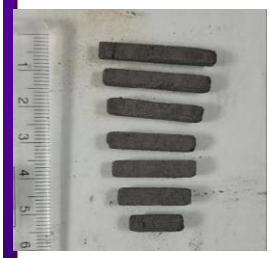

n	Length [mm]	Width [mm]	Thickness [mm]
1	15	5	3
2	20	5	3
3	23	5	3
4	25	5	3
5	27	5	3
6	30	5	3
7	33	5	3

Torresani, E., German, R.M., Huff, R. and Olevsky, E.A., Influence of gravity on sintering of 3D-printed powder components. (2022) *Journal of the American Ceramic Society*.

Stereolithography

Debinding 240°C x 4h and 300°C x1h + Sintering at 1270°C x 2h

Heating Rate 3°C/min

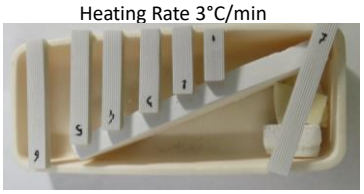

n	Length [mm]	Width [mm]	Thickness [mm]
1	15	6	3
2	20	6	3
3	25	6	3
4	30	6	3
5	35	6	3
6	40	6	3
7	44	6	3

Experimental Conditions

Binder Jetting

Dilatometry Test:
After Debinding 480°C x 2h
- Sintering at 1350°C x 15 min - Heating Rate 5°C/min
- Cylindrical specimens: 5 mm x 10 mm

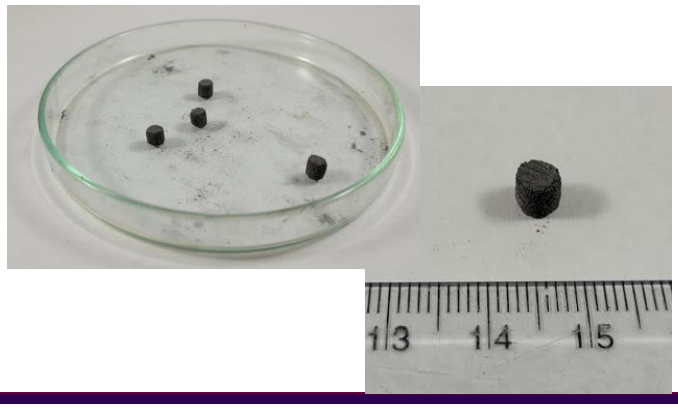

Stereolithography

Dilatometry Test:
After Debinding 300°C x 2h and pre-consolidation at 800°C x 2h:

- Sintering at 1270°C x 15 min - Heating Rate 5°C/min
- Cylindrical specimens: 5 mm x 10 mm

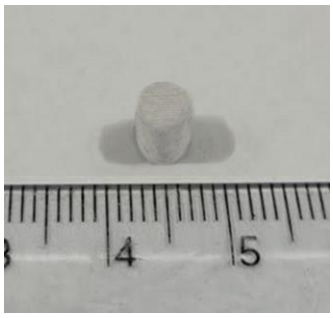

Experimental Conditions

Binder Jetting

Dilatometry Test:
After Debinding 480°C x 2h
- Sintering at 1350°C x 15 min - Heating Rate 5°C/min
- Cylindrical specimens: 5 mm x 10 mm

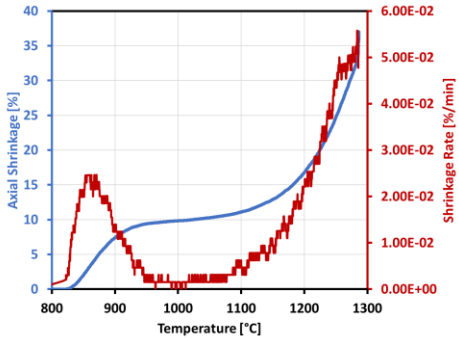

Stereolithography

Dilatometry Test:
After Debinding 300°C x 2h and pre-consolidation at 800°C x 2h:

- Sintering at 1270°C x 15 min - Heating Rate 5°C/min
- Cylindrical specimens: 5 mm x 10 mm

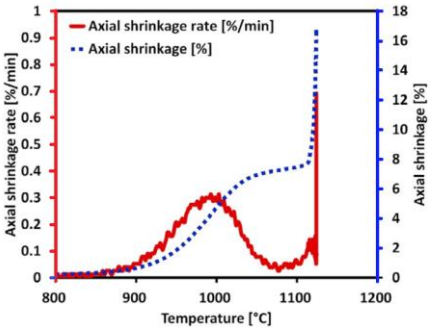

Experimental Conditions

Sintering parameters

$$\eta_0 = A_0 T exp\left(\frac{Q}{RT}\right)$$

$$P_L = \frac{-\eta_0(T)\psi\dot{\theta}}{(1-\theta)} = \frac{3\alpha(1-\theta)^2}{r} \longrightarrow Y = ln\left(-\frac{3(1-\theta)^3}{rT\psi\dot{\theta}}\right) = ln\left(\frac{A_0}{\alpha}\right) + \frac{Q}{RT}$$

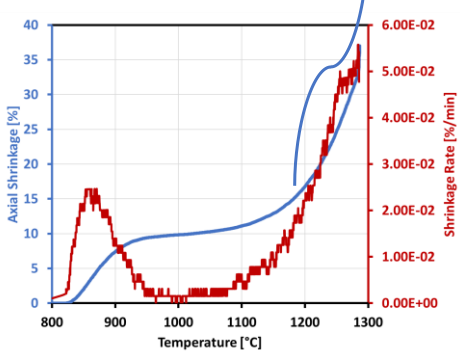

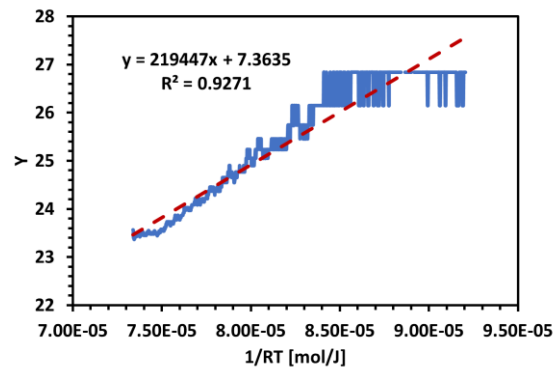

Experimental Conditions

Binder Jetting

Debinding 480°C x 2h

Sintering at 1350°C x 2h, Heating Rate: 5°C/min

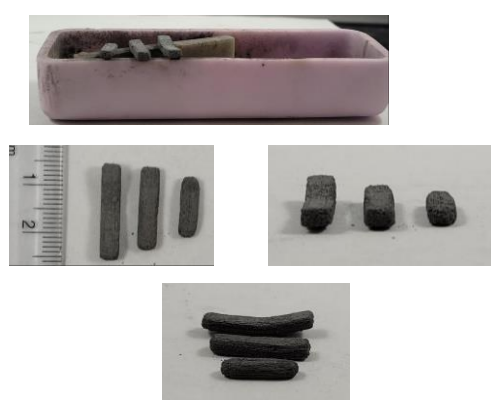

Experimental Conditions

Stereolithography

Debinding 240°C x 4h and 300°C x1h and Sintering at 1270°C

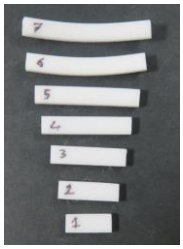

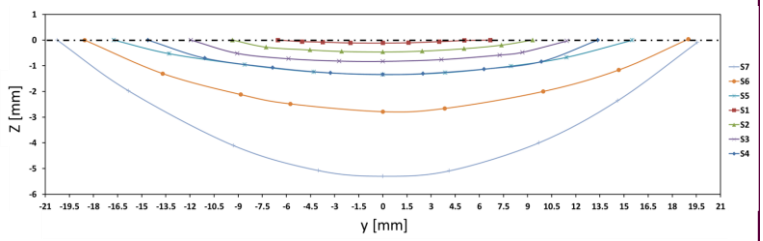

Torresani, E., German, R.M., Huff, R. and Olevsky, E.A., Influence of gravity on sintering of 3D-printed powder components. (2022) *Journal of the American Ceramic Society*.

Modeling Results

Binder Jetting

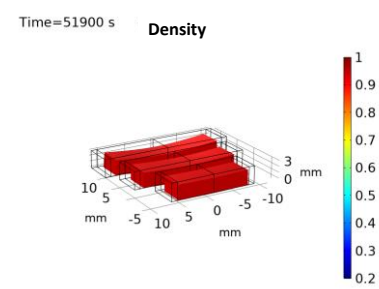

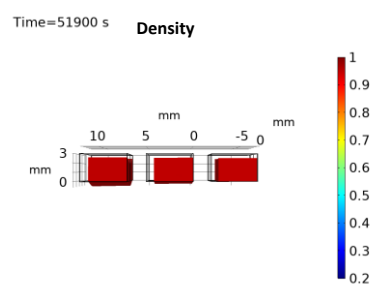

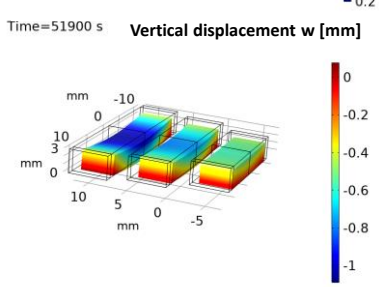

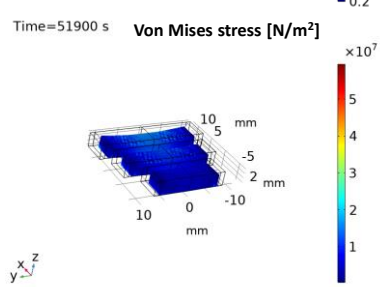

Modeling Results

Stereolithography

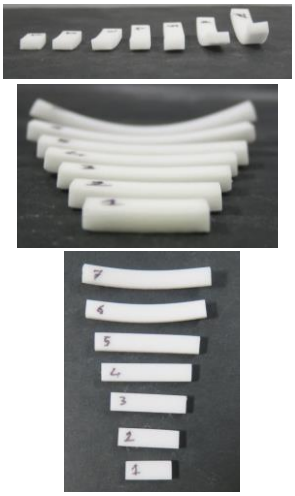

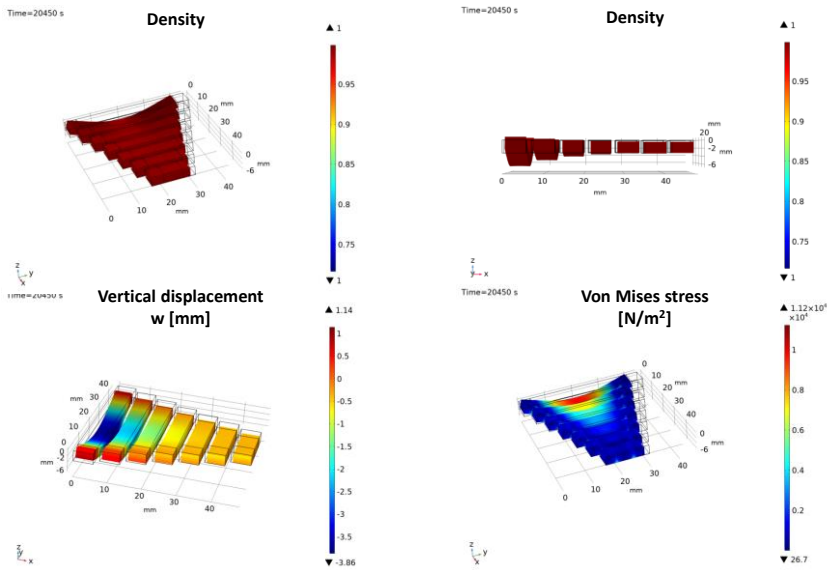

Modeling Results

Stereolithography - Analytical model for design

Normalized deflection

$$\frac{\delta_{max}}{l_0} = A\chi\left(\theta_f\right)\ln\left(\frac{\theta_0}{\theta_f}\right)\left(\frac{l_0}{t_0}\right)^n$$

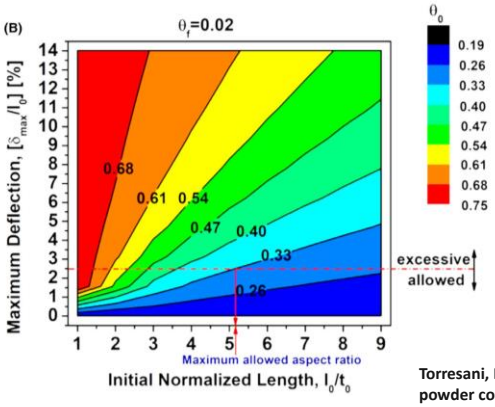

$$\frac{\delta_{max}}{l_0} = \frac{5\rho_{\text{th}}g}{432}\frac{a}{\alpha}t_0\frac{5-8\theta_f}{2\left(1-\theta_f\right)^3}\ln\left(\frac{\theta_0}{\theta_f}\right)\left(\frac{l_0}{t_0}\right)^3$$

$$n \approx 3$$

$$A \approx \frac{5\rho_{th}g}{432}\frac{a}{\alpha}t_0$$

$$\chi\left(\theta_f\right) = \frac{5-8\theta_f}{2\left(1-\theta_f\right)^3}$$

a = grain size
α = surface energy
ϑ_0 = initial porosity
ϑ_f = final porosity
l_0 = initial length
t_0 = initial thickness
ρ_{th} = theoretical density
g = gravity force

Torresani, E., German, R.M., Huff, R. and Olevsky, E.A., Influence of gravity on sintering of 3D-printed powder components. (2022) *Journal of the American Ceramic Society*.

SPS NET SHAPING CAPABILITY

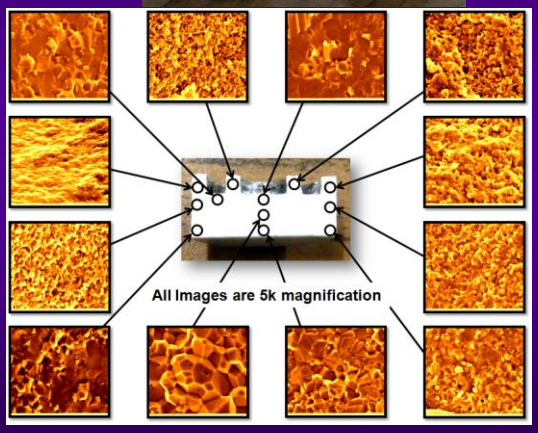

R. Bordia, S.J. Kang, E.A. Olevsky, Current understanding and future research directions at the onset of the next century of sintering science and technology, J. Am. Ceram. Soc., 100, 2314-2335 (2017)

153

153

DENTAL IMPLANT PROTOTYPE PRODUCED BY SPS-FPSPS SEQUENCE

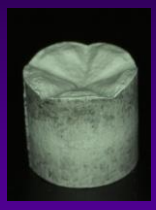

Complex shape HAp-based dental implant prototype produced by SPS-FPSPS sequence

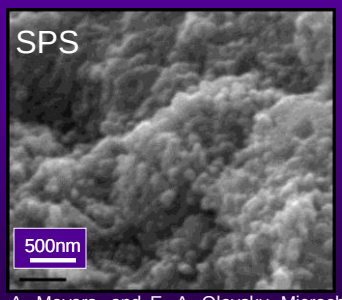

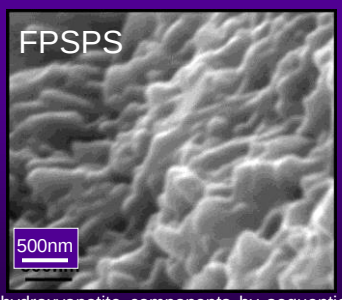

Y.-S. Lin, M. A. Meyers, and E. A. Olevsky, Microchannelled hydroxyapatite components by sequential freeze drying and free pressureless spark plasma sintering, *Adv. App. Ceram.*, 111, 269-274 (2012)

154

154

Cost-Effective Multi-Component Binder-Jetting

Printing of an alumina gear and HAP dental implant at SDSU Powder Technology Laboratory. The total equipment cost is less than $1500.

CONTROLLABLE INTERFACE SOLUTIONS

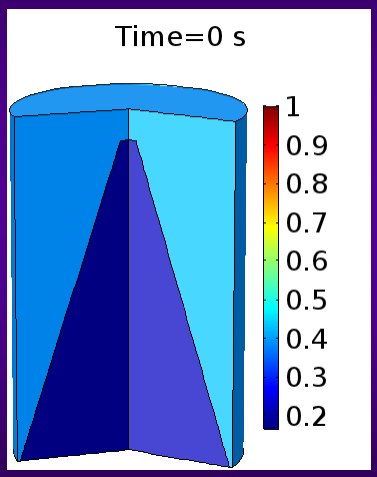

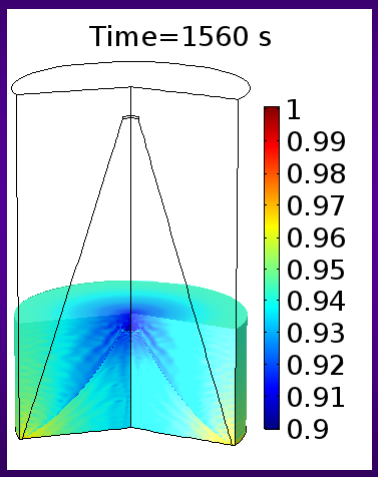

Complex Shapes Spark Plasma Sintering

- Densification of large complex shape by very low electric current

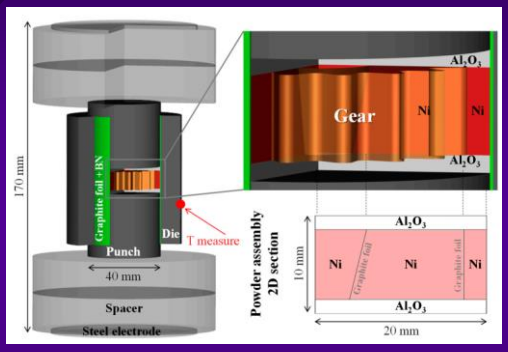

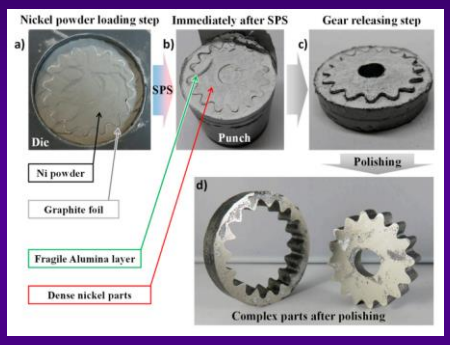

Energy efficient SPS configuration
+
Controllable interface approach

- Graphite paper act as
  a. Movable interface during sintering
  b. Lubricant when releasing sintered parts

C. Manière, E. Torresani, E.A. Olevsky, Simultaneous Spark Plasma Sintering of Multiple Complex Shapes, Materials, 12, 557 (2019)

157

157

Complex Shapes Spark Plasma Sintering

- Large sized Ni gear which has the homogenous structure was obtained

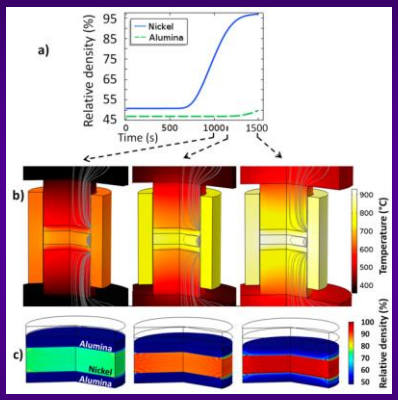

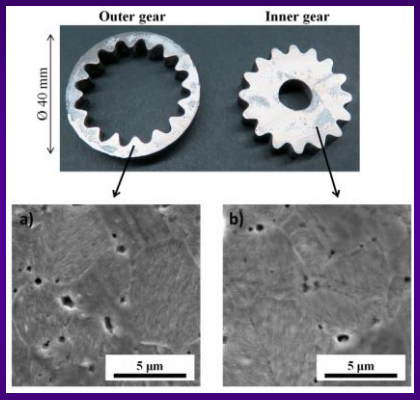

- Low thermal conductivity of alumina
- High thermal conductivity of Ni

⇨ **Homogeneous density and grain size over 40mm samples**

C. Manière, E. Torresani, E.A. Olevsky, Simultaneous Spark Plasma Sintering of Multiple Complex Shapes, Materials, 12, 557 (2019)

158

158

POST BINDER-JETTING SPS NET SHAPING CAPABILITY

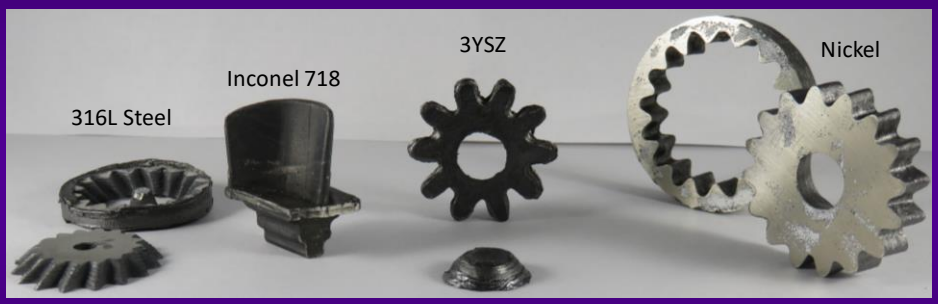

INCONEL TURBINE BLADE PRODUCED BY 3D-PRINTING AND SPS

After 3D-Printing

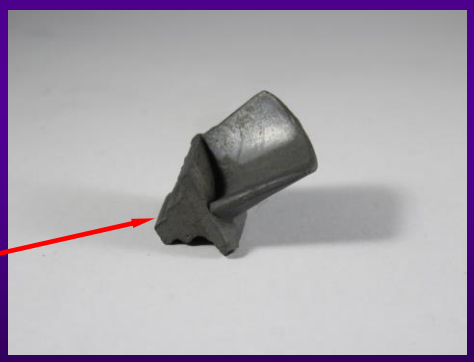

After SPS
(surface still covered by graphite)

Multicomponent Complex Shape Spark Plasma Sintering

~ 50 micro-gears by one SPS run

161

161

Questions / Problems

1. Describe different types of sintering-assisted additive manufacturing techniques.
2. Explain controllable interface approach.
3. Describe how sintering and additive manufacturing complement each other.

162

162

TUTORIAL CONTENTS

New electric nano pulsing (ENP) technology

---Wenwu Xu, Runjian Jiang, Elisa Torresani, Eugene Olevsky et al. Localized engineering of grain boundary morphology by electro-nano-pulsing processing, Mater. Today Adv. 20 (2023) 100442.

Applications of Electric Nano Pulsing (ENP) Technology-Grain Boundary Engineering

Principle of Grain Boundary Engineering by ENP Processing

GBs that are perpendicular to external electric current direction experience large thermal gradient and small current density gradient.

Electric resistance difference at GBs and GIs

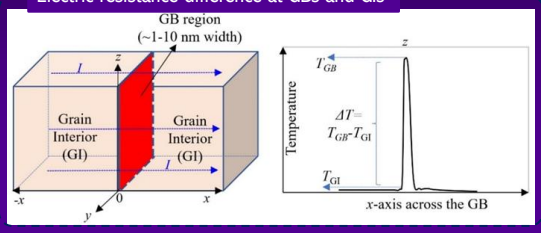

Current density difference at GBs

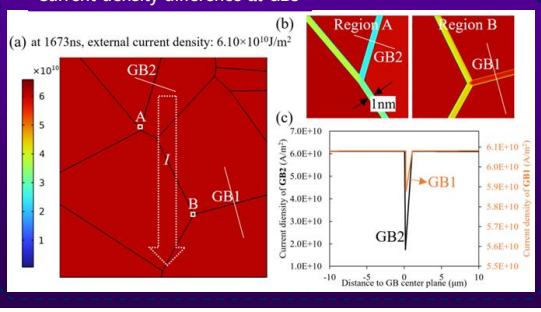

Temperature difference at GBs

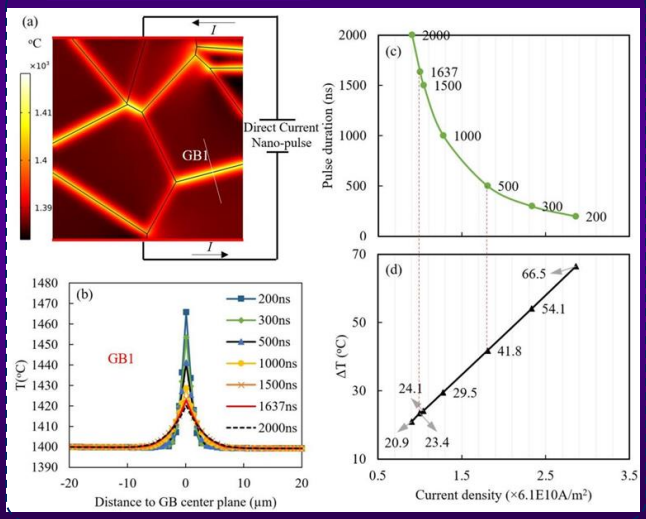

New electric nano pulsing (ENP) technology

Development of Electric Nano Pulsing (ENP) Technology

Q: What does this ENP technology look like?

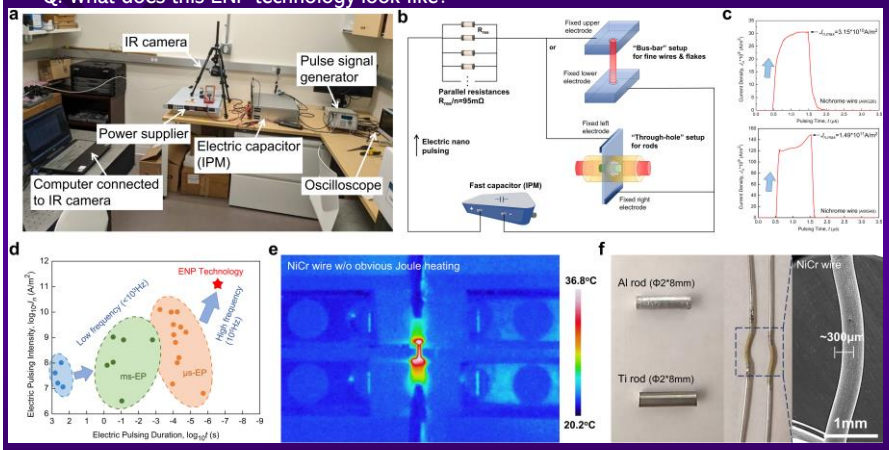

The illustration of proposed electric nano pulsing (ENP) technology. (a) physical picture. (b) schematic diagram showing the electric circuit features and possible sample set up in ENP machine. (c) Examples on the electric pulsing showing the current density curve output by ENP machine. (d) comparison between the proposed ENP technology and other existed electric pulsing technologies showing all-around performance improvement.(e) example on the temperature map of nichrome alloy during ENP process. (f) exemplary images of some conductive materials that are subject to ENP process by different sample setups.

---Eugene A. Olevsky, Runjian Jiang, Elisa Torresani, et. al. Quasi-instantaneous materials processing technology via high-intensity electrical nano pulsing, Sci. Rep. 14 (2024) 434.

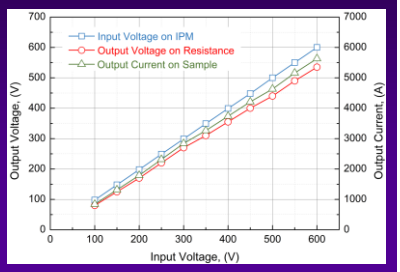

The voltage input and output characteristics of the constructed ENP device.

Unique electric pulsing method:

Ultra-high voltage (1000V)

Ultra-high current density (10^{11}~10^{12}A/m^2)

Ultra-short pulsing duration (<1μs)

Ultra-high pulsing frequency (100 kHz)

Fast Joule heating and strong field effect

Ultra-rapid non-equilibrium microstructure evolution on nanometer spatial scale and nanosecond time scale.

New electric nano pulsing (ENP) technology

Applications of Electric Nano Pulsing (ENP) Technology-Defect Generation and Reconfiguration

Formation mechanism of dislocations by ENP processing

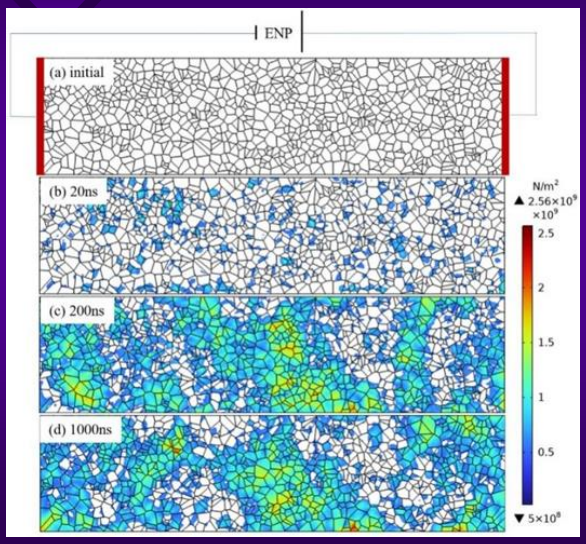

Modelling showing the shear stress distribution in grain interiors and grain boundaries in nichrome alloy during the ENP treatment; (a) initial microcrystalline structure; (b)-(d) distribution of von Mises stress at varied instances.

Reasons for dislocation formation:

- Lattice strain

  1.1% lattice strain at current density of 3×10^9A/m^2.

- Vacancy defects

  Vacancy defects with increased concentration act as the formation sites of massive screw dislocations.

- Shear stress at GBs

  Shear stress is calculated as 4.18×10^{-13}N/atom in the ENP treatment, but it is hundreds times larger due to higher electric resistance at GBs.

New electric nano pulsing (ENP) technology

---Eugene A. Olevsky, Runjian Jiang, Elisa Torresani, et. al. Quasi-instantaneous materials processing technology via high-intensity electrical nano pulsing. Sci. Rep. 14 (2024) 434.

Applications of Electric Nano Pulsing (ENP) Technology-Defect Generation and Reconfiguration

Microstructue and atomic structure of generated dislocations after ENP processing

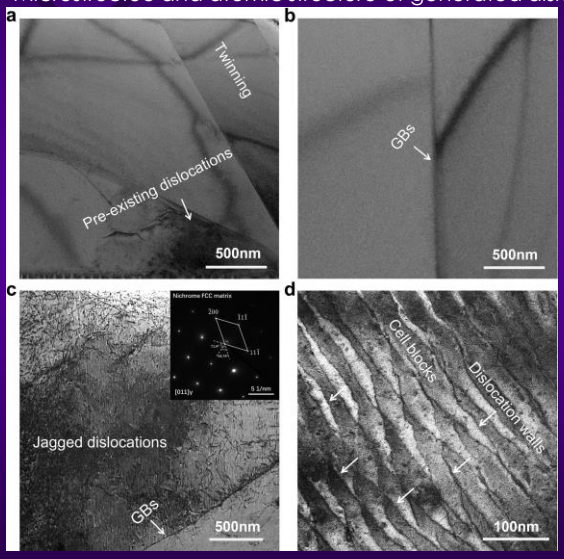

Bright-field TEM images showing the dislocation configurations in nichrome alloys. (a) Raw sample. (b) After conventional heating. (c) After ENP processing of two electric pulses with current density of 6.98×10^{10}A/m^2, pulsing duration of 1μs and pulsing frequency of 100KHz. Insert is the corresponding selected area electron diffraction pattern (SAED) of the FCC matrix along [011] zone axis. (d) After ENP processing of eight electric pulses with current density of 3.15×10^{10}A/m^2, pulsing duration of 1μs and pulsing frequency of 100KHz.

Strong electrical pulses are expected to promote dislocation generation and motion.

- ENP processing (two pulses at a 6.98×10^{10}A/m^2 and 100kHz)
  Jagged dislocations (highly curved morphology)
  Due to cross-slip of extended screw dislocations or point pinning of dislocation lines.

- ENP processing (eight pulses at a 3.15×10^{10}A/m^2 and 100kHz)
  Seaweed dislocations (periodically arranged morphology)
  Due to multiplication and rearrangement of entangled dislocations in various slipping direction.

New electric nano pulsing (ENP) technology

---Eugene A. Olevsky, Runjian Jiang, Elisa Torresani, et. al. Quasi-instantaneous materials processing technology via high-intensity electrical nano pulsing. Sci. Rep. 14 (2024) 434.

Applications of Electric Nano Pulsing (ENP) Technology-Surface Nanocoating

External Morphology of Surface Nanocoating by ENP Processing

By ENP processing (Eight pulses at 3.15×10^{10}A/m^2 and 100kHz

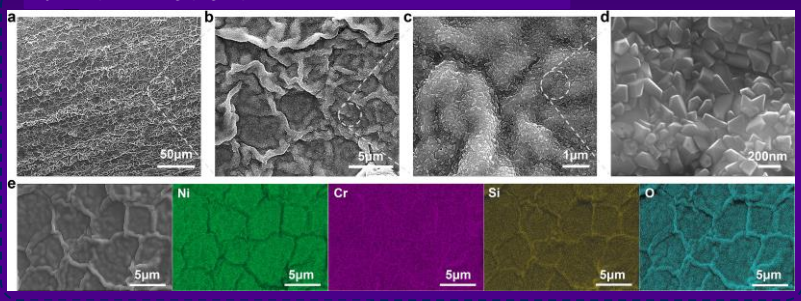

The external morphology of surface nanocoating on nichrome alloy after ENP processing. (a) low-magnification view, (b) fold-like morphology at micro-scale, (c) ravine-like morphology at sub-nanoscale and (d) well-faceted crystals at nano-scale, (e) EDS mapping showing the non-uniform element distribution on surface triple hierarchical nanocoating.

Triple hierarchical structure
- Dense chromium oxide with specific surface area
- Applications in wear-resistant and gas sensors

By thermal processing (1400°C and 10s)

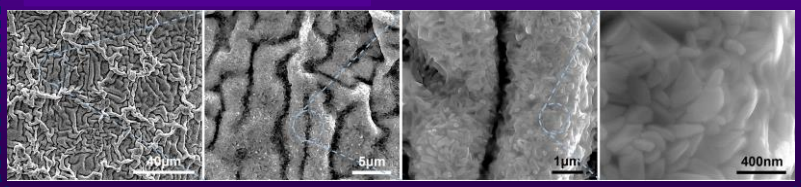

The exterior morphology showing the coarse and loose surface structure on nichrome alloy under conventional furnace at 1400°C (melting point) for 10s. With the magnification increasing from figure a to d, the spheroidization and coarsening of surface layer is clearly observed.

Loose and coarse NiO/Cr_2O_3 or $NiCr_2O_4$ spinel under long-term oxidation

Questions / Problems

1. Describe difference between SPS and ENP.
2. What potential applications does ENP have?

169

169

TUTORIAL CONTENTS

- Sintering Fundamentals: Classic Concepts
- Sintering Fundamentals: Continuum Theory
- Introduction to Field-Assisted Sintering
- Spark-Plasma Sintering
- High-Voltage Electric Discharge Compaction
- Flash Sintering
- Microwave Sintering
- Integrated Additive Manufacturing – Field-Assisted Sintering
- Electric Nano-Pulse Technology

170

170